

Copyright
by
Baiyuan Gao
2018

**The Dissertation Committee for Baiyuan Gao Certifies that this is the approved
version of the following dissertation:**

Stress, Porosity, and Pore Pressure in Fold-and-Thrust Belt Systems

Committee:

Peter B. Flemings, Supervisor

Maria A. Nikolinakou

Demian M. Saffer

Luc L. Lavier

M Bayani Cardenas

Stress, Porosity, and Pore Pressure in Fold-and-Thrust Belt Systems

by

Baiyuan Gao

Dissertation

Presented to the Faculty of the Graduate School of

The University of Texas at Austin

in Partial Fulfillment

of the Requirements

for the Degree of

Doctor of Philosophy

The University of Texas at Austin

December 2018

Acknowledgements

I would first like to acknowledge my supervisor, Dr. Peter Flemings, for his constant support and patient guidance throughout my doctoral studies. I'm incredibly grateful that he always provides me the resources to learn and helps me to grow professionally. I also have truly appreciated that he keeps pushing me beyond where I think I can be to reach my full potential and he helps me evolve to be a better geoscientist. I would also like to thank Dr. Maria Nikolinakou for putting tremendous time and effort into helping me to thrive both technically and personally. When I am struggling, or when I get stuck, she always genuinely encourages me and offers constructive advice to help me overcome the challenges. Many thanks to my committee members Dr. Demian Saffer, Dr. Luc Lavier, and Dr. Bayani Cardenas for sharing their expertise, experience, and knowledge for improving and finishing my dissertation. Thanks to Dr. John Germaine for contributing helpful discussions and thoughtful advice during both of my Master and Ph.D. studies. I would like to express my sincere thanks to all my group members. They have been an indispensable source of professional and personal advice and provided all the help I could have asked for. Finally, I would like to give special thanks to my mother Xiaofeng Bai, my father Chunwen Gao, and my best friend Xiaoyin Li. It is because of their continuous motivation and endless love that I was able to focus on my education and achieve this milestone.

Abstract

Stress, Porosity, and Pore Pressure in Fold-and-Thrust Belt Systems

Baiyuan Gao, Ph.D.

The University of Texas at Austin, 2018

Supervisor: Peter B. Flemings

I use forward geomechanical modeling to study the mechanical and fluid flow behaviors in compressional regions such as fold-and-thrust belts and accretionary wedges. Under drained conditions, lateral tectonic loading increases the mean effective stress and deviatoric stress and drives the sediments to shear-failure as the sediment approaches the deformation front (or trench location). The shear-induced porosity-loss accounts for about one third of the total porosity-loss during tectonic loading under drained conditions. There are four characteristic stress regions in my model: far-field, transition, critical state wedge, and footwall. In the transition zone, the shear-stress ratio varies significantly and the stress state changes from uniaxial-strain compression state to critical state. Increasing the basal friction coefficient leads to a higher surface slope angle and more porosity loss in the footwall whereas increasing the sediment internal strength leads to a lower surface angle and more porosity loss in the hanging wall. Fluid flow has a great impact on stress and compression in fold-and-thrust belts. My models show that the hanging-wall overpressure is greater than the footwall near trench but lower than the footwall overpressure towards the inner wedge. The high hanging-wall overpressure near trench is caused by the rapid increase of total mean and deviatoric stress. A significant finding is that the high

overpressure near trench reduces the vertical effective stress and causes the décollement to be weak near the frontal wedge. Low permeability and high convergence rate promote overpressure generation and enlarge the overpressure-weakened décollement region. This study has broad impacts on the earthquake studies, faults stability analysis, and topics associated fluid flow transport in compressional margins.

Table of Contents

List of Tables	x
List of Figures	xi
Chapter 1: Introduction	1
1.1 Background	1
1.2 This Dissertation	7
1.3 Future research	9
References	10
Chapter 2: Mechanics of Fold-and-Thrust Belts Based on Geomechanical Modeling	13
Abstract	13
2.1 Introduction	14
2.2 Model Description	17
2.2.1 Model Setup	17
2.2.2 Sediment Behavior	18
2.2.3 Modeling Scenarios	21
2.3 Model Results	26
2.3.1 Stress	26
2.3.2 Stress Evolution and Porosity Change	29
2.3.3 Sensitivity Analysis	34
2.3.3.1 Impact of Basal Friction Coefficient	34
2.3.3.2 Impact of Sediment Internal Friction Coefficient	35
2.4 Discussion	40
2.4.1 Stress State	40
2.4.2 Strain	41
2.4.3 Volumetric Change (Compaction)	42
2.4.4 Implications for Field Observations	48
2.4.5 Model Limitations	50
2.5 Summary	51

2.6 Acknowledgments.....	52
2.7 Appendix A: Governing Equations.....	53
2.8 Appendix B: Material Constitutive Model SR3	53
References.....	60
Chapter 3: Overpressure generation and its impact on stress and porosity in accretionary wedge system	68
Abstract.....	68
3.1 Introduction.....	70
3.2 Model description	73
3.2.1 Boundary and initial conditions	76
3.2.2 Material properties	76
3.3 Model results.....	79
3.3.1 Overpressure distribution.....	81
3.3.2 Stresses and compression distribution	83
3.3.3 The evolutionary behavior of stress and compression.....	85
3.3.4 Impact of mudrock permeability.....	90
3.3.5 Impact of convergence rate	96
3.4 Discussion.....	97
3.4.1 Overpressure generation mechanism and implications.....	97
3.4.2 Comparison with critical taper theory.....	103
3.4.3 Strain evolution.....	106
3.4.4 Model limitations and future directions	108
3.5 Conclusions.....	108
References.....	120
Chapter 4: The role of overpressure on décollement friction resistance in frontal subduction zone	125
Abstract.....	125
4.1 Introduction.....	126
4.2 Approach and results.....	127
4.2.1 Model set-up and material properties	127

4.2.2 Base model results	128
4.3 The impact of permeability and convergence rate on stress	133
4.4 Discussion	134
4.5 Conclusions	136
Reference	137
Bibliography	139

List of Tables

Table 2.1: Impact of basal friction on surface angle, stress ratios, and principal stress orientations.....	24
Table 2.2: Impact of internal friction on surface angle, stress ratios, and principal stress orientations.....	25
Table 2.3: SR3 material model parameters.....	55
Table 2.4: Nomenclature.....	56
Table 3.1 List of models and summary of key results.	80
Table 3.2: Nomenclature.....	110
Table 3.3: SR3 material model parameters.....	111

List of Figures

Figure 1.1: Overpressure distribution from one of the transient geomechanical models in my work	7
Figure 2.1: Model set-up and boundary conditions.	22
Figure 2.2: Basic principles of critical state model SR3.....	23
Figure 2.3: (a) Maximum-to-minimum principal effective stress ratio distribution. (b) Shear stress along décollement and threshold value for sliding along décollement.	27
Figure 2.4: (a) Horizontal-to-vertical effective stress ratio at end of simulation. (b) Horizontal, vertical, and mean effective stresses along profile A. (c) Horizontal, vertical, and mean effective stresses along profile B.....	30
Figure 2.5: Comparisons of stress-state and principal-effective-stress orientations at décollement with three different basal friction coefficients	31
Figure 2.6: (a) Mean effective stress at end of system evolution. (b) Shear-stress ratio. (c) Porosity. (d) Mean vs. deviatoric stress plot along profile A. (e) Porosity along profiles A and B (depth referring to thousand-meter below seafloor).....	32
Figure 2.7: Stress and compaction history for sediment that moves from initial point A to final point A'	33
Figure 2.8: (a)–(c) Shear-stress ratio distribution for models with different basal friction coefficients. (d) Mean effective vs. deviatoric stress for sediment along profiles A, B, and C. (e) Porosity vs. depth trends along profiles of A, B, C, and D.....	37

Figure 2.9: (a) Geomechanical model prediction (triangles) and critical taper theory prediction (gray line) of wedge surface-slope angle as a function of basal friction coefficient. (b) Maximum principal stress dip angle predicted by geomechanical model in wedge (red diamonds) and in footwall (blue circles), as well as critical taper theory prediction (gray line). (c) Geomechanical model prediction (triangles) and critical taper theory prediction (gray line) of wedge surface-slope angle as a function of internal friction coefficient. (d) Maximum principal effective stress dip angle predicted by geomechanical model in wedge (red diamonds) and in footwall (blue circles), as well as critical taper theory prediction (gray line).38

Figure 2.10: (a)–(c) Contours of shear-stress ratio for internal friction coefficients equal 0.36, 0.44, and 0.53, respectively. (d) Shear-stress ratios along profiles A, B, and C. (e) Porosity vs. depth trends along profiles of A, B, C, and D.39

Figure 2.11: (a) Contours of shear-stress ratio and regions of distinct compaction behavior in a fold-and-thrust belt: (I) critical state wedge region, (II) transition region, (III) far-field geostatic region, and (IV) footwall region. (b) Estimated porosity vs. depths trends corresponding to different shear-stress ratios and associated regions.45

Figure 2.12: Evolution of strain and porosity for a sediment element that passes into the accretionary wedge.46

Figure 2.13: Seismic signature calculated from geomechanical modeling results..47

Figure 2.14: Input hardening: relationship among volumetric strain, compressive intercept (solid line), and tensile intercept (dashed line).58

Figure 2.15: Initial porosity–depth relationship of modeled sediment.	59
Figure 3.1: Model set-up and boundary conditions.	74
Figure 3.2: Basic principles of critical state model SR3.....	75
Figure 3.3: (a) Color contours of overpressure at 85 km of tectonic displacement. (b) Color contours of overpressure ratio. (c) Overpressure along profile A in (a) together with reduced overburden stress. (d) Overpressure ratio along profile A. (e) Horizontal, vertical , and mean effective stresses along profile A.	82
Figure 3.4: (a) Color contour of mean effective stress. (b) Deviatoric stress. (c) Shear- stress ratio. (d) Porosity. (e) Mean effective stress and deviatoric stress for hanging-wall (red circles) and footwall (green triangles) along profile A. (f) Porosity along profile A and porosity results from drained model.	88
Figure 3.5: Stress and compression paths of hanging-wall (A) and footwall (B) sediment.	89
Figure 3.6: Impact of permeability on overpressure.	92
Figure 3.7: Impact of permeability on stress and compression	93
Figure 3.8: Impact of convergence rate on overpressure	94
Figure 3.9: Impact of convergence rate on stresses and compaction.....	95
Figure 3.10: (a) Schematic figure of the trajectory of a tracked sediment as it is incorporated into the prism. (b) Stress history. (c) Pore pressure generation components versus loading time. (d) The compression path along t1 to t3 in (b).....	98
Figure 3.11: (a) Color contour of pore pressure ratio. (b) Pore pressure ratio along the vertical profiles in (a).....	105

Figure 3.12: Evolution of strain of a sediment element that passes into the accretionary wedge from the transient model (base case).	107
Figure 3.13: (a) The porosity and vertical effective stress relationship at uniaxial strain condition. (b) The porosity and permeability relationships for high-permeability, medium permeability, and low-permeability. (c) The permeability and vertical effective stress relationship. (d) The coefficient of consolidation and vertical effective stress relationship.	112
Figure 3.14: Input hardening: relationship among volumetric strain, compressive intercept, and tensile intercept	113
Figure 3.15: (a) Stress path from a0 to a1. (b)The corresponding compression path due to drainage from a0 to a1.	119
Figure 4.1: (a) Model set-up and boundary conditions.....	129
Figure 4.2: (a) The evolution of stress and pressure in a sediment element immediately above the décollement. (b) The variation of stress and pressure immediately above the décollement at the end of the simulation. (c) The distribution of vertical effective stress and the frictional resistance immediately above the décollement at the end of the simulation.....	131
Figure 4.3: (a) Impact of mudrock permeability on the vertical effective stress and basal frictional resistance along décollement. (b) Impact of convergence rate on the vertical effective stress and basal frictional resistance. The “slow”, “med.”, and “fast” represent displacement rate of 1mm./yr., 5mm./yr., and 10mm./yr., respectively.	135

Chapter 1: Introduction

1.1 BACKGROUND

Fold-and-thrust belts develop in the foreland of major orogenic belts (Jordan & Grotzinger, 2008). A fold-and-thrust belt is composed of a series of folds and thrust-faults that are produced by compressional tectonics (Allaby, 2013). An accretionary wedge (or prism) forms at the leading edge of the convergent boundary where the top sediment on the subduction plate is scrapped off and appended to the overriding plate (Steele *et al.*, 2009). The gliding interface between the overriding plate and the subducting plate is called the décollement and it separates the intensely deformed overlying rock and the much less deformed underlying rock. Because fold-and-thrust belts and accretionary wedges have similar structures (folds and faults) and are both formed in compressional tectonic environments, mechanisms associated with fold-and-thrust belts can also be applied to accretionary wedges.

The development of a thin-skinned fold-and-thrust belt at convergent plate boundaries is analogous to snow piling up in front of a bulldozer (Davis *et al.*, 1983; Dahlen, 1990). Sediment deforms significantly above the décollement and gradually forms a wedge-shaped geometry due to a large amount of shortening and thickening (Chapple, 1978). In contrast, the sediment below the décollement experiences much less deformation. Critical taper theory assumes the entire wedge is at shear failure condition. The wedge geometry is controlled by the combined effects of sediment internal friction

coefficient, basal friction coefficient, and pore fluid pressure distribution (Dahlen, 1990; Dahlen & Suppe, 1988; Davis et al., 1983).

Lateral tectonic loading alters mean effective stress and deviatoric stress and both of them contribute to sediment compression. Conventionally, sediment is assumed to deform only in the vertical direction during burial without lateral strain (uniaxial-strain compression) (e.g. (Hart *et al.*, 1995; Stigall & Dugan, 2010)). Under this assumption, the horizontal effective stress (σ'_h) is assumed to be proportional to the vertical effective stress (σ'_v) with a constant horizontal-to-vertical effective stress ratio of K_0 ($\sigma'_h = K_0\sigma'_v$). The maximum and minimum principal stress remain vertical and horizontal, respectively. Thus, under uniaxial-strain compression, the change of mean effective stress, deviatoric stress, and porosity depend only on the change of vertical effective stress. However, the uniaxial-strain compression assumption does not apply in non-uniaxial deformation regions, such as fold-and-thrust belts and salt systems (Hauser *et al.*, 2014; Nikolinakou *et al.*, 2018). In a fold-and-thrust belt, tectonic loading increases the lateral stress independent from the vertical load. As a result, the horizontal effective stress no longer depends only on the vertical effective stress. Sediment that is initially outside the prism has an initial horizontal stress that is a fraction of the vertical effective stress. However, as this sediment passes into an accretionary prism, the horizontal effective stress increases, becoming equal to, and eventually greater, than the vertical effective stress. The increase in horizontal stress ultimately leads to an increase in deviatoric (differential) stress and results in shear failure when the deviatoric stress reaches the maximum deviatoric stress that the sediment can

withstand. The additional increase in mean effective stress and deviatoric stress caused by non-uniaxial strain compression results in additional porosity loss compared to uniaxial strain compression at equivalent depths (Chapter 2). Poroelastic models (e.g., Wang (2017)) can account for volumetric changes caused by the mean effective stress, however they do not incorporate porosity loss because of shear-induced compression.

Critical state soil mechanics (Roscoe & Burland, 1968; Wood, 1990) provides a quantitative approach to account for the interrelationship of mean stress, shear stress and porosity under complex stress paths. Thus, this method is more appropriate than the uniaxial or poroelastic approach to study the compression in fold-and-thrust-belts. Karig (1986) first recognized that tectonic loading in fold-and-thrust belts leads to non-uniaxial stress paths and he introduced the concept of critical state soil mechanics in fold-and-thrust belt studies. More recently, Kitajima et al., (2017) and Flemings & Saffer (2018) applied critical state soil mechanics on experimental and field data to estimate material properties, stresses and pore pressures in fold-and-thrust belt systems.

The pore pressure distribution in a fold-and-thrust belt is a result of the tectonic loading and fluid drainage processes. Tectonic loading provides the source of overpressure generation by increasing the total mean stress and deviatoric stress. The fluid drainage process depends on the drainage length, permeability, and compressibility. Long drainage path, low permeability, and high compressibility will limit the fluid drainage thus preserve high overpressure. When the fluid cannot be expelled from the pores efficiently during tectonic loading, part of the tectonic load is supported by the pore fluid, causing

overpressure; the rest of the load is supported by the sediment matrix, increasing effective stresses and decreasing porosity.

The mechanical and hydrological properties of the sediment in fold-and-thrust belts significantly impact the fault strength, slip behavior, and are closely related to earthquake ruptures and tsunamis (Scholz, 2002; Saffer & Tobin, 2011). Thus, it is crucial to understand how stress and fluid flow evolve in fold-and-thrust belts. Several approaches have been developed to investigate the deformation, stresses and pore pressure in fold-and-thrust belts. A few commonly used approaches are listed below with their capabilities and limitations:

- Critical taper theory provides an analytical model based on force balance to understand the interrelationship between wedge geometry, basal friction, material strength, and pore pressure. (Davis *et al.*, 1983). However, critical taper theory cannot address the sediment compression behavior nor the pore pressure variation, because it assumes constant sediment density and a constant pore pressure ratio (pore pressure is proportional to overburden stress) throughout the wedge. In addition, critical taper theory does not address the footwall mechanics.
- The steady state flow model (e.g (Saffer & Bekins, 2002)) is able to predict the pore pressure variation given a prescribed porosity distribution and a relationship between porosity and permeability. However, the sediment porosity in this model is not coupled to stress. As a result, the steady state flow model cannot predict the change of porosity and permeability caused by tectonic loading.

- Kinematics models (e.g. (Morgan & Karig, 1995)) can estimate the magnitude and orientation of principal strains in different locations of a fold-and-thrust belt. Morgan (1994) uses the seismic profile and available porosity distribution to constrain the strain field in a deformed regime. However this type of model does not predict stresses or pore pressures.

None of these traditional models can reveal the coupled behavior of stress, strain, porosity, and pore pressure in fold-and-thrust belts.

Transient evolutionary geomechanical models provide a way to explore how stresses, porosity, and pore pressure change as the sediment deforms. Transient evolutionary models have been applied in anticlines, faults, and salt systems (Crook *et al.*, 2006; Heidari *et al.*, 2016; Nikolinakou *et al.*, 2018). Recently, they have been applied to study fold-and-thrust belts. For example, Rowe *et al.* (2012) use a transient evolutionary model to simulate the stress and deformation of the frontal thrust in Nankai accretionary wedge. Obradors-Prats *et al.* (2017) simulate the Borne fold-and-thrust belt. These published models limit the displacement in the hanging-wall to only a few kilometers. In addition, they prescribe the initial wedge geometry; as a result, they cannot capture how stress and porosity change with time from the onset of tectonic loading to shear failure. Finally, none of the existing models incorporates the role of shear stress on porosity loss and pore pressure generation.

The purpose of my dissertation is to study the poro-mechanical behavior of sediments in fold-and-thrust belts using large-strain forward geomechanical models

(Figure 1.1). I describe the sediments using the SR3 material model (Rockfield, 2017). SR3 is a poro-elastoplastic formulation from the critical state soil mechanics family of models (Wood, 1990). This material model is able to take into account the effect of shear on compression, hence, to couple sediment porosity loss with the full stress tensor. I capture the evolution and distribution of stress, strain, porosity, and pore pressure in fold-and-thrust belts systems. I also study the impact of sediment internal friction, basal friction, rock permeability, and convergence rate on stress and compression.

The major findings of my study are as follows:

- Hanging-wall sediment has a much higher mean effective stress and deviatoric stress than the footwall and this stress contrast results in a sudden porosity change at the décollement.
- Shear induced porosity loss accounts for about 35% of total porosity loss during tectonic loading in drained conditions. The fraction of shear-induced compression is even higher for the compression under transient conditions.
- Near the trench, hanging-wall overpressure is greater than footwall overpressure because of high mean and shear stresses.
- High overpressure generated by tectonic loading significantly reduces the basal friction resistance and leads to weak décollement conditions.
- Low permeability and fast convergence rate further reduce the basal friction resistance and broaden the region of weak décollement
- The coupled model suggests the persistence of a low friction zone along the

décollement near the wedge tip.

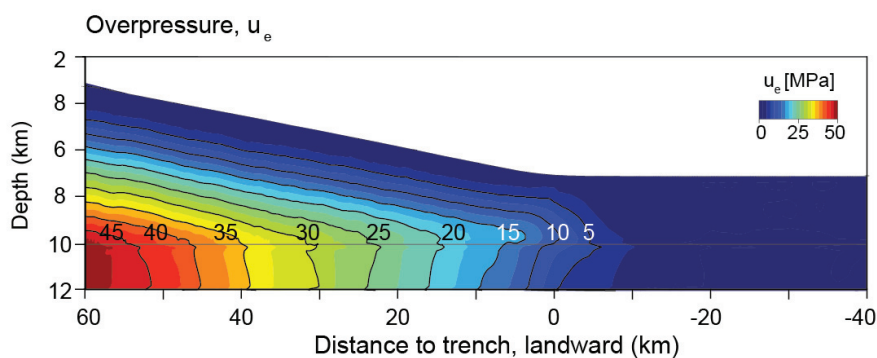


Figure 1.1: Overpressure distribution from one of the transient geomechanical models in my work

1.2 THIS DISSERTATION

In Chapter 2, I built a drained geomechanical model to examine the mechanical behavior and the evolution of sediment porosity and strength in fold-and-thrust belts. I explain that the observation of porosity offset at the décollement is due to the fact that both mean effective stress and deviatoric stress in the hanging-wall are much greater than in the footwall. I quantify that shear stress accounts for about 35% of the total porosity loss during tectonic loading. I find a transition zone in which the stress ratios and compression curves vary rapidly from uniaxial to their critical state values. I investigate the impact of basal friction and sediment internal strength on both hanging-wall and footwall. High basal frictional resistance results in higher porosity loss in the footwall but it does not impact the hanging-wall porosity. High sediment internal strength results in higher porosity loss in the

hanging-wall but it has little impact on the footwall porosity. Finally, I demonstrate how the strain ellipse evolves as a sediment is consumed into the critical wedge.

In Chapter 3, I built coupled geomechanical models to investigate the interaction of mechanical and fluid-flow behavior in a fold-and-thrust belt. Because I model sediments with a critical state formulation, porosity, stress, and pore pressure are interrelated to each other. The fluid flow is simulated by Darcy's law and the permeability is updated as a function of porosity. I find the hanging-wall overpressure is greater than the footwall overpressure near trench whereas lower than the footwall overpressure toward the inner wedge. The great hanging-wall overpressure near trench is caused by the rapid increase of total mean stress and deviatoric stress. This high overpressure, both within the hanging and in the footwall sediments results in less porosity loss compared to fully drained conditions. Subsequently, the porosity offset at the décollement is less pronounced.

In Chapter 4, I focus on studying the hydro-mechanical conditions along the décollement and its implications on slip behavior and earthquake events. I find that lateral tectonic loading causes rapid change of stresses and overpressure near the trench. Both total mean stress and deviatoric stress contribute to overpressure generation. The rapid increase of overpressure reduces the normal effective stress at the frontal wedge and thus decreases the frictional resistance at the décollement. A higher convergence rate or lower permeability further reduce the décollement frictional resistance and cause a broader zone of weak décollement. These results suggest that the highly overpressured wedges are more prone to develop aseismic slip.

1.3 FUTURE RESEARCH

This study provides the ground work for further research. Here, I propose three potential future advancements.

My first suggestion is to simulate faults in fold-and-thrust belt models. Faults are commonly found in these systems and significantly impact the stress states and fluid flow field. The current model suggests that the wedge has reached shear failure but does not simulate the formation of individual faults.

My second suggestion is to assign high permeability in the décollement zone. In the field, the fractured décollement zone may have a much higher permeability than the sediment above and below it. The current models only consider the permeability change due to sediment compression (porosity loss).

Another suggestion is to include interbedded sand layers into the models. Sandstone strata is commonly found in fold-and-thrust belt and it has very different rock strength and permeability properties compared to mudrocks. Incorporating sand layers into the geomechanical modeling will help us understand how stronger and more permeable layers can influence the stresses, fluid flow, and structure styles in fold-and-thrust belts.

REFERENCES

- Allaby, M. (Ed.), 2013, A dictionary of geology and earth sciences. Oxford University Press., p. 226
- Chapple, W.M., 1978, Mechanics of thin-skinned fold-and-thrust belts: Geological Society of America Bulletin, v. 89, no. 8, p. 1189, doi: 10.1130/0016-7606(1978)89<1189:MOTFB>2.0.CO;2.
- Crook, A.J.L., Owen, D.R.J., Willson, S.M., and Yu, J.G., 2006, Benchmarks for the evolution of shear localisation with large relative sliding in frictional materials: Computer methods in applied mechanics and engineering, v. 195, 37-40, p. 4991–5010, doi: 10.1016/j.cma.2005.11.016.
- Dahlen, F.A., 1990, Critical Taper Model Of Fold-And-Thrust Belts And Accretionary Wedges: Annual Review of Earth and Planetary Sciences, v. 18, no. 1, p. 55–99, doi: 10.1146/annurev.earth.18.1.55.
- Davis, D., Suppe, J., and Dahlen, F.A., 1983, Mechanics of fold-and-thrust belts and accretionary wedges: Journal of Geophysical Research, v. 88, B2, p. 1153, doi: 10.1029/JB088iB02p01153.
- Flemings, P.B., and Saffer, D.M., 2018, Pressure and Stress Prediction in the Nankai Accretionary Prism: A Critical State Soil Mechanics Porosity-Based Approach: Journal of Geophysical Research: Solid Earth, v. 123, no. 2, p. 1089–1115, doi: 10.1002/2017JB015025.
- Gao, B., Flemings, P.B., Nikolinakou, M.A., Saffer, D.M., and Heidari, M., 2018, Mechanics of Fold - and - Thrust Belts Based on Geomechanical Modeling: Journal of Geophysical Research: Solid Earth.
- Goult, N.R., 2004, Mechanical compaction behaviour of natural clays and implications for pore pressure estimation: Petroleum Geoscience, v. 10, no. 1, p. 73–79, doi: 10.1144/1354-079302-552.
- Hart, B.S., Flemings, P.B., and Deshpande, A., 1995, Porosity and pressure: Role of compaction disequilibrium in the development of geopressures in a Gulf Coast Pleistocene basin: Geology, v. 23, no. 1, p. 45, doi: 10.1130/0091-7613(1995)023<0045:PAPROC>2.3.CO;2.

- Hauser, M.R., Couzens-Schultz, B.A., and Chan, A.W., 2014, Estimating the influence of stress state on compaction behavior: *Geophysics*, v. 79, no. 6, D389-D398, doi: 10.1190/geo2014-0089.1.
- Heidari, M., Nikolinakou, M.A., Hudec, M.R., and Flemings, P.B., 2016, Geomechanical analysis of a welding salt layer and its effects on adjacent sediments: *Tectonophysics*, v. 683, p. 172–181, doi: 10.1016/j.tecto.2016.06.027.
- Jordan, T.H., and Grotzinger, J., 2008, *The Essential Earth*, W. H. Freeman., p. 217.
- Karig, D.E., 1986, Physical properties and mechanical state of accreted sediments in the Nankai Trough, Southwest Japan Arc, in Moore, J.C., ed., *Structural Fabrics in Deep Sea Drilling Project Cores From Forearcs*, Geological Society of America, p. 117–133.
- Kitajima, H., Saffer, D., Sone, H., Tobin, H., and Hirose, T., 2017, In Situ Stress and Pore Pressure in the Deep Interior of the Nankai Accretionary Prism, Integrated Ocean Drilling Program Site C0002: *Geophysical Research Letters*, v. 44, no. 19, p. 9644–9652, doi: 10.1002/2017GL075127.
- Morgan, J.K., and Karig, D.E., 1995, Kinematics and a balanced and restored cross-section across the toe of the eastern Nankai accretionary prism: *Journal of Structural Geology*, v. 17, p. 31–45.
- Morgan, J.K., Karig, D.E., and Maniatty, A., 1994, The estimation of diffuse strains in the toe of the western Nankai accretionary prism: A kinematic solution: *Journal of Geophysical Research: Solid Earth* (1978–2012), v. 99, p. 7019–7032.
- Nikolinakou, M.A., Heidari, M., Flemings, P.B., and Hudec, M.R., 2018, Geomechanical modeling of pore pressure in evolving salt systems: *Marine and Petroleum Geology*, v. 93, p. 272–286, doi: 10.1016/j.marpetgeo.2018.03.013.
- Obradors-Prats, J., Rouainia, M., Aplin, A.C., and Crook, A.J.L., 2017, Hydromechanical Modeling of Stress, Pore Pressure, and Porosity Evolution in Fold-and-Thrust Belt Systems: *Journal of Geophysical Research: Solid Earth*, v. 122, no. 11, p. 9383–9403, doi: 10.1002/2017JB014074.
- Rockfield, 2017, *Elfen Explicit Manual, Version 4.10*: Swansea, UK, Rockfield Software.
- Roscoe, K. H., & Burland, J. B., 2012, On the generalized stress-strain behaviour of “wet” clay. In J. Heyman (Ed.), *Engineering Plasticity*, Cambridge, England: Cambridge Univ. Press., p.535–609.

- Rowe, K.T., Screaton, E.J., and Ge, S., 2012, Coupled fluid flow and deformation modeling of the frontal thrust region of the Kumano Basin transect, Japan: Implications for fluid pressures and décollement downstepping: *Geochemistry, Geophysics, Geosystems*, v. 13, no. 3, n/a-n/a, doi: 10.1029/2011GC003861.
- Saffer, D.M., and Bekins, B.A., 2002, Hydrologic controls on the morphology and mechanics of accretionary wedges: *Geology*, v. 30, no. 3, p. 271, doi: 10.1130/0091-7613(2002)030<0271:HCOTMA>2.0.CO;2.
- Saffer, D.M., and Tobin, H.J., 2011, Hydrogeology and Mechanics of Subduction Zone Forearcs: Fluid Flow and Pore Pressure: *Annual Review of Earth and Planetary Sciences*, v. 39, no. 1, p. 157–186, doi: 10.1146/annurev-earth-040610-133408.
- Scholz, C.H., 2002, *The Mechanics of Earthquakes and Faulting*. p. 1-50.
- Steele, J.H., Thorpe, S.A., and Turekian, K.K., 2009, *Encyclopedia of Ocean Sciences*, Elsevier, *Encyclopedia of Ocean Sciences*.
- Stigall, J., and Dugan, B., 2010, Overpressure and earthquake initiated slope failure in the Ursa region, northern Gulf of Mexico: *Journal of Geophysical Research: Solid Earth* (1978–2012), v. 115, B4.
- Wood, D.M., 1990, *Soil behaviour and critical state soil mechanics*, Cambridge University Press., p. 139-173.

Chapter 2: Mechanics of Fold-and-Thrust Belts Based on Geomechanical Modeling

ABSTRACT

We use a large strain geomechanical model and critical state soil mechanics to study the evolution of stress and deformation in an evolving fold-and-thrust belt and its underlying footwall sediments. Both mean effective stress and deviatoric stress contribute to porosity loss within the wedge with 35% of the porosity loss resulting from increased shear. As a result, porosity increases abruptly across the décollement because both mean-effective and shear stresses are much higher inside the wedge than in the footwall. As the basal friction coefficient (μ_b) increases, more shear stress is transmitted across the décollement, resulting in additional compaction of the footwall sediment and decrease in the porosity contrast across the décollement. As the internal friction coefficient (μ_s) increases, the wedge sediment is more compacted because it can withstand higher mean-effective and deviatoric stresses. Inside the wedge, the sediment experiences sub-horizontal shortening strain and sub-vertical elongation strain. We predict a 10-30-km-wide “transition zone” in which the shear-stress ratios and compaction curves change rapidly between compressional critical state failure and uniaxial strain (K_0) state. Our model results agree with the taper angles and the stress orientations predicted by critical taper theory. This large-strain drained modeling approach provides first order insights into the mechanical processes of loading and compaction in fold-and-thrust belts and a foundation for understanding field observations of pressure, stress, and deformation in thrust belt systems.

2.1 INTRODUCTION

Fold-and-thrust belts are long-term products of convergent plate boundaries, and are associated with many of the world's largest earthquakes (e.g., 1960 Chile (Cisternas et al., 2005), 1964 Alaska (Plafker, 1965), 2004 Sumatra (Ammon et al., 2005), and 2011 Japan (Simons et al., 2011)). A better understanding of in situ stress, compaction, and pore pressure in fold-and-thrust belts improves our ability to estimate the mechanical strength and slip behavior of major faults (Byrne and Fisher, 1990; Dahlen, 1990; Dahlen and Suppe, 1988; Davis et al., 1983; Hafner, 1951; Hubbert and Rubey, 1959; Zoback, 2010). In addition, fold-and-thrust belts house significant hydrocarbon reserves (e.g., Zagros fold-and-thrust belts, Iran; Sabah fold-and-thrust belts, South China Sea; Perdido fold-and-thrust belts, Gulf of Mexico; and Niger fold-and-thrust belts, West Africa (Morley et al., 2011)). Hence, a better understanding of in situ conditions and physical properties also provides insights toward predicting reservoir quality, and designing safe and economic exploration programs.

Thin-skinned fold-and-thrust belts are often studied using critical taper theory (Dahlen, 1990; Dahlen and Suppe, 1988; Davis et al., 1983) or similar large-scale force-balance approaches in which the wedge is treated as a perfectly plastic or a nonlinear viscous material (Chapple, 1978; Platt, 1986). These systems are characterized by a wedge-shaped deformation region and a basal décollement (or detachment). These theories are based on the concept that the wedge is at failure throughout, and draw analogies from snow accumulating in front of a snowplow (Dahlen, 1990). In the case of critical taper theory, wedge geometry is controlled by the combined effects of the internal friction coefficient, basal friction coefficient, and pore-fluid pressure distribution (Dahlen, 1990; Dahlen and Suppe, 1988; Davis et al., 1983).

While critical taper theory provides insight into the relations among pore pressure, material strength, and wedge geometry, it does not address the mechanics of sediment deformation within and beneath the wedge. Sediments in the wedge experience great horizontal shortening and vertical thickening caused by lateral tectonic loading. As a result, systematic changes in porosity occur within and below wedges. For example, analyses of drilling cores and seismic velocities in the Nankai accretionary wedge indicate that the average sediment porosity in the wedge is lower than that outboard of the wedge (Karig, 1986; Tsuji et al., 2008). Other studies have shown a systematic decrease in porosity with both depth and distance from the wedge front (Bekins and Dreiss, 1992; Morgan et al., 1994). Negative-polarity reflections, low P-wave velocity (V_p), and sharp increases of porosity beneath the décollement all suggest that the footwall sediment is also much less compacted than the wedge sediment (Bangs et al., 2004; Hyndman et al., 1993; Saffer and Tobin, 2011; Tobin et al., 1994).

Critical state soil mechanics provide a tool for understanding and quantifying sediment deformation within critically tapered wedges. This family of soil models (e.g., Modified-Cam-Clay [MCC] (Roscoe and Burland, 1968; Wood, 1990)) describes the sediment as an elastoplastic material in which porosity is a function of both mean effective and deviatoric stresses (Wood, 1990). Thus, in geologic systems with complex stress histories, such as fold-and-thrust belts, critical state models offer a more geologically and mechanically appropriate approach to simulate compaction than simple uniaxial models. Karig (1986) first introduced critical state soil mechanics in the study of fold-and-thrust belts and illustrated possible compaction paths. Kitajima (2012) applied triaxial experiments to simulate sediment compaction under various stress paths and showed that the MCC model can describe stress and compaction behavior in the Nankai fold-and-thrust

belt. Hauser et al. (2014) showed that incorporating shear stresses into the compaction relationship using critical state soil mechanics significantly improves stress and pressure prediction in the Sabah fold-and-thrust belt. Most recently, critical-state soil mechanics was coupled with critical taper theory to predict in situ stress and pore pressure in the Nankai fold-and-thrust belt (Flemings and Saffer, 2018).

Numerical models that incorporate these realistic soil behavior in large-scale deformation provide an exciting way to explore the evolution of a range of geologic systems. Recent studies include large-strain salt-basin evolution (Heidari et al., 2016; Nikolinakou et al., 2014; Obradors-Prats et al., 2016), fault slip (Albertz and Lingrey, 2012; Crook et al., 2006), and anticline development (Rance et al., 2013). In the study of fold-and-thrust belts, Stauffer and Bekins (2001) applied MCC in coupled models to study compaction in accretionary wedges, but the loading source was prescribed and applied only vertically. Rowe et al. (2012) used MCC material and a displacement boundary to investigate the local stress and the deformation field near a frontal thrust; however, the wedge geometry was initially prescribed, and the compaction behavior was not discussed in detail. Obradors-Prats et al. (2017) also applied a geomechanical model to investigate structural styles and stress evolution inside a wedge. Few studies have focused on the detailed evolution of stress and compaction in fold-and-thrust belts from the onset of tectonic loading, while incorporating the impacts of basal friction on the sediments both above and below the décollement.

Here, we study marine accretionary prisms and their land-counterpart fold-and-thrust belts using a large-strain, plane-strain geomechanical model. For the remainder of the paper, we refer to these systems as “fold-and-thrust belts.” However, we emphasize that we are focusing on the leading edge of fold-and-thrust belt systems where temperature

effects are limited and boundary conditions can be described by a single, planar, décollement. We limit our analysis to drained or hydrostatic pressures, modeling sediments as poro-elastoplastic using a critical state model, without prescribing stress orientations or stress ratios. We show that we are able to simulate a geometry that correctly reproduces the predictions of the critical-taper theory. In addition, we explore stress coupling across the décollement and the stress state beneath it. Our approach enables us to illuminate the evolution of both stress and porosity in these systems, showing that both the mean effective and the deviatoric stresses within the wedge are significantly higher than those beneath it. Our results also simulate the abrupt change in porosity across the décollement often observed in these systems.

2.2 MODEL DESCRIPTION

We use Elfen finite-element software (Rockfield, 2017) to simulate fold-and-thrust belts. Simulations are plane strain (i.e., there is no strain out of plane) and are based on a finite-strain, quasistatic, explicit, Lagrangian formulation, complemented by automated adaptive-remeshing techniques (Peric and Crook, 2004; Thornton et al., 2011). A new mesh of elements is generated once a set of predefined criteria for element distortion is exceeded in any region in the model (Perić et al., 1999). Analyses are drained: simulations are based on effective stress analysis assuming hydrostatic pore pressure (Appendix A). Gravitational body force is included.

2.2.1 Model Setup

We initialize the model with two horizontal layers representing sediments above and below the décollement (Figure 2.1a). The upper layer is 3-kilometers (km) thick, and

the lower layer is 2-km thick. The model domain is 250-km wide. A wedge is formed by the advancement of a displacement boundary on the top layer, and it grows gradually by continuously incorporating the material from at the wedge front (Figure 2.1b). A rigid wall simulates the backstop.

The right edge is restrained laterally (roller boundary), and the bottom of the model is restrained vertically and laterally. Frictional contact exists between the upper- and lower-sediment layers (Figure 2.1a), with a constant friction coefficient μ_b (base case [Model 1]: $\mu_b=0.2$; Table 2.1). The friction coefficient of the contact between the left rigid wall and the sediment is assumed to be constant and equivalent to the sediment internal friction coefficient, $\mu_s = 0.44$. There is no cohesion in sediments nor at contacts throughout the domain. We simulate tectonic movement by displacing the rigid block at the left edge of the model with a steady rate of 2 mm/yr from the left end of the modeling domain to a final displacement of 85 km (Figure 2.1b). In drained and quasi-steady state models, such as presented here, the results are independent of the displacement rate. This contrasts the case of coupled models that simulate overpressure, where the rate of displacement will impact the pore pressure.

2.2.2 Sediment Behavior

The bulk density of the sediment is a function of porosity and it evolves with stress changes (Eq. A3, Appendix A). We describe the sediment constitutive behavior with the SR3 soil model (Crook et al., 2006) available in the Elfen finite-element software. SR3 is an elastoplastic constitutive model based on critical state soil mechanics (Wood, 1990). Critical-state soil mechanics introduces the concept that compaction depends on both mean effective stress and deviatoric stress—a fundamental advance on poroelastic models that

assume volumetric deformation depends only on mean effective stress (e.g., (Wang, 2017)).

Figure 2.2 illustrates basic features of the SR3 model in mean effective stress (σ'_m) and deviatoric stress (q) space, defined as follows:

$$\sigma'_m = \frac{\sigma'_1 + \sigma'_2 + \sigma'_3}{3}, \quad (1)$$

$$q = \sqrt{\frac{(\sigma'_1 - \sigma'_2)^2 + (\sigma'_2 - \sigma'_3)^2 + (\sigma'_3 - \sigma'_1)^2}{2}}, \quad (2)$$

where σ'_1 , σ'_2 , and σ'_3 are maximum, intermediate, and minimum principal effective stresses, respectively. We define this ratio of deviatoric stress to mean effective stress as shear-stress ratio: $\eta = \frac{q}{\sigma'_m}$.

The critical state line (red line, Figure 2.2a) defines the maximum deviatoric stress that the sediment can withstand under a given mean effective stress. The critical state lines plotted in this paper are derived under conventional triaxial compression condition ($\sigma'_1 > \sigma'_2 = \sigma'_3$). Under this condition, the critical state line represents the Mohr-Coulomb shear failure line in the σ'_m - q space. Under plane-strain conditions, and in the conventional plane-strain stress space $(\frac{\sigma'_1 + \sigma'_3}{2}, \frac{\sigma'_1 - \sigma'_3}{2})$, we expect the SR3 critical state line to lie slightly higher than the Mohr-Coulomb shear failure line, based on Modified Cam Clay theory (Roscoe and Burland, 1968).

Under conventional triaxial compression condition, in σ'_m and q space, the slope of the SR3 critical state line (η_{CS}) is:

$$\eta_{CS} = \tan\beta \left[(n_{sr3} + 1)^{\frac{1}{n_{sr3}}} \right], \quad (3)$$

where β is a friction parameter, and n_{sr3} is a material constant that describes the asymmetry of the yield surface (gray curves, Figure 2.2a). The equation for the yield surface is given in the Appendix B, together with the full list of input parameters (Table

2.3). In our base case (Model 1), β and n_{sr3} are 60^0 and 1.3, respectively, resulting in a slope of critical-state line $\eta_{cs} = 0.91$ (Eq. 3).

The friction parameter β is closely related to the internal friction angle (ϕ'_s). Under conventional triaxial compression, in $\sigma'_m - q$ space, the slope of the SR3 critical state line (η_{cs}) is equivalent to the slope of the MCC critical state line (η^*) (Wood, 1990):

$$\eta^* = \frac{6\sin\phi'_s}{3-\sin\phi'_s}. \quad (4)$$

We combine Equations 3 and 4 to express the internal friction angle ϕ'_s (or internal friction coefficient μ_s) as a function of the friction parameter β and n_{sr3} :

$$\phi'_s = \text{asin} \left\{ \frac{3\tan\beta \left[(n_{sr3}+1)^{-\frac{1}{n_{sr3}}} \right]}{6+\tan\beta \left[(n_{sr3}+1)^{-\frac{1}{n_{sr3}}} \right]} \right\}, \quad (5)$$

In our base case (Model 1), β and n_{sr3} are 60^0 and 1.3, respectively. This equates to $\phi'_s = 23.5^0$ (Eq. 5). The corresponding internal friction coefficient (μ_s) is:

$$\mu_s = \tan(\phi'_s) = 0.44 \quad (6)$$

We initialize stresses by assuming uniaxial-strain burial loading. Under this assumption, horizontal effective stresses develop as a constant ratio, K_0 , of the vertical effective stress. K_0 is a function of the material frictional strength and elastoplastic properties. Here we assume a K_0 value of 0.8. As the sediment is being loaded, it follows the K_0 stress path (black line, Figure 2.2a). By substituting $\sigma'_2 = \sigma'_3$ with $K_0\sigma'_1$ ($K_0 = 0.8$) in both Equation 1 and Equation 2, we solve η_{K_0} to be 0.23 (black line, Figure 2.2a).

The green, purple, and cyan curves (Figure 2.2a) are isovolumetric (iso-porosity) surfaces. The form of the iso-porosity curves shows that both the mean effective stress (σ'_m) and the deviatoric stress (q) contribute to sediment compaction. For example, a rock with a porosity of 23% ($n = 0.23$, purple iso-porosity in Figure 2.2a) can support a mean effective stress of 45 MPa under isotropic stress conditions ($\eta = 0$); the same rock can

support only ~ 30 MPa mean effective stress if it lies on the critical state line ($\eta = \eta_{cs}$). In other words, compaction depends on the shear-stress ratio (η); the higher this ratio, the lower the porosity for the same mean effective stress (Figure 2.2b).

2.2.3 Modeling Scenarios

As a base case (Model 1, Table 2.1), we assume a basal friction coefficient $\mu_b = 0.2$ and an internal friction coefficient $\mu_s = 0.44$. The equivalent basal friction and internal friction angles are $\phi_b = 11^\circ$ and $\phi'_s = 24^\circ$, respectively. We constrain the basal friction coefficient (μ_b) and the internal friction coefficient (μ_s) to be within in the range of the mudrock properties in the Nankai fold-and-thrust belt, based on the laboratory experiments and predictions from analytical model ($\mu_s = 0.5 \pm 0.1$, $\mu_b = 0.2 \pm 0.1$, (Davis et al., 1983; Lallemand et al., 1994; Nemcok et al., 2009)). We then conduct sensitivity analyses of the friction parameters μ_s and μ_b to investigate their effects on stress state and compaction behavior, both within the wedge and in the footwall sediments (Tables 1 and 2). Specifically, we examine the effect of a décollement with basal friction coefficients μ_b varying from 0.1 to 0.3 (Table 2.1, equivalent $\phi_b = 6^\circ - 17^\circ$). We also investigate the effect of sediment internal friction coefficient by varying internal friction coefficient μ_s from 0.36 to 0.53 (Table 2.2, $\phi'_s = 20^\circ - 28^\circ$).

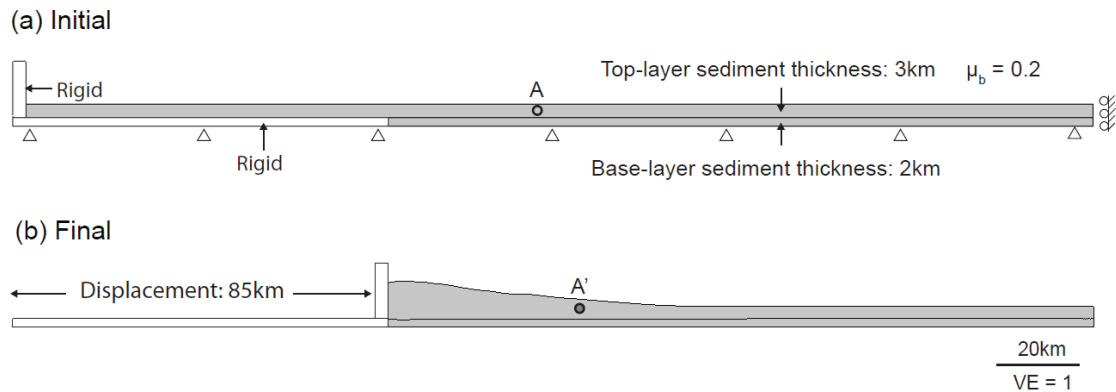


Figure 2.1: Model set-up and boundary conditions. (a) Model setup. Upper and lower layers are 3 km and 2 km thick, respectively. Only vertical movement is allowed at right boundary (roller); both horizontal and vertical movements are restricted at base. Rigid block on left boundary is displaced from left to right. Left end of base layer is rigid to minimize edge effects. Contact between layers represents décollement and is assigned a constant friction coefficient μ_b . Contact between rigid moving block and top layer is assigned friction coefficient $\mu_w = \mu_s = 0.44$. (b) Final deformation after 85 km of displacement of base case (Model 1; Table 2.1). Point A and point A' represent sediment element before (top) and after (bottom) deformation. See Figure 7 for its corresponding stress and compression paths.

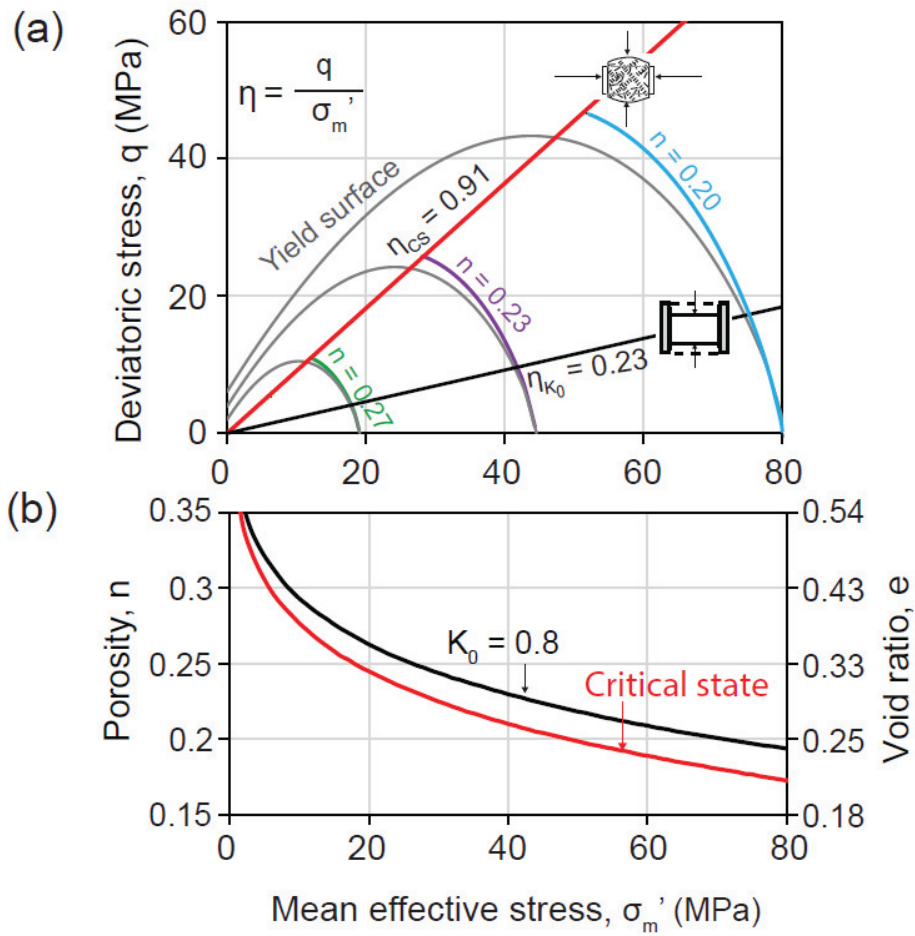


Figure 2.2: Basic principles of critical state model SR3: (a) Mean effective vs. deviatoric stress plot. Gray solid curves represent yield surfaces for different preconsolidation pressures. Red line represents critical state line for internal friction angle $\phi'_s = 23.5^\circ$ (Eq.4). Solid black line represents uniaxial (K_0) compression stress path with $K_0=0.8$. Green, purple, and cyan arc curves are iso-porosity curves. (b) Compaction curves. Black curve is K_0 compaction curve. Red curve is critical-state compaction curve.

Table 2.1: Impact of basal friction on surface angle, stress ratios, and principal stress orientations

μ_b	μ_s	α ($^{\circ}$)	σ'_1 dip wedg e ($^{\circ}$)	σ'_x/σ'_z wedge	σ'_1 / σ'_3 wedg e	q/σ'_m wedg e	σ'_1 dip foot. ($^{\circ}$)	σ'_x/σ'_z foot.	σ'_1 / σ'_3 foot.	q/σ'_m foot.	#
.10	.44	2.2	4.0	2.5	2.5	0.85	72	0.76	1.4	0.35	2
.15	.44	3.5	5.7	2.5	2.4	0.82	66	0.77	1.5	0.40	6
.20	.44	5.0	7.4	2.4	2.5	0.85	62	0.76	1.6	0.48	1
.25	.44	6.0	9.5	2.4	2.5	0.85	58	0.79	1.8	0.56	7
.30	.44	8.2	10.2	2.4	2.5	0.84	54	0.83	1.9	0.61	3

Note: Columns 1–3: basal friction coefficient, internal friction coefficient, surface slope angle. Columns 4–7: maximum principal stress orientation in wedge, horizontal-to-vertical stress ratio in wedge, maximum-to-minimum principal stress ratio in wedge, shear-stress ratio in wedge. Columns 8–11: orientations and stress ratios in footwall. Column 12: model number. For consistent comparison, the locations are chosen such that the sediment above décollement is 4km thick and sediment below décollement is 2km thick. The stress ratios and stress orientations are estimated by taking the average value of the hanging wall 4km sediment (wedge), and by taking the average value of the footwall 2km sediment (foot.).

Table 2.2: Impact of internal friction on surface angle, stress ratios, and principal stress orientations

μ_b	μ_s	α ($^\circ$)	σ'_1 dip wedge ($^\circ$)	σ'_x/σ'_z wedge	σ'_1/σ'_3 wedge	q/σ'_m wedge	σ'_1 dip foot. ($^\circ$)	σ'_x/σ'_z foot.	σ'_1/σ'_3 foot.	q/σ'_m foot.	#
.20	.36	6.0	11	2.0	2.1	0.69	58	0.83	1.6	0.43	4
.20	.40	5.2	8.2	2.3	2.4	0.79	61	0.78	1.6	0.47	8
.20	.44	5.0	7.4	2.4	2.5	0.85	62	0.76	1.6	0.48	1
.20	.48	4.9	5.8	2.8	2.8	0.94	63	0.75	1.7	0.50	9
.20	.53	4.5	5.0	3.1	3.1	1.0	64	0.74	1.7	0.51	5

Note: Columns 1–3: basal friction coefficient, internal friction coefficient, surface slope angle. Columns 4–7: maximum principal stress orientation in wedge, horizontal-to-vertical stress ratio in wedge, maximum-to-minimum principal stress ratio in wedge, shear stress ratio in wedge. Columns 8–11: orientations and stress ratios in footwall. Column 12: model number. For consistent comparison, the locations are chosen such that the sediment above décollement is 4km thick and sediment below décollement is 2km thick. The stress ratios and stress orientations are estimated by taking the average value of the hanging wall 4km sediment (wedge), and by taking the average value of the footwall 2km sediment (foot.).

2.3 MODEL RESULTS

In Model 1, after 85 km of displacement, a self-similarly growing and critically tapered compressive wedge has formed. The wedge surface dips at approximately 5° and merges with the originally horizontal sediment surface (Figure 2.3a).

2.3.1 Stress

The wedge fails in shear and the ratio of maximum-to-minimum principal effective stress (Figure 3a) is approximately constant within the wedge region ($\frac{\sigma'_1}{\sigma'_3} = 2.5$) and is much higher than that in the footwall ($\frac{\sigma'_1}{\sigma'_3} = 1.6$) or the far field ($\frac{\sigma'_1}{\sigma'_3} = 1.25$). The ratio of maximum-to-minimum effective stress in the wedge is slightly more than predicted by Coulomb failure (i.e. Rankine passive failure) for a cohesionless material (Dahlen, 1990; Rankine, 1857):

$$\frac{\sigma'_1}{\sigma'_3} = \frac{1+\sin\phi'_s}{1-\sin\phi'_s} = 2.3 \quad (\phi'_s = 23.5^\circ). \quad (7)$$

The reason for the discrepancy is that under plane-strain conditions, the slope of the critical state line in an average stress vs. maximum shear stress plot ($\frac{\sigma'_1+\sigma'_3}{2}, \frac{\sigma'_1-\sigma'_3}{2}$) is slightly higher than that of the Mohr–Coulomb shear-failure line (Roscoe and Burland, 1968).

Shear stress along the base of the wedge, τ_{xz} (red line, Figure 2.3b), equals the basal strength $\mu_b\sigma'_z$ (cyan dash-line, Figure 2.3b): the sediment is sliding along the décollement (labeled “Sliding” in Figure 2.3b). Sliding stops approximately 75 km from the moving wall, in the region where $\mu_b\sigma'_z$ and τ_{xz} diverge (“No sliding,” Figure 2.3b).

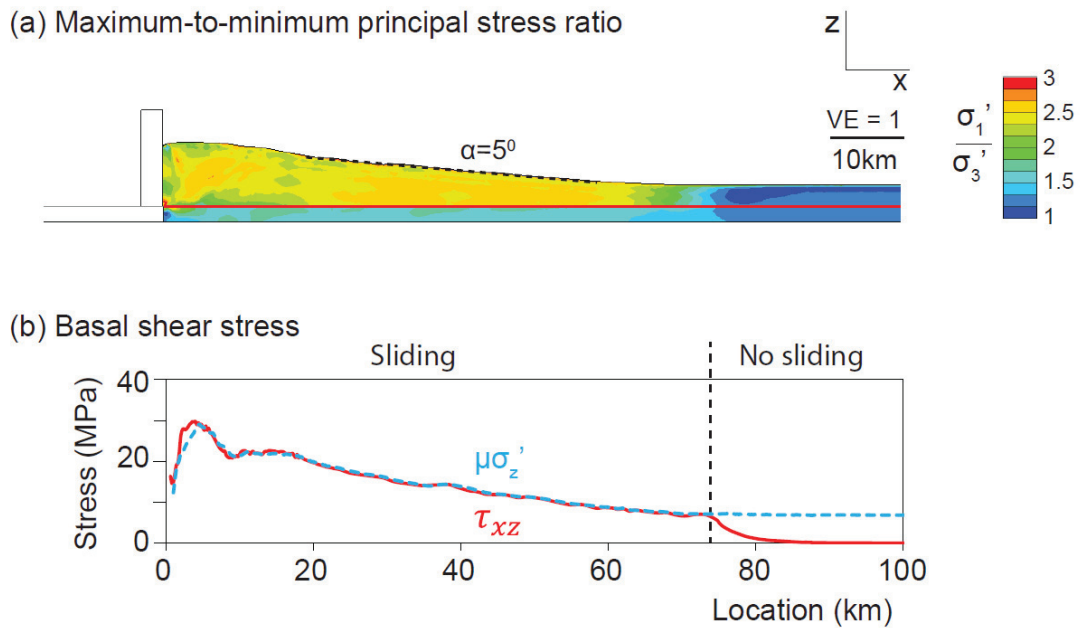


Figure 2.3: (a) Maximum-to-minimum principal effective stress ratio distribution. Wedge surface slope is about 5° . Very left portion (close to rigid wall boundary) is excluded from our ensuing analysis because of edge effects. (b) Shear stress along décollement (red line in [a]) and threshold value for sliding along décollement (cyan dash-line). Sliding zone: $\tau_{xz} = \mu_b \sigma'_z$. No-sliding zone: $\tau_{xz} < \mu_b \sigma'_z$.

Within the wedge, horizontal effective stress is approximately 2.5 times greater than vertical effective stress (orange area, Figure 2.4a, b). In contrast, beneath the wedge, horizontal stress is a fraction of vertical effective stress ($\sigma'_x/\sigma'_z = 0.76$). As a result, an abrupt drop in both horizontal and mean effective stresses occurs beneath the décollement (Figure 2.4b). In the far field (profile B, Figure 2.4a), horizontal, vertical, and mean effective stress continuously increase with depth (Figure 2.4c); the sediment is still at the uniaxial strain K_0 condition, where $\sigma'_x/\sigma'_z = K_0 = 0.8$. As the wedge evolves, material outside it is incorporated either into the wedge or subsumed beneath it. The material consumed into the wedge undergoes a much larger change in stress, because it is driven from K_0 conditions to failure under horizontal compression. In contrast, the material beneath the décollement is at a stress state close to, but at a higher shear stress than, K_0 conditions.

We consider the principal stress orientations immediately above and below the décollement (red and black dots, Figure 2.5b). In Figure 2.5a, the big red Mohr circle and small black Mohr circle represent the stress states above and below the décollement, respectively (Figure 2.5a, b). In Model 1, the maximum principal effective stress dips 7° seaward relative to the horizontal; in contrast, it dips 62° in the footwall (Figure 2.5a–c). Although horizontal effective stresses are different across the décollement (Figure 2.4b), the shear (τ_{xz}) and normal stresses (σ'_z) acting on the décollement are continuous (Figure 5a).

A vertical profile through the wedge (profile A, Figure 2.6b) illustrates that sediments throughout the wedge are at failure, the shear-stress ratio, $\eta = 0.91$, indicating that the stress state lies on the critical state line (red circles, Figure 2.6d). In contrast, stress states within the footwall are well below the critical state line (green triangles, Figure 2.6d),

with a shear-stress ratio of 0.48 (green area, Figure 2.6b). The stress states within the footwall lie between the critical state line and the K_0 compression line, indicating a level of shear that is higher than uniaxial but lower than failure. Stress states along a vertical profile in the far field (profile B, Figure 2.6b) maintain the uniaxial-strain stress ratio $\eta = 0.23$ (blue squares, Figure 2.6d). Between the critical-state wedge and the far field is the transition zone, where the shear-stress ratio gradually decreases from the critical state value to the uniaxial- strain compression value (red-cyan, Figure 2.6b).

2.3.2 Stress Evolution and Porosity Change

We track the evolution of mean effective stress and deviatoric stress for a sediment element that is initially outside the wedge and then incorporated into the wedge as deformation proceeds (point A, Figure 2.1). Initially, the shear-stress ratio lies along the K_0 (uniaxial) stress line ($\eta = 0.23$) (point A [empty circle], Figure 2.7a). As lateral stress increases, mean effective stress and deviatoric stress also increase (blue line, Figure 2.7a), and the stress path evolves from the K_0 stress state (up and to the right on the mean effective vs. deviatoric stress plot). Eventually, the sediment element is fully incorporated into the wedge (point A', Figure 2.1b), the deviatoric stress reaches the critical state condition, and the sediment fails in shear (point A' [filled circle], Figure 2.7a).

Porosity declines 8.5 porosity units along this stress path (Figure 2.7b). We deconstruct this porosity decline into that caused by the change in mean effective stress (Δn_m) and that caused by the change in shear-stress ratio (Δn_s). Δn_m is the change in porosity along the K_0 compression line from the initial to the final mean effective stress; it equals 5.5 porosity units (Figure 2.7b). Δn_s is the difference between the porosity at the final stress state on the K_0 compression line and the porosity at the final stress state on the critical state line; it equals 3 porosity units (Figure 2.7b). Thus, the shear-induced

compaction (Δn_s) accounts for 35% of total porosity reduction as the sediment enters the fold-and-thrust belt.

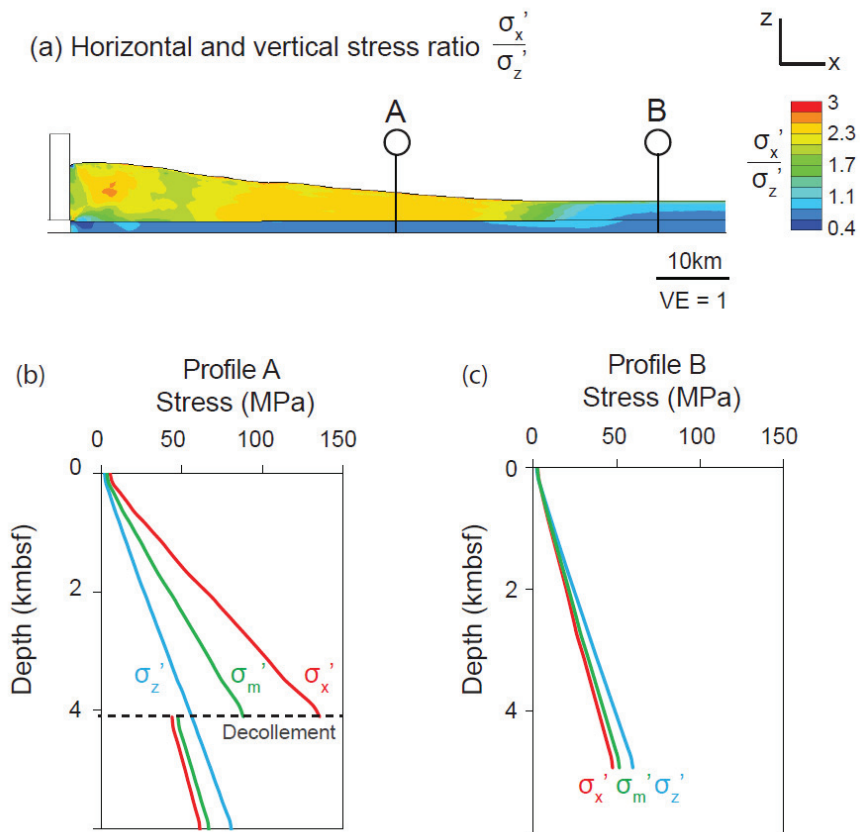


Figure 2.4: (a) Horizontal-to-vertical effective stress ratio at end of simulation. (b) Horizontal (red), vertical (cyan), and mean (green) effective stresses along profile A of (a). (c) Horizontal, vertical, and mean effective stresses along profile B of (a).

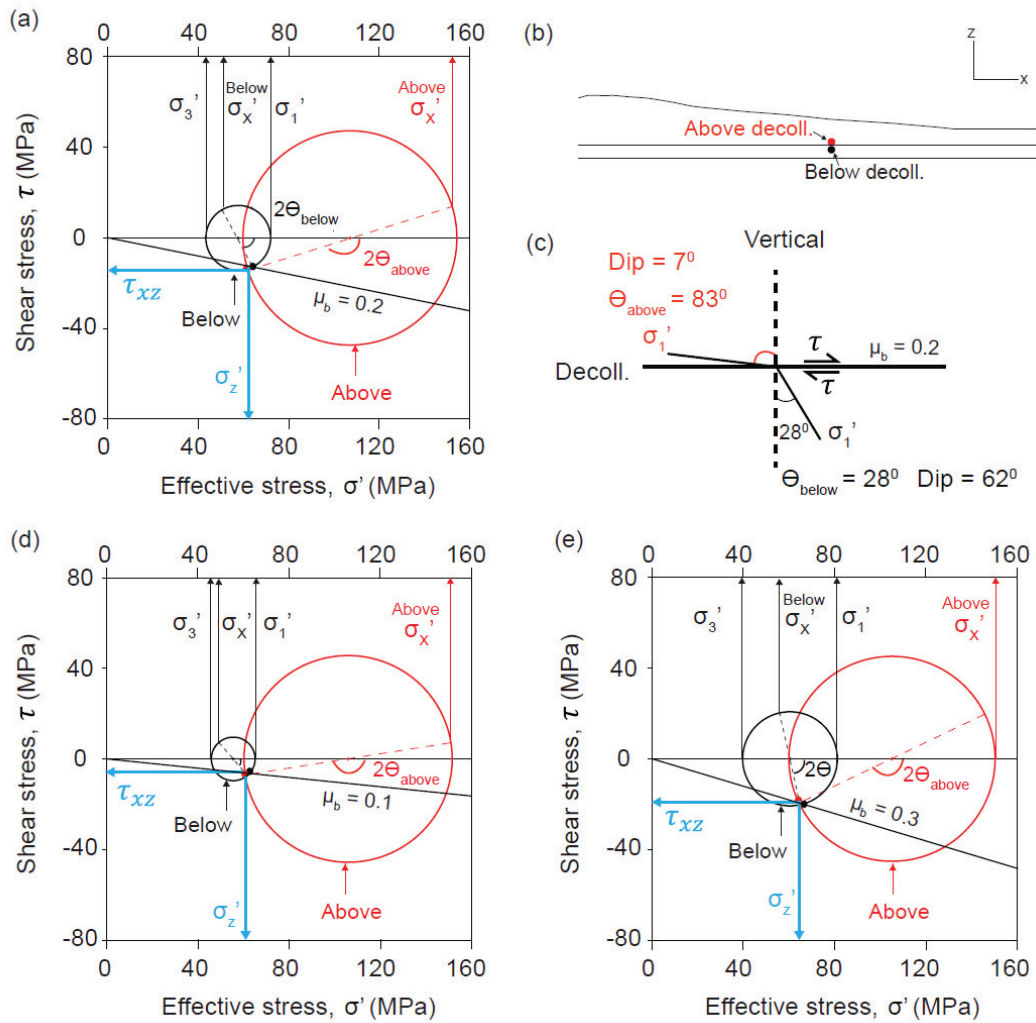


Figure 2.5: Comparisons of stress-state and principal-effective-stress orientations at décollement with three different basal friction coefficients, μ_b . (a) Stress state for $\mu_b = 0.2$. Red and black circles represent stress states for sediment just above and below décollement (illustrated in [b]). Red θ represents angle between maximum principal effective stress (σ_1') orientation in wedge to vertical direction (illustrated in [c]). Black θ represents angle of σ_1' to vertical in footwall. (b) Schematic figure showing locations of plotted stress points just above and below décollement. (c) Summary of stress orientations in (a). (d) Stress state for $\mu_b = 0.1$. (e) Stress state for $\mu_b = 0.3$.

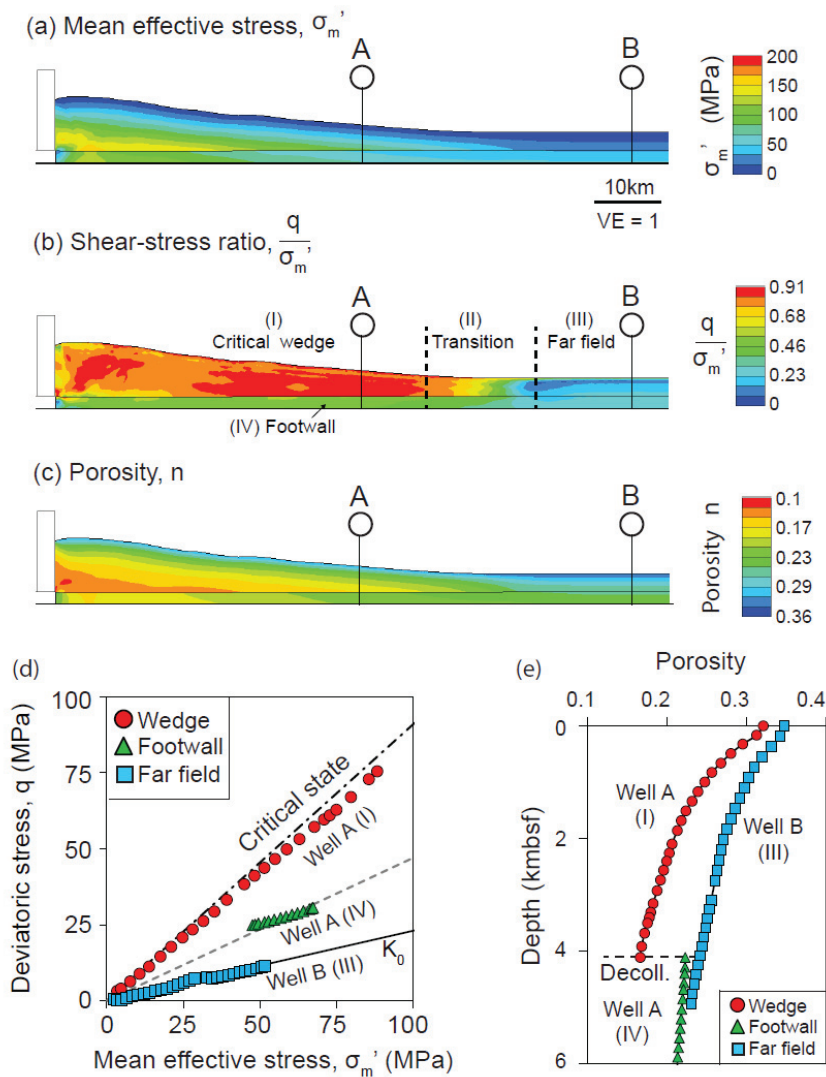


Figure 2.6: (a) Mean effective stress at end of system evolution. (b) Shear-stress ratio. Shear-stress ratios are approximately constant in wedge (0.91), footwall (0.47), and far field (0.23); they vary in transition zone. (c) Porosity. (d) Mean vs. deviatoric stress plot along profile A (red circles: wedge [I]; green triangles: footwall [IV]), and along far-field profile B (cyan squares: far field [III]). (e) Porosity along profiles A and B (depth referring to thousand-meter below seafloor). Red circles: along profile A in wedge (I). Green triangles: along profile A in footwall (IV). Cyan squares: along profile B in far field (III).

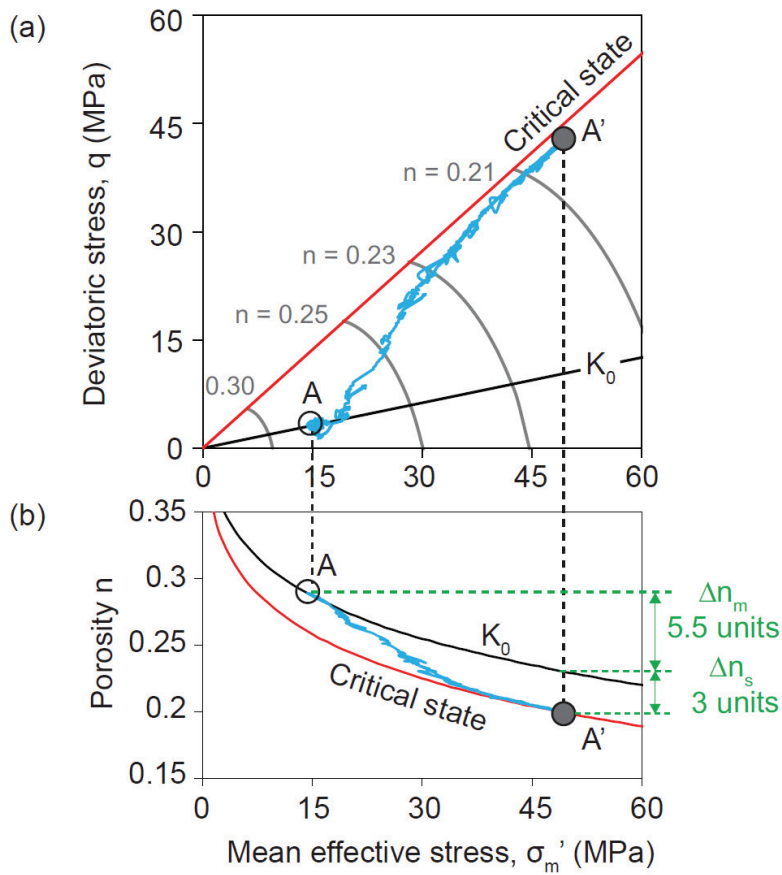


Figure 2.7: Stress and compaction history for sediment that moves from initial point A to final point A' (Figure 1). (a) Stress path showing mean effective and deviatoric stress evolution. Gray curves are isoporosity surfaces. (b) Porosity as a function of mean effective stress. Porosity starts from uniaxial value on K_0 compaction line (black) and ends on critical state line (red). During tectonic loading, mean effective stress causes porosity reduction of 0.055 ($\Delta n_m = 0.055$), and shear stress contributes an additional reduction of 0.03 ($\Delta n_s = 0.03$).

The difference in the stress path that material undergoes above and below the décollement results in porosity differences between the wedge and footwall. Porosity in the footwall is slightly lower at a given depth than in the far field and is significantly higher (6 porosity units) than the porosity in the wedge immediately above the décollement (Figure 2.6e).

2.3.3 Sensitivity Analysis

2.3.3.1 Impact of Basal Friction Coefficient

We compare Model 1 (base case), which had a basal friction coefficient of 0.2, with models with basal coefficients of $\mu_b = 0.1$ (Model 2, Table 2.1) and $\mu_b = 0.3$ (Model 3, Table 2.1), while holding all other parameters constant. The surface slope angle (α) increases with μ_b (Figure 2.8a–c) and is consistent with predictions of critical taper theory (gray line, Figure 9a). The surface angle predicted by critical taper theory is calculated by applying equation 30 in Davis et al. (1983), representing the dry sandbox case.

Increasing the basal friction coefficient also impacts stress orientations. The dip angle of the maximum principal effective stress (σ_1') in the wedge increases from 4° to 10° , as μ_b increases from 0.1 to 0.3 (red diamonds, Figure 2.9b). This increase is also consistent with orientations of the maximum principal stress from critical taper theory (gray line, Figure 2.9b). Below the décollement, as the basal friction increases from 0.1 to 0.3, the dip angle of σ_1' decreases from 72° to 54° (blue dots, Figure 2.9b).

These systematic changes in principal stress orientations are caused by increased shear stress along the décollement. For each model ($\mu_b=0.1, 0.2,$ and 0.3), we plot the stress state of the sediment just above the décollement inside the wedge, and just below the

décollement inside the footwall (Figure 2.5b). As the basal friction coefficient increases, the shear stress τ_{xz} at the contact increases. Specifically, an increase in μ_b , from 0.1 to 0.3, increases τ_{xz} from 8 MPa to 20 MPa (Figure 2.5d, and Figure 5e). As a result, the maximum principal effective stress rotates toward vertical in the wedge and toward horizontal in the footwall as the basal friction coefficient increases (Figure 2.5). The ratio of maximum-to-minimum principal effective stress in the footwall also increases as is illustrated by the increase in the Mohr Circle diameter.

Changing the basal friction coefficient does not impact the porosity profile within the wedge (profiles A–C, Figure 2.8e) because sediments inside the wedge are at critical state (circles, Figure 2.8d). At equivalent depths below the seafloor, mean effective stress is the same; because sediments are at critical state, the shear-stress ratio remains constant (equal to $\eta_{cs}=0.91$), and therefore deviatoric stress also remains the same. In contrast, increasing μ_b results in a lower porosity in the footwall (Figure 2.8e). The increased basal friction coefficient increases the mean effective stress and the deviatoric stress (Figure 2.8d), which increases compaction (Figure 2.8e). The porosity offset across the décollement decreases as the basal friction coefficient increases.

2.3.3.2 Impact of Sediment Internal Friction Coefficient

We next compare our base model (Model 1), which had an internal friction coefficient of 0.44 ($\phi'_s = 24^\circ$) against models with sediment internal friction coefficients μ_s equal to 0.36 ($\phi'_s = 20^\circ$) and 0.53 ($\phi'_s = 28^\circ$) (Models 4 and 5, respectively; Table 2.2), while holding all other parameters constant. As μ_s increases from 0.36 to 0.53, the measured surface slope α decreases from 6° to 4.5° (Figure 2.10a–c). These surface slopes are again consistent with critical taper theory predictions (gray line, Figure 2.9c). As μ_s increases, the dip angle of the maximum principal stress (σ'_1) decreases in the

wedge (red diamonds, Figure 2.9d) and slightly increases in the footwall (blue dots, Figure 9d). In the wedge, along the projected profiles (A–C, Figure 2.10), as μ_s increases from 0.36 to 0.53, the dip angles of the maximum principal stress decreases from 11° to 5° (red diamonds, Figure 2.9d). The σ'_1 orientations in the wedge are consistent with the critical theory predictions (gray line, Figure 2.9d). In the footwall, the maximum principal effective stress orientations are subvertical. The average dip angle along projected profiles (A–C, Figure 2.9d) increases from 58° to 64° as μ_s increases from 0.36 to 0.53 (blue dots, Figure 2.9d).

Sediment porosity decreases inside the wedge as the sediment internal friction coefficient increases. A higher internal friction coefficient means stronger sediments; therefore, the slope of the critical state line is higher. Shear failure occurs at a higher mean effective stress level, leading to a higher deviatoric stress at failure (e.g., orange dots, Figure 2.10d). Because both mean effective stress and deviatoric stress contribute to sediment compaction, a higher internal friction coefficient results in a greater porosity decrease. Therefore, the sediment is more compacted inside the wedge (purple, black, and orange lines, Figure 2.10e).

In the footwall, sediment porosity-depth trends (Figure 2.10e) for the three cases are similar to each other (triangles, Figure 2.10d). At equivalent depths to the seafloor, stress components remain the same because the basal friction coefficient is assumed constant; therefore, shear stress along the décollement does not change. As a result, the footwall exhibits little deviatoric stress or compaction differences between the models.

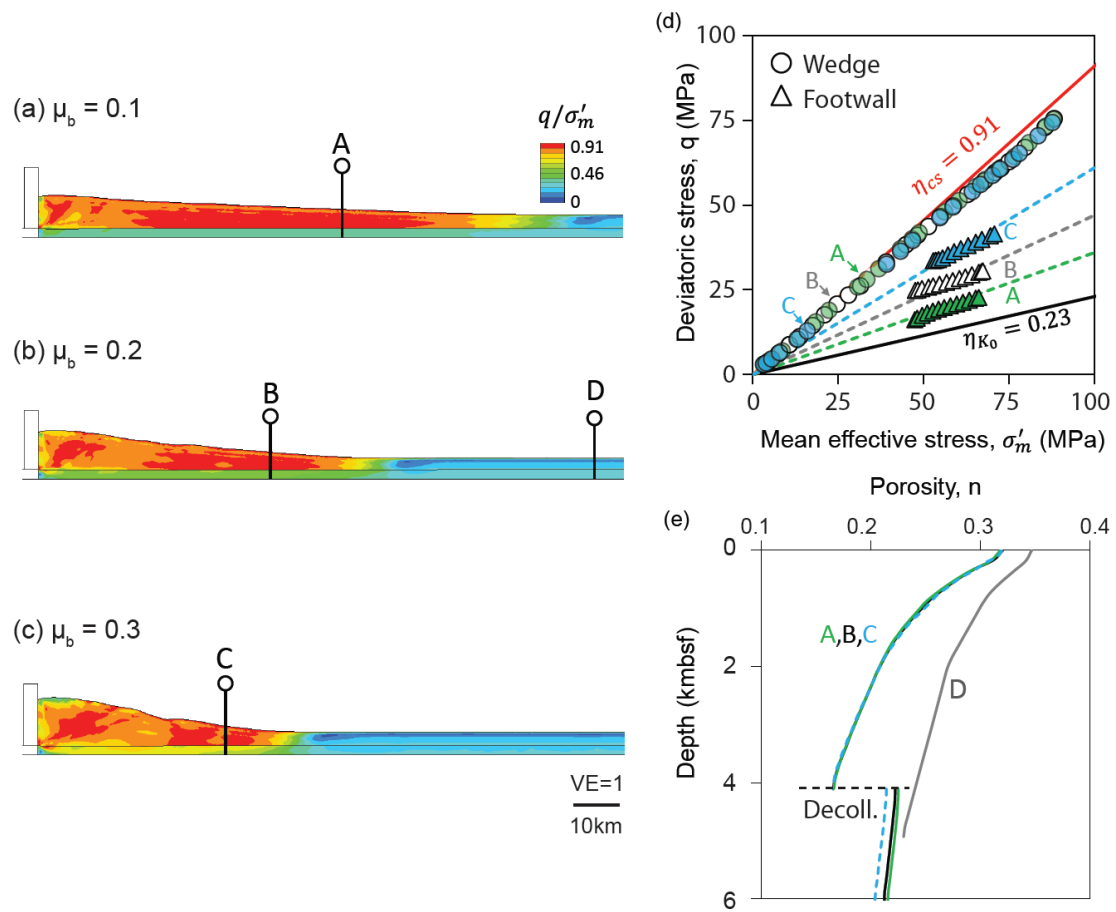


Figure 2.8: (a)–(c) Shear-stress ratio for models with basal friction $\mu_b = 0.1, 0.2,$ and $0.3,$ respectively. (d) Mean effective vs. deviatoric stress for sediment along profiles A ($\mu_b = 0.1$; green symbols), B ($\mu_b = 0.2$; white symbols), and C ($\mu_b = 0.3$; cyan symbols). Red and black solid lines represent critical state and uniaxial strain conditions, respectively. Circles represent stress states in wedge; triangles represent stress states in footwall. Dash lines show corresponding average shear-stress ratios for sediment in footwall: $\eta = 0.35$ (profile A), $\eta = 0.48$ (profile B), and $\eta = 0.61$ (profile C). (e) Porosity vs. depth trends along profiles of A, B, C, and D.

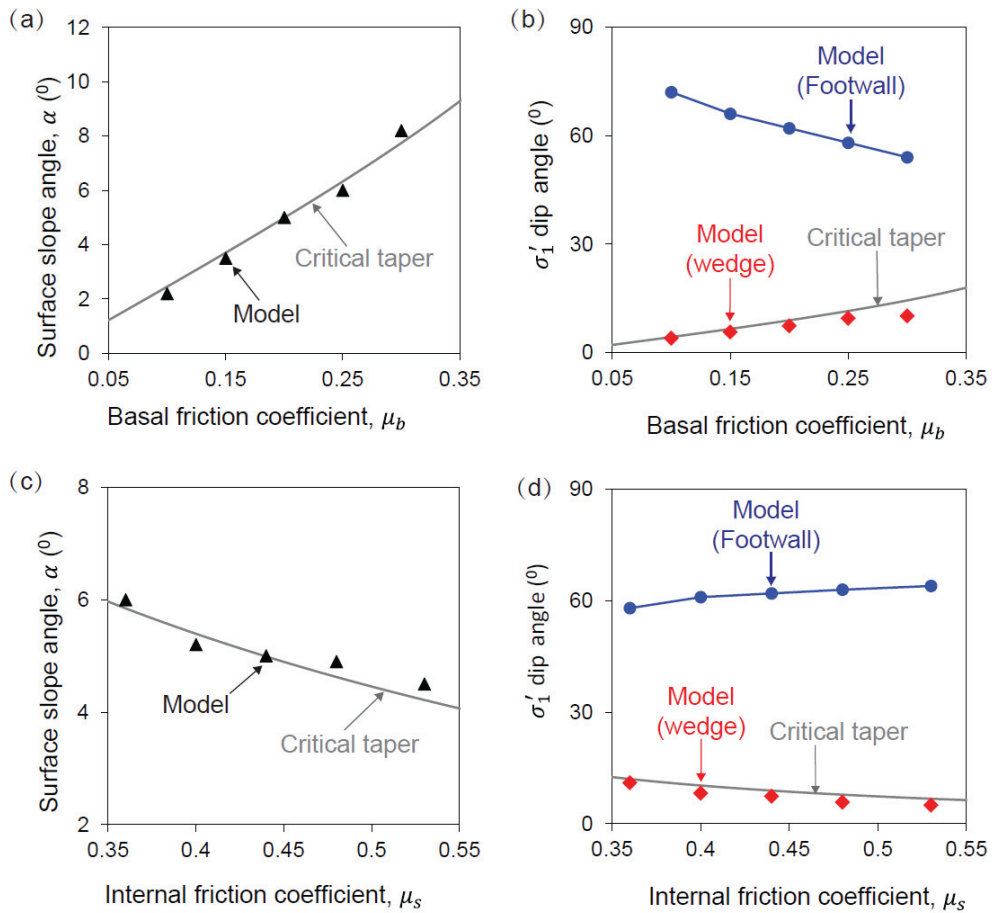


Figure 2.9: (a) Geomechanical model prediction (triangles) and critical taper theory prediction (gray line) of wedge surface-slope angle as a function of basal friction coefficient (μ_b varies; $\mu_s = 0.44$). (b) Maximum principal stress (σ'_1) dip angle predicted by geomechanical model in wedge (red diamonds) and in footwall (blue circles), as well as critical taper theory prediction (gray line). (c) Geomechanical model prediction (triangles) and critical taper theory prediction (gray line) of wedge surface-slope angle as a function of internal friction coefficient (μ_s varies; $\mu_b = 0.2$). (d) Maximum principal effective stress (σ'_1) dip angle predicted by geomechanical model in wedge (red diamonds) and in footwall (blue circles), as well as critical taper theory prediction (gray line).

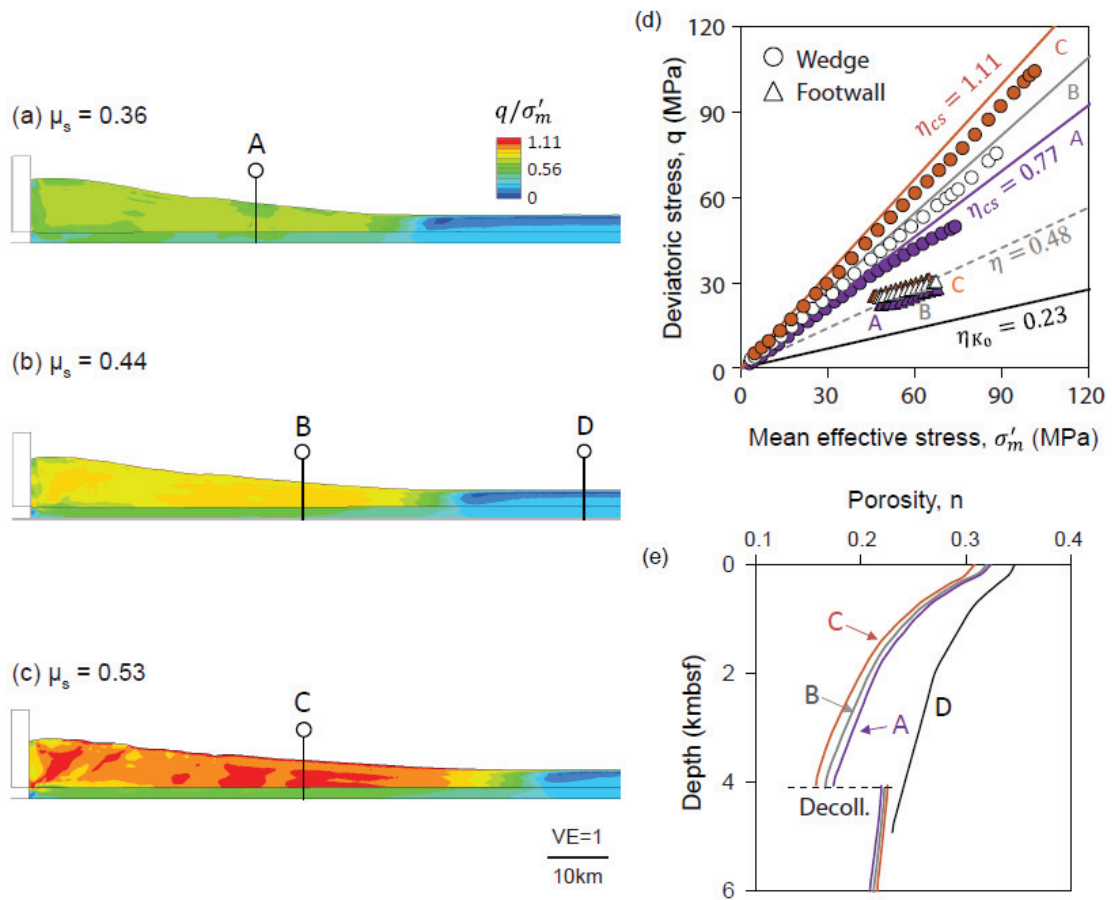


Figure 2.10: (a)–(c) Contours of shear-stress ratio for $\mu_s = 0.36, 0.44,$ and $0.53,$ respectively. (d) Shear-stress ratios along profiles A (purple), B (white), and C (orange). Black solid line represents uniaxial conditions. Circles and triangles show stress states in wedge and in footwall, respectively. Slope of critical state line is $\eta_{cs} = 0.77$ for $\mu_s = 0.36$ (purple line), $\eta_{cs} = 0.91$ for $\mu_s = 0.44$ (gray line), and $\eta_{cs} = 1.11$ for $\mu_s = 0.53$ (orange line). (e) Porosity vs. depth trends along profiles of A, B, C, and D.

2.4 DISCUSSION

We have used large-strain geomechanical models to simulate the evolution of fold-and-thrust belts under drained (hydrostatic) conditions. The simulations provide a range of insights into the underlying controls on compaction behavior, strain, and stress state in these complex environments.

2.4.1 Stress State

Our model results define four zones with distinct stress states (Figure 2.11). Outboard of the fold-and-thrust belt, the maximum principal effective stress equals the vertical effective stress, and the minimum principal effective stress is a fraction of the vertical effective stress (“Far-field,” Figure 2.11a). These sediments have undergone vertical uniaxial strain during burial. Inside the wedge (“Critical state wedge,” Figure 2.11a), the maximum principal stress dips slightly toward the décollement. Lateral stress is limited by the strength of the rock, which is defined as the maximum deviatoric stress that can be withstood at a given mean effective stress. Beneath the décollement (“Footwall,” Figure 2.11a), the maximum principal effective stress dips steeply and lateral effective stresses are a fraction of the vertical effective stresses. The sediments in the “Footwall” zone are dominated by vertical loading from the overlying sediment. However, some shear stress transmitted across the décollement disturbs the stress ratio from the far field (i.e. it is not in a K_0 state). Finally, the “Transition” zone, the stress state changes rapidly from the far-field conditions to critical state (“Transition,” Figure 2.11a).

As the décollement friction coefficient (μ_b) increases, maximum principal stress orientation within the wedge rotates from nearly horizontal to more steeply dipping, and the surface slope increases, as predicted by the critical taper theory (Figure 2.9a, b). There

is no impact on the shear-stress (η_{cs}) ratio within the wedge. Beneath the wedge, as μ_b increases, the maximum principal stress rotates from vertical to dipping steeply toward the décollement (Figure 2.9a, b). In addition, the ratio of σ'_1/σ'_3 increases because of greater traction along the décollement (Table 2.1; Figure 2.8). As the friction coefficient within the sediment increases (μ_s), the ratio of the q/σ'_m increases (Figure 2.10): the rock strength is increased and thus can withstand a higher deviatoric stress and a higher mean effective stress before failure. In addition, as μ_s increases, surface slope declines and the orientation of the maximum principal effective stress in the wedge becomes more horizontal (Figure 2.9c, d). Beneath the wedge, an increase in μ_s results in a very slight increase in the dip angle of σ'_1 (Table 2.2; Figure 2.9d).

We show that with low basal friction coefficients, the stress state is very close to that recorded for the uniaxial (K_0) strain condition. For many fold-and-thrust belts in a marine environment (e.g., Nankai, Barbados, and Cascadia), the estimated effective basal friction is less than 0.2 (Schott and Koyi, 2001; Sreaton et al., 2002; Wang and He, 1999). Thus, the common assumption of a near complete decoupling across the décollement and the interpretation of uniaxial strain conditions within the footwall (Housen et al., 1996; Saffer, 2003; Sreaton et al., 2002) is reasonable. We also find that while the deviatoric stress of footwall sediment increases as μ_b increases (Figure 8d), it never reaches critical state. Thus, footwall sediment is unlikely experience extensional shear failure or generate shear fractures. Therefore, in the footwall, we do not envision there to be fault permeability generated in the footwall.

2.4.2 Strain

Shortening and elongation occur concurrently as the sediment is incorporated into

a fold-and-thrust belt (Fig. 2.12a). We illustrate the sediment deformation by plotting the associated strain ellipses of a tracked sediment element (Figure 2.12a, b). Outside the wedge, the sediment is deformed under vertical uniaxial strain by burial and the minimum principal strain axis is horizontal (Pt. A, Figure 2.12a, b). As the sediment passes through the Transition Zone (Pt. A to Pt. B, Figure 2.12a), the minimum principal strain rotates toward vertical (gray line, Figure 2.12b). Before reaching the trench, the vertical strain (ϵ_z) approximately equals the maximum strain (ϵ_1), and the horizontal strain (ϵ_x) approximately equals the minimum strain (ϵ_3). Vertical and horizontal strains both remain shortening (positive) in the Transition Zone (Pt. A to Pt. B, Figure 2.12b). As the sediment passes from the trench into the wedge, the sediment experience horizontal shortening and vertical elongation (Pt. B to Pt. C, Figure 2.12b). The vertical strain becomes close to the minimum strain and the horizontal strain converges onto the maximum strain. Although there is both vertical elongation and horizontal shortening, the magnitude of the shortening strain is higher than that of the elongation strain, and the sediment is continually compacted (porosity decreases) (Figure 2.12c). These results are qualitatively very similar to those derived by Morgan et al. (1994) based on kinematic modeling. The results on strain rotation also show agreement with the strain analysis indicated from fabric orientations (Henry et al., 2003; Housen, 1997; Housen et al., 1996; Owens, 1993) and P wave anisotropy (Brückmann et al., 1997) of Nankai and Barbados fold-and-thrust belts.

2.4.3 Volumetric Change (Compaction)

The four stress zones (Figure 2.11) have distinct porosity–depth relationships. In the far field, porosity declines with depth monotonically at a lower rate than at all other locations. Within the wedge, porosity declines most rapidly with depth. At a given depth,

porosity in the wedge is lower than in the far field for two reasons: (1) mean effective stress is much larger because of the increase in lateral stress; and (2) the shear-stress ratio (η) is higher, resulting in more compaction at a given mean effective stress than under far-field conditions. Beneath the wedge, the porosity is slightly less than the far field at equivalent depths (green triangles vs. cyan squares, Figure 2.6e). This is because: (1) beneath the wedge, the overburden is greater because the overlying sediment is more compacted and hence its density is greater; and (2) there is additional shear transmitted across the décollement and this causes additional compaction. The Transition Zone is 10-30 km wide: a higher μ_b narrows the Transition Zone (Figure 2.8a-c). Within this zone, mean-effective and deviatoric stresses toward the thrust belt increase as the horizontal effective stress increases (Figure 2.11b); as a result, within the transition zone, porosity decreases toward the thrust belt at a given depth.

As material from the far field is incorporated into the wedge, the porosity decreases by 8.5 porosity units (0.085, Figure 2.12c). The majority of this porosity loss (6.4 porosity units) occurs as the sediment element passes through the Transition Zone (Pt. A to Pt. B, Figure 2.12c) where the sediment element transits from uniaxial stress conditions to compressional failure. Thereafter, as the sediment element passes across the critical state zone, porosity continues to decline but at a lower rate (Pt. B to Pt. C, Figure 2.12c). The compaction along this path is deconstructed into that caused by the change in vertical effective stress assuming under uniaxial-strain condition (Δn_{k_0}), the change in mean effective stress under non- K_0 conditions (Δn_m), and finally the change on shear stress under non- K_0 conditions (shear-induced compaction, Δn_s) (e.g. Figure 2.7b). The porosity loss only considering the change in vertical effective stress (Δn_{k_0}) is about 25%, the porosity loss by the change of non- K_0 mean effective stress (Δn_m) is about 65%, and

the porosity loss by the shear-induced compaction (Δn_s) is about 35%. (Figure 2.12c). What is perhaps most striking about these results is the very rapid loss in porosity across the transition zone as the stress conditions evolve from uniaxial burial to compressive failure. In partially drained systems, it is this area that will produce the greatest fluid sources that will contribute to the highest excess pressure. Saffer and Bekins (2002) used hydrologic modeling constrained by the observed porosity field to show that this was the region that expelled the greatest fluid volume.

Ultimately, the difference in the stress paths of material above and below the décollement results in a striking change in porosity across the décollement. This porosity difference increases from the outboard edge of the wedge to the interior of the wedge. Increasing the basal friction coefficient results in more compaction in the footwall and less porosity offset at the décollement. The observation of negative polarity are likely associated with the porosity contrast near décollement, and they have been found in many fields including Nankai, Costa Rica, Barbados, and Hikurangi (Bangs et al., 2004; Bangs et al., 1990; Park et al., 2010; Ranero et al., 2008; Tobin et al., 1994). Our study shows the porosity offset can exist in drained conditions, thus the observation of porosity offset may not be a sufficient condition to determine the existence of excess pressure.

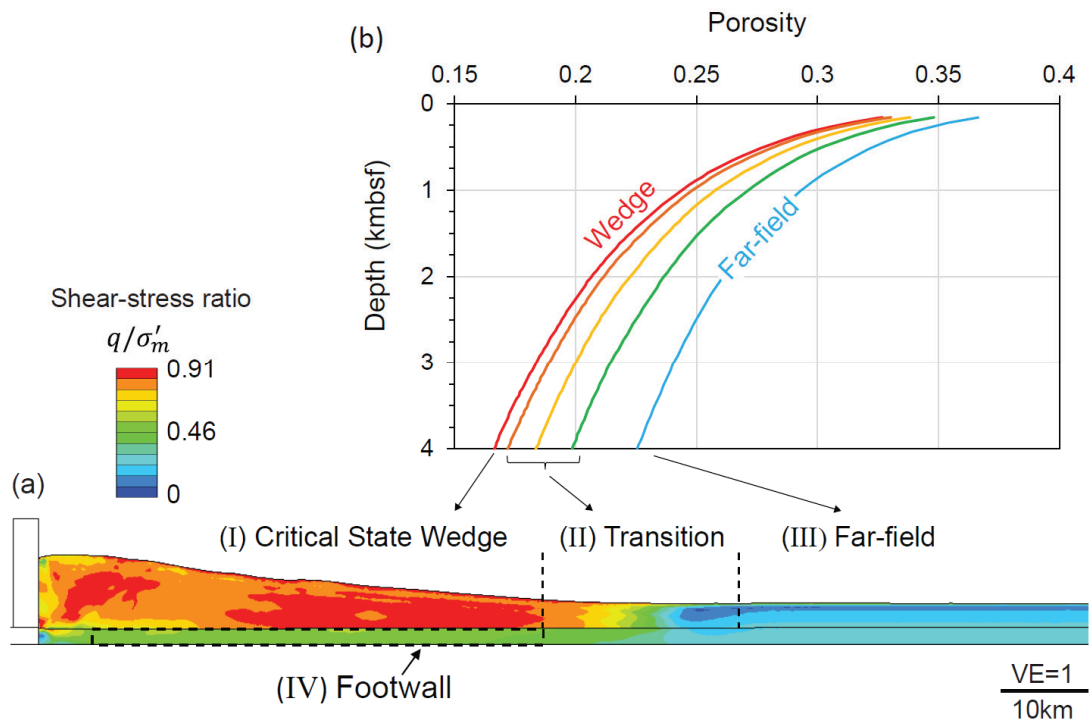


Figure 2.11: (a) Contours of shear-stress ratio and regions of distinct compaction behavior in a fold-and-thrust belt: (I) critical state wedge region, (II) transition region, (III) far-field geostatic region, and (IV) footwall region. (b) Estimated porosity vs. depths trends corresponding to different shear-stress ratios q/σ'_m and associated regions.

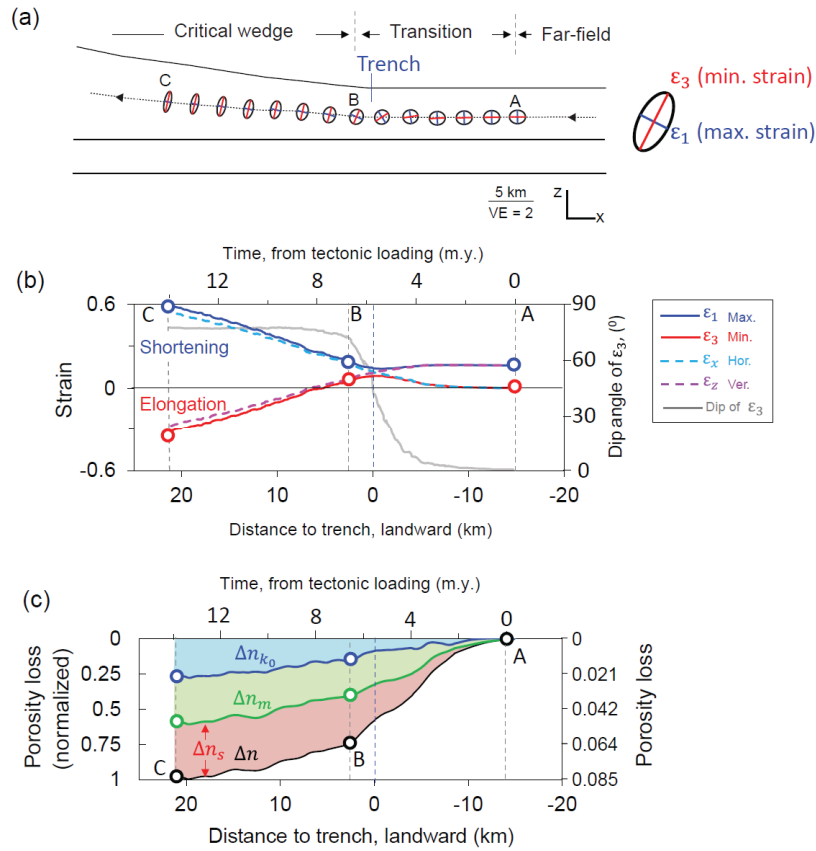


Figure 2.12: Evolution of strain and porosity for a sediment element that passes into the accretionary wedge. (a) Evolution of strain ellipse. Dark blue and red axes show the maximum and minimum strain orientations. Sediment starts to experience tectonic loading at Pt. A and reaches critical state at Pt. B. The region between Pt. A and Pt. B is Transition Zone. Seaward of Pt. A is the Far Field Zone and landward of Pt. B is the Critical Wedge Zone (Figure 11). (b) The evolution of principal strains (ϵ_1 and ϵ_3), horizontal strain (ϵ_x), and vertical strain (ϵ_z) with tectonic loading time and distance to trench. We denote shortening as positive and elongation as negative. The rotation of the principal strain orientation is shown with the gray line. Inside the wedge, the sediment experiences horizontal shortening strain (positive) and vertical elongation strain (negative). (c) Compaction due to change in vertical effective stress under uniaxial strain (Δn_{K_0}), loading by change in non- K_0 mean effective stress (Δn_m), and shear-induced compaction (Δn_s). The total compaction during tectonic loading is Δn .

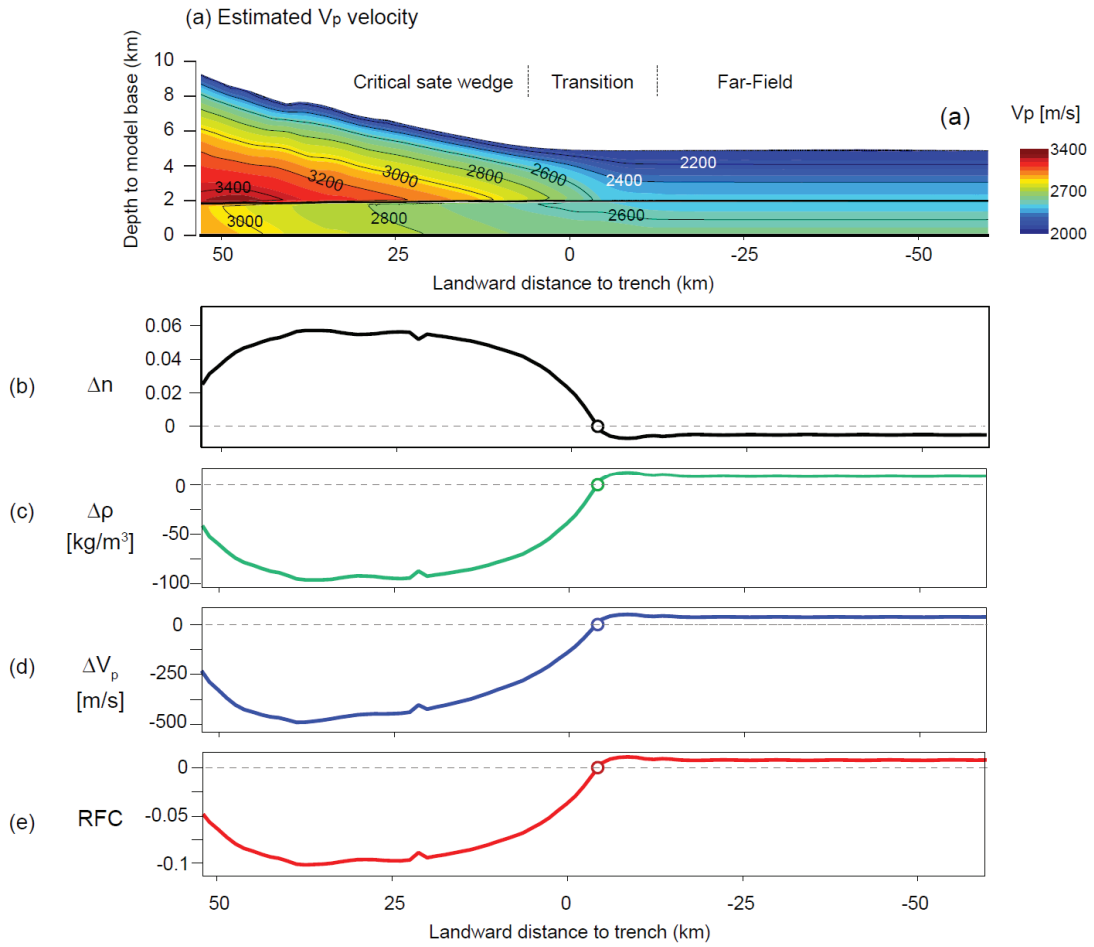


Figure 2.13: Seismic signature calculated from geomechanical modeling results. (a) V_p velocity pattern calculated from geomechanical-model porosity (Figure 6c), using Hoffman and Tobin (2004). (b) Porosity contrast just above (n_1) and below (n_2) the décollement ($\Delta n = n_2 - n_1$). (c) Density contrast just above (ρ_1) and below (ρ_2) the décollement ($\Delta \rho = \rho_2 - \rho_1$). (d) V_p velocity contrast ($\Delta V_p = V_2 - V_1$). (e) Reflection coefficient at décollement interface ($RFC = \frac{\rho_2 V_2 - \rho_1 V_1}{\rho_2 V_2 + \rho_1 V_1}$).

2.4.4 Implications for Field Observations

The models presented provide insight into the physical properties within fold-and-thrust belts. Sediment-matrix (intergranular) permeability distribution is a crucial component for studying flow behavior (Saffer and Bekins, 2002; Wang et al., 1990). Empirical models show that permeability declines logarithmically with porosity (Neuzil, 1994; Reece et al., 2012). Because our models show that, in drained conditions, porosity in the hanging wall is much lower than that in the footwall (Figure 2.6c, e), sediment-matrix permeability in the hanging wall is anticipated to be much lower than that in the footwall. Ultimately, models such as this may even be used to describe the permeability anisotropy because the evolution of strain can be tracked. This analysis considers only the permeability field resulting from compaction and does not explore the impacts of diagenesis or localized fracturing impacts.

Porosity is a primary factor controlling sediment elastic moduli and thus seismic velocities (Eberhart-Phillips et al., 1989; MacKay et al., 1995; Mavko et al., 1998). Therefore, P-wave velocity (V_p) can also be derived from porosity. We calculate a V_p distribution (Figure 2.13a) from the modeled porosity (Figure 2.6c), using the empirical porosity- V_p relationship of Hoffman and Tobin (2004). At equivalent depths below seafloor, the velocities are much higher within the wedge than in the far-field (Figure 2.13a). This reflects the higher porosity of the footwall sediments relative to the hanging wall sediments (Figure 2.6c).

We examine the contrast in velocity and density at the décollement to predict how the décollement will be seismically imaged (Figure 2.13c-e). The footwall has a lower seismic impedance ($\rho_2 V_2$) than the wedge ($\rho_1 V_1$), which results in a negative reflection coefficient (RFC, Figure 2.13e). The negative reflection coefficient will result in a negative

polarity reflection at the décollement as has been observed (Bangs et al., 2009; Moore, 1990; Park, 2002). The reflection amplitude increases dramatically landward for 25 km from the trench and thereafter declines (Figure 2.13e). This reflection response results from the compression behavior of the sediment (Figure 2.2b). Near the trench, the increase in both mean effective stress and deviatoric stress within the wedge results in a large porosity loss relative to the underlying strata. However, as the total stresses increase in the landward direction, the porosity is less sensitive to the difference in stress states above and below. This results in a near constant velocity offset at first and ultimately in a declining velocity and density offset in the landward direction (Figure 2.13c, d).

The elastic parameters including Young's modulus (E) and bulk modulus (K) can then be inverted from the estimated V_p distribution through rock physics relationships (Castagna et al., 1985; Dvorkin et al., 1999; Mavko et al., 1998). These physical properties are closely related to the storage of elastic potential energy and impacts fluid flow (Lotto and Dunham, 2015; Wang and Hu, 2006), thus can provide constrained information for studying earthquake rupture propagation. The geomechanics-constrained reference seismic velocity models may also contribute to build better velocity-depth conversion, leading to better prediction of locating seismicity events and structure images.

Our results may also provide guidance for identifying overpressured regions. By comparing field-porosity measurements (or seismic-derived porosity) with reference porosity–depth trends, areas with a high discrepancy in porosities may indicate the existence of excess pressure.

More broadly, our models provide insight into the relationship among pore pressure, porosity, and stress. Most previous attempts to estimate stress or pore pressure in fold-and-thrust belts were primarily focused on underthrust sediment, where the sediment

was assumed at uniaxial strain compaction (Saffer, 2003, 2007; Screaton et al., 2002). Recently, attempts have been made to include lateral stresses in the wedge and describe porosity as a function of mean effective stress (e.g., (Kitajima and Saffer, 2012; Moore and Tobin, 1997; Tsuji et al., 2014; Tsuji et al., 2008)). These recent approaches are beginning to illuminate the modeling of pressure and stresses; herein we further show that both mean and deviatoric stresses contribute significantly to compaction within the wedge.

2.4.5 Model Limitations

Any model has its limitations. First, we have considered only drained conditions and thus do not simulate excess pressure, which is clearly a direction for future work. Second, we do not consider the effect of strain weakening and consequent strain localization. Thus, the model does not consider the development of discrete faults within the wedge. Third, we are modeling a critically stressed wedge, in which the hanging-wall sediment is being accreted actively and is at shear failure condition. We are aware that, depending on the local tectonic history or dynamic events, the current stress state in the field of fold-and-thrust belts may not be all critical stressed. For example, Wang and Hu (2006) consider the impact of temporal stress change during earthquake cycles on deformation and stresses.

At a more fundamental level, the specific constitutive model has a direct impact on the predicted stress state and pore pressure. The SR3 model, as applied here, assumes yield surfaces that are symmetric about the isotropic stress axis. However, the yield surfaces are commonly found to be rotated about the loading path and are not necessarily symmetric about the isotropic stress axis (Wood, 1990). As material is driven from K_0 consolidation to failure, the evolution of these yield surfaces and the consequent compression remains a

key uncertainty. In the future, more-complicated models could incorporate the additional effects of this yield surface evolution (Whittle et al., 1994).

2.5 SUMMARY

We have simulated the evolution of marine accretionary prisms and their land counterpart fold-and-thrust belts using a large-strain, plane-strain geomechanical model under drained (hydrostatic) conditions. The simulated geometry correctly reproduces the predictions of critical-taper theory. Moreover, our approach enables us to illuminate the evolution of, and controls upon, porosity in these systems.

Sediment within fold-and-thrust belts has a much lower porosity than that in the underlying footwall because lateral loading increases mean effective and deviatoric stresses. Porosity contrast between the wedge and footwall sediments decreases as μ_b increases; a higher basal friction coefficient increases the footwall compaction but does not change the wedge compaction. In contrast, increasing the sediment internal friction coefficient increases compaction in the wedge but has little impact on the footwall. Our model records the development of a transition zone approximately 10–30 km wide, in which the stress ratios and compaction trends change rapidly between a uniaxial strain state and critical state. In this zone, the material undergoes the most dramatic change in stress state and associated compaction. The strain field shows the maximum shortening strain orientation rotates from vertical to sub-horizontal as the sediment is incorporated into the wedge.

These simulations provide new insight into fold-and-thrust-belt systems because they directly tie porosity to material properties, such as sediment strength and the décollement properties. Ultimately, we envision that these types of models can be used to

infer in situ pressure and stress from field observations. In turn, these approaches will assist in the design of stable and economic wells and may inform our understanding of earthquake processes in convergent margins.

2.6 ACKNOWLEDGMENTS

This work was funded by Statoil Fellowship and The University of Texas at Austin GeoFluids Consortium, which is supported by the following companies: Anadarko, BHP Billiton, BP, Chevron, Conoco-Phillips, ExxonMobil, Hess, PEMEX, Repsol, Shell, and Statoil. Publication authorized by the director of the Bureau of Economic Geology, Jackson School of Geosciences, The University of Texas at Austin. No new data were used in producing this manuscript.

2.7 APPENDIX A: GOVERNING EQUATIONS

Under plane strain and drained condition, the governing equilibrium equations are:

$$\frac{\partial \sigma'_x}{\partial x} + \frac{\partial \tau_{xz}}{\partial z} = 0 \quad (\text{A1})$$

$$\frac{\partial \tau_{xz}}{\partial x} + \frac{\partial \sigma'_z}{\partial z} = (\rho_b - \rho_w)g \quad (\text{A2})$$

where σ'_x and σ'_z are horizontal and vertical effective stresses, τ_{xz} is shear stress, ρ_w is water density, and ρ_b is bulk density. ρ_b is a function of porosity (n):

$$\rho_b = (1 - n)\rho_s + n\rho_w \quad (\text{A3})$$

where ρ_s and ρ_w are grain density and water density, respectfully. The values of applied ρ_s and ρ_w are shown in Table B1.

2.8 APPENDIX B: MATERIAL CONSTITUTIVE MODEL SR3

In our geomechanical analyses, we model sediments as elastoplastic material using the constitutive model SR3 (Crook et al. (2006); Rance et al. (2013)).

In our calibration of SR3, the elastic behavior depends on Young's modulus (E) and Poisson's ratio (ν). Poisson's ratio is assumed constant (Table 2.3). Young's modulus is a function of mean effective stress (σ'_m), porosity (n), and five input material constants (Table 2.3): E_{ref} , A , B , n_e , and c :

$$E = E_{ref} \left(\frac{\sigma'_m + A}{B} \right)^{n_e} n^c \quad (\text{B1})$$

Yield is described by a smooth three-invariant surface controlled by eight parameters:

$$\Phi(\sigma'_m, \varepsilon_v^p) = g(\theta_l, \sigma'_m)q + (\sigma'_m - \sigma_m^t) \tan \beta \left(\frac{\sigma'_m - \sigma_m^c}{\sigma_m^t - \sigma_m^c} \right)^{\frac{1}{n_{sr3}}} \quad (\text{B2})$$

where σ'_m is mean effective stress, q is deviatoric stress, ε_v^p is volumetric plastic strain, σ_m^c is preconsolidation stress (compressive intercept of yield surface with hydrostatic axis), σ_m^t is tensile intercept of yield surface with hydrostatic axis, β is friction parameter, θ_l is Lode angle, and n_{sr3} is material constant. Function $g(\theta_l, \sigma'_m)$ controls

the shape of the yield surface on the deviatoric plane. Input material constants are listed in Table 2.3. Hardening is defined by a relationship between volumetric plastic strain ε_v^p and the compressive and tensile intercepts σ_m^c and σ_m^t , respectively (Figure 2.14). The initial porosity–depth curve (Figure 2.15) is obtained from a uniaxial column test.

Table 2.3: SR3 material model parameters

Symbol	Parameter Name	Value
A	Material constant	-0.28
B	Material constant	-0.28
c	Material constant	-2
E_{ref}	Reference Young's modulus	40 MPa
$\sigma_m^{t_0}$	Initial tensile intercept	-0.085 MPa
$\sigma_m^{c_0}$	Initial compressive intercept	1 MPa
n_{sr3}	Material constant	1.3
n_e	Material constant	0.3
β	Friction parameter	60^0
ν	Poisson's ratio	0.25
ρ_s	Grain density	2.7 g/cm ³
ρ_w	Water density	1 g /cm ³

Table 2.4: Nomenclature

Symbol	Description	Dimensions
A	Material constant	Dimensionless
B	Material constant	Dimensionless
c	Material constant	Dimensionless
E	Young's modulus	M/LT ²
E _{ref}	Reference Young's modulus	M/LT ²
g	Yield surface shape factor	Dimensionless
K ₀	Geostatic stress ratio	Dimensionless
n	Porosity	Dimensionless
n _{sr3}	Material constant	Dimensionless
q	Deviatoric stress	M/LT ²
v	Poisson's ratio	Dimensionless
μ_w	Friction coefficient at wall contact	Dimensionless
μ_s	Sediment internal friction coefficient	Dimensionless
μ_b	Basal friction coefficient	Dimensionless
ϕ'_s	Sediment internal friction angle	Dimensionless
ϕ_b	Basal friction angle	Dimensionless
σ'_x	Horizontal effective stress	M/LT ²
σ'_z	Vertical effective stress	M/LT ²
σ'_1	Maximum principal effective stress	M/LT ²
σ'_2	Intermediate principal effective stress	M/LT ²
σ'_3	Minimum principal effective stress	M/LT ²
σ'_m	Mean effective stress	M/LT ²
σ_m^c	Compressive intercept	M/LT ²
σ_m^t	Tensile intercept	M/LT ²
$\sigma_m^{c_0}$	Initial compressive intercept	M/LT ²
$\sigma_m^{t_0}$	Initial tensile intercept	M/LT ²
τ_{xz}	Shear stress	M/LT ²
ϵ_1	Maximum principal strain	Dimensionless
ϵ_2	Minimum principal strain	Dimensionless
ϵ_x	Horizontal strain	Dimensionless
ϵ_z	Vertical strain	Dimensionless
α	Surface slope	Dimensionless
β	Friction parameter	Dimensionless
θ	Stress orientation angle	Dimensionless

Table 2.4 cont.

θ_1	Lode angle	Dimensionless
η	Shear stress ratio	Dimensionless
η^*	Slope of Mohr–Coulomb failure	Dimensionless
η_{K_0}	Slope of K_0 state line	Dimensionless
η_{cs}	Slope of critical state line	Dimensionless
ε_v^p	Plastic volumetric strain	Dimensionless

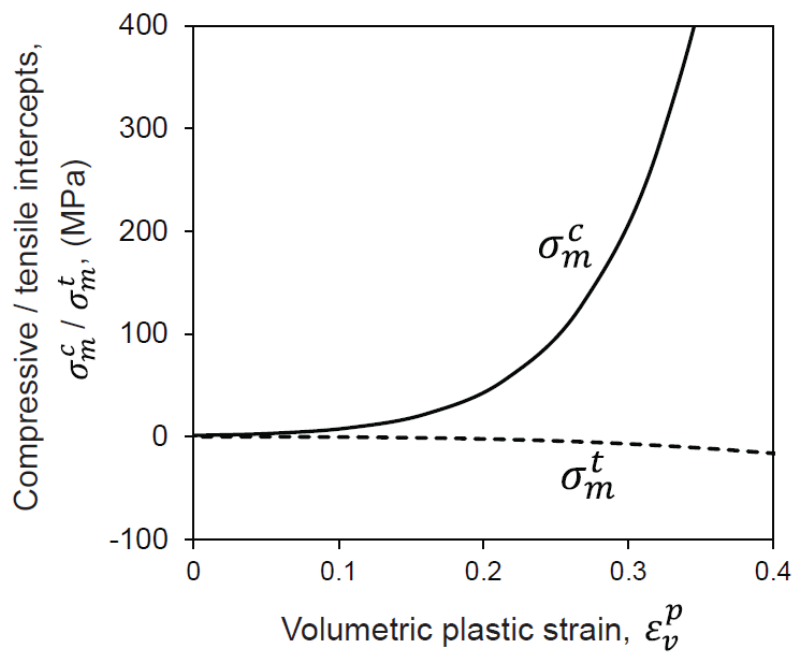


Figure 2.14: Input hardening: relationship among volumetric strain (ϵ_v^p), compressive intercept σ_m^c (solid line), and tensile intercept σ_m^t (dashed line).

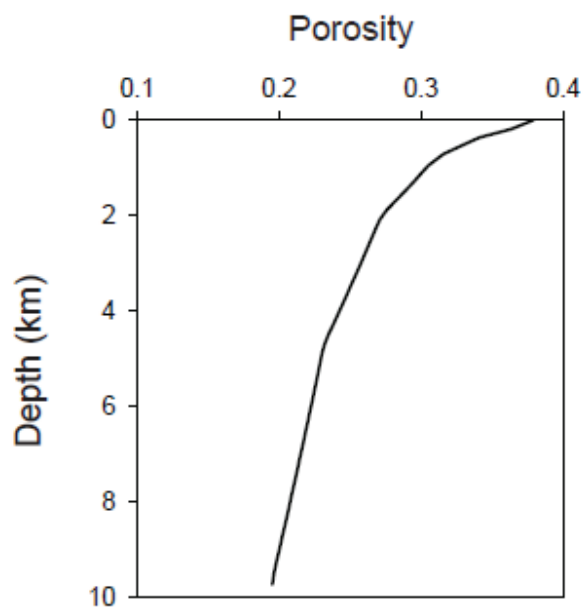


Figure 2.15: Initial porosity–depth relationship of modeled sediment.

REFERENCES

- Albertz, M., & Lingrey, S. (2012). Critical state finite element models of contractional fault-related folding: Part 1. Structural analysis. *Tectonophysics*, 576-577, 133–149. <https://doi.org/10.1016/j.tecto.2012.05.015>
- Ammon, C. J., Ji, C., Thio, H.-K., Robinson, D., Ni, S., Hjorleifsdottir, V., . . . Helmberger, D. (2005). Rupture process of the 2004 Sumatra-Andaman earthquake. *Science*, 308, 1133–1139.
- Bangs, N.L.B., Moore, G. F., Gulick, S.P.S., Pangborn, E. M., Tobin, H. J., Kuramoto, S., & Taira, A. (2009). Broad, weak regions of the Nankai Megathrust and implications for shallow coseismic slip. *Earth and Planetary Science Letters*, 284(1-2), 44–49. <https://doi.org/10.1016/j.epsl.2009.04.026>
- Bangs, N. L., Shipley, T. H., Gulick, S. P.S., Moore, G. F., Kuromoto, S., & Nakamura, Y. (2004). Evolution of the Nankai Trough décollement from the trench into the seismogenic zone: Inferences from three-dimensional seismic reflection imaging. *Geology*, 32(4), 273. <https://doi.org/10.1130/G20211.2>
- Bangs, N. L. B., Westbrook, G. K., Ladd, J. W., & Buhl, P. (1990). Seismic velocities from the Barbados Ridge complex: Indicators of high pore fluid pressures in an accretionary complex. *Journal of Geophysical Research: Solid Earth* (1978–2012), 95, 8767–8782.
- Bekins, B. A., & Dreiss, S. J. (1992). A simplified analysis of parameters controlling dewatering in accretionary prisms. *Earth and Planetary Science Letters*, 109(3-4), 275–287. [https://doi.org/10.1016/0012-821X\(92\)90092-A](https://doi.org/10.1016/0012-821X(92)90092-A)
- Brückmann, W., Moran, K., & Housen, B. A. (1997). Directional properties of p-wave velocities and acoustic anisotropies in different structural domains of the Northern Barbados Ridge accretionary complex. In (Vol. 156, pp. 115–123).
- Byrne, T., & Fisher, D. (1990). Evidence for a weak and overpressured decollement beneath sediment - dominated accretionary prisms. *Journal of Geophysical Research: Solid Earth* (1978 - 2012), 95, 9081 - 9097.
- Castagna, J. P., Batzle, M. L., & Eastwood, R. L. (1985). Relationships between compressional-wave and shear-wave velocities in clastic silicate rocks. *Geophysics*, 50, 571–581.

- Chapple, W. M. (1978). Mechanics of thin-skinned fold-and-thrust belts. *Geological Society of America Bulletin*, 89(8), 1189–1198. [https://doi.org/10.1130/0016-7606\(1978\)89<1189:MOTFB>2.0.CO;2](https://doi.org/10.1130/0016-7606(1978)89<1189:MOTFB>2.0.CO;2)
- Crook, A.J.L., Willson, S. M., Yu, J. G., & Owen, D.R.J. (2006). Predictive modelling of structure evolution in sandbox experiments. *Journal of Structural Geology*, 28(5), 729–744. <https://doi.org/10.1016/j.jsg.2006.02.002>
- Dahlen, F. (1990). Critical Taper Model Of Fold-And-Thrust Belts And Accretionary Wedges. *Annual Review of Earth and Planetary Sciences*, 18(1), 55–99. <https://doi.org/10.1146/annurev.earth.18.1.55>
- Dahlen, F. A., & Suppe, J. (1988). Mechanics, growth, and erosion of mountain belts. In *Geological Society of America Special Papers. Processes in Continental Lithospheric Deformation* (Vol. 218, pp. 161–178). Geological Society of America. <https://doi.org/10.1130/SPE218-p161>
- Davis, D., Suppe, J., & Dahlen, F. A. (1983). Mechanics of fold-and-thrust belts and accretionary wedges. *Journal of Geophysical Research*, 88(B2), 1153. <https://doi.org/10.1029/JB088iB02p01153>
- Dvorkin, J., Prasad, M., Sakai, A., & Lavoie, D. (1999). Elasticity of marine sediments: Rock physics modeling. *Geophysical Research Letters*, 26, 1781–1784.
- Eberhart-Phillips, D., Han, D.-H., & Zoback, M. D. (1989). Empirical relationships among seismic velocity, effective pressure, porosity, and clay content in sandstone. *Geophysics*, 54, 82–89.
- Flemings, P. B., & Saffer, D. M. (2018). Pressure and Stress Prediction in the Nankai Accretionary Prism: A Critical State Soil Mechanics Porosity-Based Approach. *Journal of Geophysical Research: Solid Earth*, 123(2), 1089–1115. <https://doi.org/10.1002/2017JB015025>
- Hafner, W. (1951). Stress distributions and faulting. *Geological Society of America Bulletin*, 62, 373–398.
- Hauser, M. R., Couzens-Schultz, B. A., & Chan, A. W. (2014). Estimating the influence of stress state on compaction behavior. *Geophysics*, 79(6), D389-D398. <https://doi.org/10.1190/geo2014-0089.1>
- Heidari, M., Nikolinakou, M. A., Hudec, M. R., & Flemings, P. B. (2016). Geomechanical analysis of a welding salt layer and its effects on adjacent

- sediments. *Tectonophysics*, 683, 172–181.
<https://doi.org/10.1016/j.tecto.2016.06.027>
- Henry, P., Jouniaux, L., Screatton, E. J., Hunze, S., & Saffer, D. M. (2003). Anisotropy of electrical conductivity record of initial strain at the toe of the Nankai accretionary wedge. *Journal of Geophysical Research: Solid Earth*, 108(B9), 640.
<https://doi.org/10.1029/2002JB002287>
- Hoffman, N. W., & Tobin, H. J. (2004). An Empirical Relationship between Velocity and Porosity for Underthrust Sediments in the Nankai Trough Accretionary Prism. *Proc. ODP, Sci. Results*, 190/196, 1–23.
<https://doi.org/10.2973/odp.proc.sr.190196.355.2004>
- Housen, B. A. (1997). Magnetic anisotropy of Barbados prism sediments. *Proceedings of the Ocean Drilling Program, Scientific Results*, 156, 97–105.
- Housen, B. A., Tobin, H. J., Labaume, P., Leitch, E. C., Maltman, A. J., & Party, O. D. P. L. 1. S. S. (1996). Strain decoupling across the decollement of the Barbados accretionary prism. *Geology*, 24(2), 127–130. [https://doi.org/10.1130/0091-7613\(1996\)024<0127:SDATDO>2.3.CO;2](https://doi.org/10.1130/0091-7613(1996)024<0127:SDATDO>2.3.CO;2)
- Hubbert, M. K., & Rubey, W. W. (1959). Mechanics of fluid-filled porous solids and its application to overthrust faulting. *Geological Society of America Bulletin*, 70, 115–166.
- Hyndman, R. D., Moore, G. F., & Moran, K. (1993). Velocity, porosity, and pore-fluid loss from the Nankai subduction zone accretionary prism. *Proceedings of the Ocean Drilling Program, Scientific Results*, 131, 211–220.
- Karig, D. E. (1986). Physical properties and mechanical state of accreted sediments in the Nankai Trough, Southwest Japan Arc. In J. C. Moore (Ed.), *Structural Fabrics in Deep Sea Drilling Project Cores From Forearcs* (pp. 117–133). Geological Society of America. Retrieved from <http://dx.doi.org/10.1130/MEM166-p117>
- Kitajima, H., Chester, F. M., & Biscontin, G. (2012). Mechanical and hydraulic properties of Nankai accretionary prism sediments: Effect of stress path. *Geochemistry, Geophysics, Geosystems*, 13, 1–24.
<https://doi.org/10.1029/2012GC004124>
- Kitajima, H., & Saffer, D. M. (2012). Elevated pore pressure and anomalously low stress in regions of low frequency earthquakes along the Nankai Trough subduction megathrust. *Geophysical Research Letters*, 39(23), n/a-n/a.
<https://doi.org/10.1029/2012GL053793>

- Lallemand, S. E., Schnürle, P., & Malavieille, J. (1994). Coulomb theory applied to accretionary and nonaccretionary wedges: Possible causes for tectonic erosion and/or frontal accretion. *Journal of Geophysical Research: Solid Earth* (1978–2012), 99, 12033–12055.
- Lotto, G. C., & Dunham, E. M. (2015). High-order finite difference modeling of tsunami generation in a compressible ocean from offshore earthquakes. *Computational Geosciences*, 19, 327.
- MacKay, M. E., Moore, G. F., Klaeschen, D., & Huene, R. von. (1995). The case against porosity change: Seismic velocity decrease at the toe of the Oregon accretionary prism. *Geology*, 23, 827–830.
- Mavko, G., Mukerji, T., & Dvorkin, J. (1998). *The Rock Physics Handbook: Tools for Seismic Analysis in Porous Media*, 329 pp: Cambridge Univ. Press, Cambridge, UK.
- Moore, J. C., & Tobin, H. (1997). Estimated fluid pressures of the Barbados accretionary prism and adjacent sediments. In (Vol. 156, pp. 229–238). *Ocean Drilling Program*.
- Morgan, J. K., Karig, D. E., & Maniatty, A. (1994). The estimation of diffuse strains in the toe of the western Nankai accretionary prism: A kinematic solution. *Journal of Geophysical Research: Solid Earth* (1978–2012), 99, 7019–7032.
- Morley, C. K., King, R., Hillis, R., Tingay, M., & Backe, G. (2011). Deepwater fold and thrust belt classification, tectonics, structure and hydrocarbon prospectivity: a review. *Earth-Science Reviews*, 104, 41–91.
- Nemcok, M., Schamel, S., & Gayer, R. (2009). *Thrustbelts: Structural architecture, thermal regimes and petroleum systems*: Cambridge University Press.
- Neuzil, C. E. (1994). How permeable are clays and shales? *Water Resources Research*, 30, 145–150.
- Nikolinakou, M. A., Hudec, M. R., & Flemings, P. B. (2014). Comparison of evolutionary and static modeling of stresses around a salt diapir. *Marine and Petroleum Geology*, 57, 537–545.
<https://doi.org/10.1016/j.marpetgeo.2014.07.002>
- Obradors-Prats, J., Rouainia, M., Aplin, A. C., & Crook, A. J. L. (2017). *Hydromechanical Modeling of Stress, Pore Pressure, and Porosity Evolution in*

- Fold-and-Thrust Belt Systems. *Journal of Geophysical Research: Solid Earth*, 122(11), 9383–9403. <https://doi.org/10.1002/2017JB014074>
- Obradors-Prats, J., Rouainia, M., Aplin, A. C., & Crook, Anthony J. L. (2016). Stress and pore pressure histories in complex tectonic settings predicted with coupled geomechanical-fluid flow models. *Marine and Petroleum Geology*, 76, 464–477. <https://doi.org/10.1016/j.marpetgeo.2016.03.031>
- Owens, W. H. (1993). Magnetic fabric studies of samples from Hole 808C, Nankai Trough. *Proceedings of Ocean Drilling Program, Scientific Results*, 13, 301–310.
- Park, J.-O., Fujie, G., Wijerathne, L., Hori, T., Kodaira, S., Fukao, Y., . . . Taira, A. (2010). A low-velocity zone with weak reflectivity along the Nankai subduction zone. *Geology*, 38, 283–286. <https://doi.org/10.1130/G30205.1>
- Park, J.-O., Tsuru, T., Kodaira, S., Cummins, P. R., & Kaneda, Y. (2002). Splay fault branching along the Nankai subduction zone. *Science*, 297(5584), 1157–1160.
- Perić, D., & Crook, A. J.L. (2004). Computational strategies for predictive geology with reference to salt tectonics. *Computer Methods in Applied Mechanics and Engineering*, 193(48-51), 5195–5222.
- Perić, D., Vaz Jr, M., & Owen, D. R.J. (1999). On adaptive strategies for large deformations of elasto-plastic solids at finite strains: computational issues and industrial applications. *Computer Methods in Applied Mechanics and Engineering*, 176(1-4), 279–312.
- Plafker, G. (1965). Tectonic deformation associated with the 1964 Alaska earthquake. *Science*, 148, 1675–1687.
- Platt, J. P. (1986). Dynamics of orogenic wedges and the uplift of high-pressure metamorphic rocks. *Geological Society of America Bulletin*, 97, 1037–1053.
- Rance, J. M., Profit, M. L., Dee, S. J., & Roberts, D. T. (2013). Predicting the Paleo Evolution of Overpressured Geological Structures. In *American Rock Mechanics Association*.
- Ranero, C. R., Grevemeyer, I., Sahling, H., Barckhausen, U., Hensen, C., Wallmann, K., . . . McIntosh, K. (2008). Hydrogeological system of erosional convergent margins and its influence on tectonics and interplate seismogenesis. *Geochemistry, Geophysics, Geosystems*, 9, 1–18. <https://doi.org/10.1029/2007GC001679>
- Rankine, W. M. (1857). On the stability of loose earth. *Philosophical Transactions of the Royal Society of London*, 147, 9–27.

- Reece, J. S., Flemings, P. B., Dugan, B., Long, H., & Germaine, J. T. (2012). Permeability - porosity relationships of shallow mudstones in the Ursa Basin, northern deepwater Gulf of Mexico. *Journal of Geophysical Research: Solid Earth* (1978 - 2012), 117, 1 - 13.
- Rockfield. (2017). *Elfen Explicit Manual (Version 4.10)*. Swansea, UK: Rockfield Software.
- Roscoe, K. H., & Burland, J. B. (1968). On the generalized stress-strain behaviour of wet clay: Cambridge.
- Rowe, K. T., Screaton, E. J., & Ge, S. (2012). Coupled fluid flow and deformation modeling of the frontal thrust region of the Kumano Basin transect, Japan: Implications for fluid pressures and decollement downstepping. *Geochemistry, Geophysics, Geosystems*, 13(3), n/a-n/a. <https://doi.org/10.1029/2011GC003861>
- Saffer, D. M. (2003). Pore pressure development and progressive dewatering in underthrust sediments at the Costa Rican subduction margin: Comparison with northern Barbados and Nankai. *Journal of Geophysical Research: Solid Earth*, 108(B5), 939. <https://doi.org/10.1029/2002JB001787>
- Saffer, D. M. (2007). Pore pressure within underthrust sediment in subduction zones. *The Seismogenic Zone of Subduction Thrust Faults*, 171–209.
- Saffer, D. M., & Bekins, B. A. (2002). Hydrologic controls on the morphology and mechanics of accretionary wedges. *Geology*, 30(3), 271. [https://doi.org/10.1130/0091-7613\(2002\)030<0271:HCOTMA>2.0.CO;2](https://doi.org/10.1130/0091-7613(2002)030<0271:HCOTMA>2.0.CO;2)
- Saffer, D. M., & Tobin, H. J. (2011). Hydrogeology and Mechanics of Subduction Zone Forearcs: Fluid Flow and Pore Pressure. *Annual Review of Earth and Planetary Sciences*, 39(1), 157–186. <https://doi.org/10.1146/annurev-earth-040610-133408>
- Schott, B., & Koyi, H. A. (2001). Estimating basal friction in accretionary wedges from the geometry and spacing of frontal faults. *Earth and Planetary Science Letters*, 194, 221–227.
- Screaton, E., Saffer, D., Henry, P., & Hunze, S. (2002). Porosity loss within the underthrust sediments of the Nankai accretionary complex: Implications for overpressures. *Geology*, 30(1), 19. [https://doi.org/10.1130/0091-7613\(2002\)030<0019:PLWTUS>2.0.CO;2](https://doi.org/10.1130/0091-7613(2002)030<0019:PLWTUS>2.0.CO;2)

- Simons, M., Minson, S. E., Sladen, A., Ortega, F., Jiang, J., Owen, S. E., . . . Chu, R. (2011). The 2011 magnitude 9.0 Tohoku-Oki earthquake: Mosaicking the megathrust from seconds to centuries. *Science*, 332, 1421–1425.
- Stauffer, P., & Bekins, B. A. (2001). Modeling consolidation and dewatering near the toe of the northern Barbados accretionary complex. *Journal of Geophysical Research: Solid Earth* (1978–2012), 106, 6369–6383. <https://doi.org/10.1029/2000JB900368>
- Thornton, D. A., & Crook, A. J. L. (2014). Predictive Modeling of the Evolution of Fault Structure: 3-D Modeling and Coupled Geomechanical/Flow Simulation. *Rock Mechanics and Rock Engineering*, 47(5), 1533–1549. <https://doi.org/10.1007/s00603-014-0589-6>
- Tobin, H. J., Moore, J. C., & Moore, G. F. (1994). Fluid pressure in the frontal thrust of the Oregon accretionary prism: Experimental constraints. *Geology*, 22, 979–982.
- Tsuji, T., Kamei, R., & Pratt, R. G. (2014). Pore pressure distribution of a mega-splay fault system in the Nankai Trough subduction zone: Insight into up-dip extent of the seismogenic zone. *Earth and Planetary Science Letters*, 396, 165–178. <https://doi.org/10.1016/j.epsl.2014.04.011>
- Tsuji, T., Tokuyama, H., Costa Pisani, P., & Moore, G. (2008). Effective stress and pore pressure in the Nankai accretionary prism off the Muroto Peninsula, southwestern Japan. *Journal of Geophysical Research: Solid Earth* (1978–2012), 113, 1–19. <https://doi.org/10.1029/2007JB005002>
- Wang, C. - Y., Shi, Y., Hwang, W. - T., & Chen, H. (1990). Hydrogeologic processes in the Oregon - Washington Accretionary Complex. *Journal of Geophysical Research: Solid Earth* (1978 - 2012), 95, 9009 - 9023.
- Wang, H. F. (2017). *Theory of linear poroelasticity with applications to geomechanics and hydrogeology*: Princeton University Press.
- Wang, K., & He, J. (1999). Mechanics of low - stress forearcs: Nankai and Cascadia. *Journal of Geophysical Research: Solid Earth* (1978 - 2012), 104, 15191 - 15205.
- Wang, K., & Hu, Y. (2006). Accretionary prisms in subduction earthquake cycles: The theory of dynamic Coulomb wedge. *Journal of Geophysical Research: Solid Earth* (1978–2012), 111.
- Whittle, A. J., DeGroot, D. J., Ladd, C. C., & Seah, T.-H. (1994). Model prediction of anisotropic behavior of Boston Blue Clay. *Journal of Geotechnical Engineering*, 120(1), 199–224.

Wood, D. M. (1990). Soil behaviour and critical state soil mechanics: Cambridge University Press.

Zoback, M. D. (2010). Reservoir geomechanics: Cambridge University Press., 340-369.

Chapter 3: Overpressure generation and its impact on stress and porosity in accretionary wedge system

ABSTRACT

I use forward transient geomechanical modeling to study the coupled mechanical and fluid-flow behavior in an evolving accretionary wedge. I investigate the evolution of overpressure, stress, strength, porosity and the interrelationship between them. There is a characteristic overpressure distribution in an overpressured accretionary wedge. Near the trench, the hanging-wall overpressure is higher than the footwall overpressure, which results in downward flow. This high hanging-wall overpressure results from a rapid increase in total mean stress and shear stress, and a decrease in permeability. The high hanging-wall overpressure also results in a decrease in mean effective stress and unloading in the footwall near trench. Toward the inner wedge, the footwall overpressure becomes higher than the hanging-wall overpressure. This high footwall overpressure is caused by an increase of overburden load, an increase of drainage length, the low-permeability of the overlying hanging-wall, and a higher compressibility in the footwall sediments relative to the hanging-wall sediments. Compared to the drained case, high overpressure in both the hanging-wall and footwall results in less increase of both mean effective stress and deviatoric stress and thus less compression compared to the fully drained condition. Consequently, the porosity offset at the décollement is less pronounced than under drained conditions. In both drained and overpressured accretionary wedges, the hanging-wall sediments are at critical state. With high overpressures, the footwall sediment is closer to a uniaxial-strain (K_0) compression state when compared to drained condition because there is less shear stress transmitted into the footwall. Low permeability and high convergence rate promote overpressure generation in the accretionary wedge. Decreasing the rock

permeability or increasing the plate convergence rate lowers the mean effective stress and deviatoric stress, and reduce the porosity offset across the decollement. Overall, our model results provide physical insights on the mechanical behavior and hydraulic processes in accretionary wedges, fold-and-thrust belts, and subduction zones.

3.1 INTRODUCTION

Elevated pore fluid pressures are commonly found in subduction zones. The sources of high pore pressure include tectonic loading, mineral dehydration, and thermal pressurization (Moore & Vrolijk, 1992; Saffer & Wallace, 2015). In shallow accretionary wedges (depth <10km), rapid tectonic loading on unconsolidated sediment is considered as the most important factor that contributes to the overpressure generation (Saffer & Tobin, 2011; Kitajima & Saffer, 2012). High pore pressure in subduction zones is a key factor that impacts fault strength (Hubbert & Rubey, 1959; Zoback, 2010), fault slip tendency (Scholz, 2002; Sawai *et al.*, 2016; Hardebeck & Loveless, 2018), earthquake events (Beeler *et al.*, 2000; Dixon & Moore, 2007), and accretionary wedge geometry (Davis *et al.*, 1983; Dahlen, 1990). High pore pressure has been widely invoked to explain various geological and geophysical observations in the outer accretionary wedges, such as high-porosity and low-velocity sediments at the frontal accretionary wedge (Screaton *et al.*, 2002; Bangs *et al.*, 2009), long-distance tsunami-genic earthquake ruptures (Kimura *et al.*, 2012; Romano *et al.*, 2014; Hirono *et al.*, 2016), slow earthquakes and slips (Peng & Gombert, 2010; Obara & Kato, 2016; Tonegawa *et al.*, 2017)), mud volcanoes (Dimitrov, 2002), and temperature & geochemical anomalies (Moore & Vrolijk, 1992). Understanding the stress and pressure in compressional tectonic environments is also important for energy exploration (Couzens-Schultz & Azbel, 2014; Hauser *et al.*, 2014) and greenhouse gas storage (Kim & Hosseini, 2014).

Because direct field measurements of pore pressure and stress are scarce and challenging to obtain (e.g. Becker *et al.* (1997)), several approaches have been developed to investigate the mechanical porous-flow conditions in accretionary wedges. An inverse approach is to predict pore pressure and stress from the physical properties of recovered

cores (Screaton *et al.*, 2002), remote sensing data (e.g. seismic velocity (Tsuji *et al.*, 2008; Tsuji *et al.*, 2014), or acoustic log data (Kitajima *et al.*, 2017). This approach directly ties the predicted results to the available field data, but it introduces simplified assumptions for stress orientation and horizontal-to-vertical effective stress ratio, which are poorly constrained in tectonic active regions. Another approach applies classic critical taper theory to estimate pore pressure based on sediment internal strength, basal friction, and the wedge taper angle (Davis *et al.*, 1983; Dahlen *et al.*, 1984). However, critical taper theory assumes constant pore pressure ratio and constant sediment density, thus it cannot predict the spatial variation of pore pressure. A third approach is to simulate the steady state fluid pressure with steady flow model on a fixed cross section (e.g. (Saffer & Bekins, 2002; Saffer & Bekins, 2006)). This approach is able to approximate the pore pressure variation based on the present day geometry, but it does not incorporate the change of pressure or permeability through time (Saffer and Bekins, 2006).

Traditionally, sediment is assumed to compress under uniaxial strain conditions (e.g Hart et al (1995); Gordon & Flemings (2002)). Under uniaxial-strain conditions, the deformation only occurs vertically and the maximum and minimum principal stresses remain vertical and horizontal. The horizontal effective stress (σ'_h) is proportional to the vertical effective stress (σ'_v) with constant ratio of K_0 ($\sigma'_v = K_0 \sigma'_h$). Therefore, under uniaxial strain conditions, mean effective stress, shear stress, and porosity only depend on the vertical effective stress. However, these assumptions and interrelationships are not valid in the non-uniaxial strain geologic environments such as fold-and-thrust belts and salt systems (Heidari *et al.*, 2018; Nikolinakou *et al.*, 2018). Particularly, as a sediment particle is consumed into a fold-and-thrust belt, the horizontal effective stress increases independently from the vertical effective stress. The maximum principal stress orientation

also rotates from vertical (away from the wedge) to sub-horizontal (inside the wedge) (Chapter 2). As a result, the change of mean effective stress and shear stress no longer depends exclusively on the vertical effective stress. Therefore, in fold-and-thrust belts, the full stress tensor (including both mean effective- and shear stress) should be taken into account when studying sediment compression and pore pressure generation (e.g. Heidari et al (2018)).

Critical state soil mechanics provides a methodology to couple stress, strain, porosity, and pore pressure in non-uniaxial strain environments. Critical state soil mechanics is able to account for both mean-effective-stress and shear-stress induced compression (Roscoe *et al.*, 1958; Wood, 1990). Thus, in accretionary wedges, where the shear stress is high, applying critical state soil mechanics can provide more accurate stress and porosity prediction. Coupling pore volume changes to stress changes is also important for fluid flow analysis because it is directly related to the strain and permeability and thus impacts pore pressure generation (Schofield & Wroth, 1968; Neuzil, 1995).

Critical state formulations have been employed to study stress and pressure in fold-and-thrust belts. Rowe et al. (2012) simulate the stress and fluid flow near a frontal thrust in Nankai accretionary wedge. Obrador-Prats et al. (2017) predict the stress and pore pressure in NW Borneo fold-and-thrust belt. Both studies however prescribe the initial wedge geometries and the displacements along the décollement are limited to only a few thousand meters. Recently, critical state soil mechanics has also been applied to predict field stress and pore pressure by using porosity data from recovered cores in Nankai accretionary wedge (Flemings & Saffer, 2018).

Despite the progress, to my knowledge, no existing study reveals how the stress, porosity, and pore pressure evolve incrementally from the onset of tectonic loading to the

state of critically-stressed wedge. Here, I use large-strain evolutionary transient geomechanical models to investigate the mechanical and porous fluid flow processes in accretionary wedge systems. I simulate sediments as poro-elastoplastic material, using critical state soil mechanics. I am able to track the coupled evolution of stresses, pressure, and compression as the sediment is incorporated into the hanging-wall and into the footwall. I also quantitatively investigate how convergence rate and permeability control the distribution of stress and pore pressures in accretionary wedges.

3.2 MODEL DESCRIPTION

I have built a large-strain, plane-strain, forward geomechanical models with Elfen (Rockfield, 2017) to simulate the development of accretionary wedges. The model is based on quasi-static, finite-element method with automated adaptive remeshing techniques (Crook *et al.*, 2006). Lagrangian and Eulerian reference frames are used for the mechanical and fluid phases, respectively. Pore pressure is calculated in the seepage field, where fluid flow is determined relative to the deformation of the mesh defined in the mechanical field (Crook *et al.*, 2006). Pore pressure is then transferred to the mechanical field using the volumetric strain. The frequency of this coupling process is determined so that the difference between seepage and mechanical pore pressure remains minimal (Rockfield, 2017). More details about the material properties, governing equations, and basic discretization steps are listed in Appendix A and B.

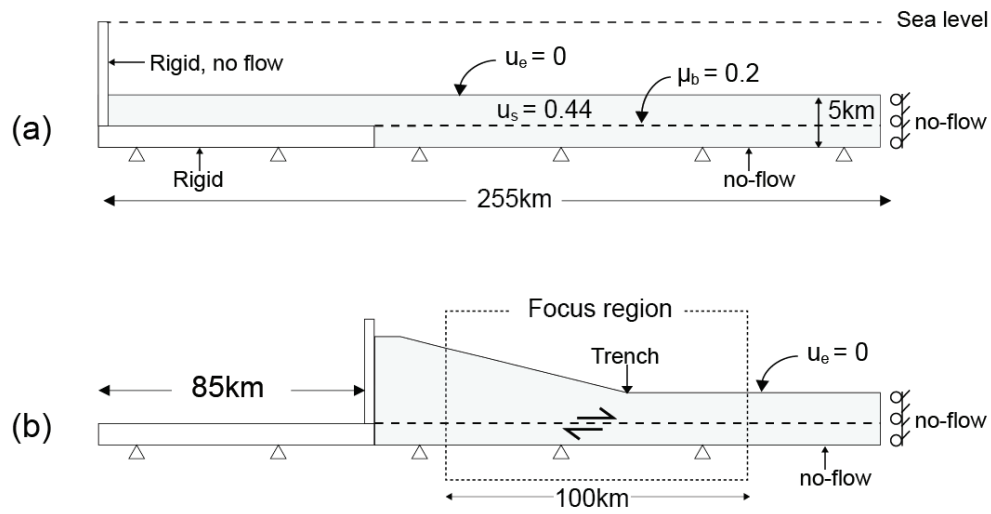


Figure 3.1: Model set-up and boundary conditions. (a) Initial geometry. The horizontal domain is 255km wide. The upper and lower sediment are 3km and 2km thick, respectively. The friction coefficient at the contact between the upper and lower layer is $\mu_b = 0.2$ (equivalent to internal friction angle of $\phi'_s = 11^\circ$). The sediment internal strength is $\mu_s = 0.44$ ($\phi'_s = 24^\circ$). The top of the model is a free-draining surface with hydrostatic pressure. The bottom is a fixed, no-flow boundary. The right boundary is fixed in horizontal direction and is also a no-flow boundary. Sea-level is kept at 12km from the base of the model throughout the simulation. (b) Final geometry at the end of the simulation. The vertical wall is displaced 85km to the right. The “Focus region” indicates the area near trench where results are subsequently plotted.

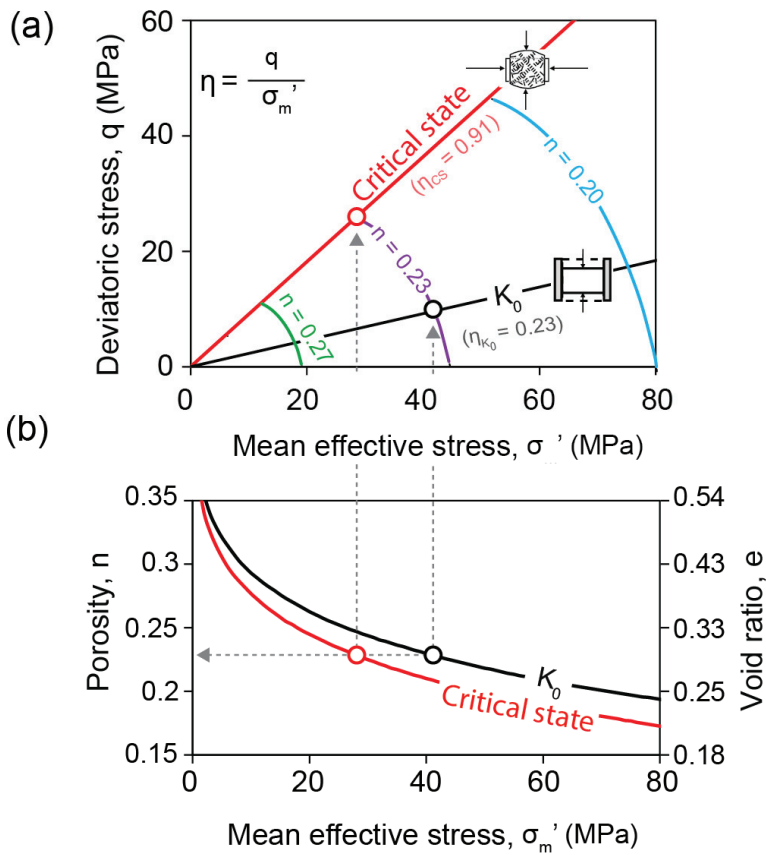


Figure 3.2: Basic principles of critical state model SR3: (a) Mean effective stress (σ'_m) versus deviatoric stress (q) plot. The red line represents critical state line for internal friction angle of 23.5° . The black line represents the uniaxial strain (K_0) compression path with $K_0 = 0.8$. The arcs are iso-porosity curves. The red dot represents a sediment element at critical state and the black dot represent another sediment element at K_0 stress path. (b) Compression curves along critical state path (red line) and uniaxial path (black line). The red and black dots show that the two sediment elements has the same porosity that results from different stress states in (a).

3.2.1 Boundary and initial conditions

We initialize the model with two horizontal layers that represent the sediment above and below the décollement (Figure 3.1a). The thickness of the upper and lower layers are 3km and 2km, respectively. The width of the domain is 255km. Displacement is constrained in both horizontal and vertical directions at the base of the model, and in the horizontal direction at the right boundary (Figure 3.1). The décollement is simulated by a frictional contact between the upper and lower layer with a constant friction coefficient (μ_b) of 0.2. The frictional coefficient of the contact between the left rigid wall and the upper sediment layer is constant and equals the sediment internal strength ($\mu_s = 0.44$). There is no cohesion at the contact boundaries. The left, right, and bottom of the domain are no-flow boundaries. The seafloor is a free-flow boundary and remains at hydrostatic pressure ($u_e = 0$). Fluid is allowed to flow freely across the décollement. The initial sediment pore pressure is hydrostatic, with the sea surface located at 12km above the base of the model (Figure 3.1a). Tectonic movement is simulated by displacing the left rigid wall towards the right at a steady rate, to a final displacement of 85km (Figure 3.1b, base case: 5mm/yr displacement rate [Model 1, Table 3.1]).

3.2.2 Material properties

I use the SR3 material model to describe the stress-strain behavior of the sediment. SR3 is an elastoplastic material model based on critical state soil mechanics (e.g., (Wood, 1990)). The SR3 model links porosity change to both mean-effective stress (σ'_m) and deviatoric stresses (q):

$$\sigma'_m = \frac{\sigma'_1 + \sigma'_2 + \sigma'_3}{3}, \quad (1)$$

$$q = \sqrt{\frac{(\sigma_1 - \sigma_2)^2 + (\sigma_2 - \sigma_3)^2 + (\sigma_3 - \sigma_1)^2}{2}}, \quad (2)$$

where σ'_1 , σ'_2 , and σ'_3 are maximum, intermediate, and minimum principal effective stresses, respectively.

We define the ratio of deviatoric stress to mean effective stress as shear-stress ratio (η):

$$\eta = \frac{q}{\sigma'_m} \quad (3)$$

The shear-stress ratio (η) is bounded by the critical state line (η_{cs}), which gives the maximum deviatoric stress that the sediment can withstand under a given mean effective stress (red line, Figure 3.2a). In this study, the slope of the critical state line (η_{cs}) is 0.91 (Table 3.3 contains the input parameters for SR3 model). Note that under conventional triaxial compression states ($\sigma'_1 > \sigma'_2 = \sigma'_3$), and for a cohesionless material, the critical state line coincides with the Mohr-Coulomb failure line in the $\sigma'_m - q$ space (Wood, 1990). Under plane strain conditions, and in the average stress ($\frac{\sigma'_1 + \sigma'_3}{2}$) and maximum shear stress ($\frac{\sigma'_1 - \sigma'_3}{2}$) space, critical state line is expected to lie higher than the Mohr-Coulomb shear failure line (Roscoe *et al.*, 1958).

The shear strength of the SR3 model can be expressed as an equivalent internal friction angle (ϕ'_s) (Gao *et al.*, 2018). In our base case (Model 1), the equivalent internal friction angle is 23.5° and the corresponding internal friction coefficient (μ_s) is:

$$\mu_s = \tan(\phi'_s) = 0.44 \quad (4)$$

This internal friction coefficient (μ_s) is within the range of values estimated from measurements and analytical calculations for the Nankai accretionary wedges (Lallemand *et al.*, 1994; Nemcok *et al.*, 2009).

We initialize the model assuming uniaxial strain (K_0) condition. The maximum and minimum principal stress directions are vertical and horizontal, respectively. The

horizontal-to-vertical effective stress ratio is 0.8 ($K_0 = 0.8$). Substituting $\sigma'_2 = \sigma'_3 = K_0\sigma'_1$ to Equations 1 and 2, the corresponding shear-stress ratio ($\eta = q/\sigma'_m$) for uniaxial (K_0) conditions is $\eta_{K_0} = 0.23$ (black line, Figure 3.2a). The initial porosity-depth relationship is shown in Appendix A (Figure 3.13a).

The interrelationship between mean effective stress (σ'_m), deviatoric stress (q), and porosity (n) is captured in $\sigma'_m - q$ space (Figure 3.2a) and $\sigma'_m - n$ space (Figure 2b). Under uniaxial strain conditions, the sediment follows the K_0 stress path in $\sigma'_m - q$ space. In this study, the slope of this line is $\eta_{K_0} = 0.23$ (black, Figure 3.2a). Under uniaxial-strain K_0 conditions, the porosity decreases along the K_0 compression line in the $\sigma'_m - n$ space (Black, Figure 3.2b). When sediment reaches shear failure, σ'_m and q lie on critical state line and the shear-stress ratio equals 0.91 ($\phi'_s = 23.5^\circ$) (red, Figure 3.2a). The relationship between mean effective stress and porosity depends on the shear-stress ratio. In $\sigma'_m - n$ space, uniaxial strain (K_0), the compression curve lies above the critical state compression curve (black versus red, Figure 3.2b). At the same magnitude of mean effective stress, sediment with higher shear-stress ratio has lower porosity (more porosity loss) than sediment with lower shear-stress ratio. The iso-porosity curves show all the possible pairs of mean effective stress and deviatoric stress that result in the same porosity (green, purple, and cyan arcs, Figure 3.2a). Consider two sediment elements with the same porosity value ($n = 0.23$, Figure 3.2a, b), that lie on different stress paths: one is on uniaxial-strain K_0 stress path (black circle, Figure 3.2a) and another is on critical state stress path (red circle, Figure 3.2a). The sediment on critical state line has a lower mean effective stress compared to that on the K_0 stress path ($\sim 30\text{MPa}$ vs. $\sim 40\text{MPa}$, Figure 3.2a). The iso-porosity curves bend to the left showing the dependency of sediment compression on the variation of deviatoric stress.

The sediment permeability is assumed to be isotropic and to vary with porosity (Appendix A, Figure 3.13b). Since porosity depends on both mean effective and deviatoric stress, permeability variation also depends on the full stress tensor. Permeability varies between 10^{-18} to 10^{-21}m^2 as porosity decreases from 0.5 to 0.15 (solid line, “med. k”, Figure 3.13b). This range of permeability values is comparable to permeability measurements on typical mudrocks in Gulf of Mexico (Yang & Aplin, 2010) and Nankai (Reece *et al.*, 2013) (Figure 3.13b). Given the assumed compression and permeability profiles, the coefficient of consolidation varies between 10^{-6} and $10^{-8}\text{m}^2/\text{s}$ (Figure 3.13d ($C_v = k/(m_v * \mu)$) as the porosity decrease 0.35 to 0.15. This range for the coefficient of consolidation matches experimental results for Gulf of Mexico mudrocks (Casey *et al.*, 2015).

3.3 MODEL RESULTS

A self-similar wedge with consistent surface slope angle is formed with continuous horizontal loading. I specify the zero reference location for horizontal distances to be the tip of the accretionary wedge toe where the surface slope angle begins to have a pronounced increase (“trench”, Figure 3.1b). At the final stage after 85 km of displacement, the surface angle is 3.8° (Model 1, Table 3.1).

Table 3.1 List of models and summary of key results.

Model No.	#0	#1	#2	#3	#4	#5
permeability	Drained**	Med.*	Low*	High*	Med.*	Med.*
convergence rate (mm./yr.)	-	5	5	5	10	1
λ^* decoll..	0	0.43	0.53	0.22	0.47	0.29
porosity offset decoll. (%)	6	3	1	4	2	4
surface slope	5	3.8	4	4.1	3.7	4.1
σ'_1 dip hanging wall	7.4	8	6.3	7.4	8.5	7.8
σ'_x/σ'_y hanging wall	2.4	2.5	2.7	2.4	2.5	2.4
σ'_1/σ'_3 hanging wall	2.5	2.6	2.8	2.5	2.6	2.5
q/σ'_m hanging wall	0.85	0.86	0.91	0.84	0.86	0.83
σ'_1 dip footwall	62	55	58	58	54.5	55.2
σ'_x/σ'_y footwall	0.76	0.9	0.91	0.83	0.89	0.87
σ'_1/σ'_3 footwall	1.6	1.4	1.4	1.6	1.6	1.5
q/σ'_m footwall	0.48	0.35	0.33	0.46	0.36	0.42

The selected properties for comparison are overpressure ratio (λ^*) (Eq. 6) at décollement, porosity offset at décollement, wedge surface slope angle, dip angle of maximum principal effective stress (σ'_1), horizontal-to-vertical effective stress ratio (σ'_x/σ'_y), maximum to minimum principal stress ratio (σ'_1/σ'_3), shear stress ratio (q/σ'_m). For consistent comparison, λ^* , stress ratios and stress orientations are estimated by taking the average value of the hanging wall 4km sediment, and by taking the average value of the footwall 2km sediment (profiles A_{low} , A_{med} , A_{high} , A_{fast} , A_{slow} Figure 7, 9).

*The applied porosity and permeability relationships of the low-, medium-, and high-permeability models are shown in Figure A1 (Appendix A).

**The drained model results are from Gao et al., (2018).

3.3.1 Overpressure distribution

Overpressure (u_e) represents the difference between pore fluid pressure (u) and hydrostatic pore pressure (u_h):

$$u_e = u - u_h \quad (5)$$

The lateral displacement load generates overpressure (u_e) in both hanging-wall and footwall sediments. On the far right (-40 to -10km, Figure 3.3a), there is no overpressure because the sediment has not been subjected to tectonic loading yet. Toward the frontal part of the wedge, lateral tectonic loading cause rapid increase of overpressure in the hanging-wall. Because there is almost no overburden stress change near the trench (almost no hanging-wall thickening) and no direct lateral loading, the footwall overpressure does not increase as fast as the hanging-wall one. Because the hanging-wall overpressure is greater than the footwall overpressure near trench, there is a downward flow cross the décollement. We describe overpressure using the overpressure ratio λ^* (Figure 3.3b), which records how close the pore pressure is to the overburden stress (σ_v), relative to the hydrostatic profile:

$$\lambda^* = \frac{u - u_h}{\sigma_v - u_h} \quad (6)$$

$\lambda^* = 0$ and $\lambda^* = 1$ means the pore pressure equals to the hydrostatic pressure and overburden stress, respectively. An increase of λ^* means a larger fraction of the increase of overburden stress is taken by the increase of pore fluid pressure.

Inside the hanging-wall along profile A (Figure 3.3a), overpressure increases with depth and λ^* reaches the maximum value of 0.6 at about 9km depth (Figure 3.3b, d). Footwall overpressure is almost constant and the λ^* decreases from about 0.5 to 0.3 from the décollement to the base of the model (Figure 3.3d) along profile A.

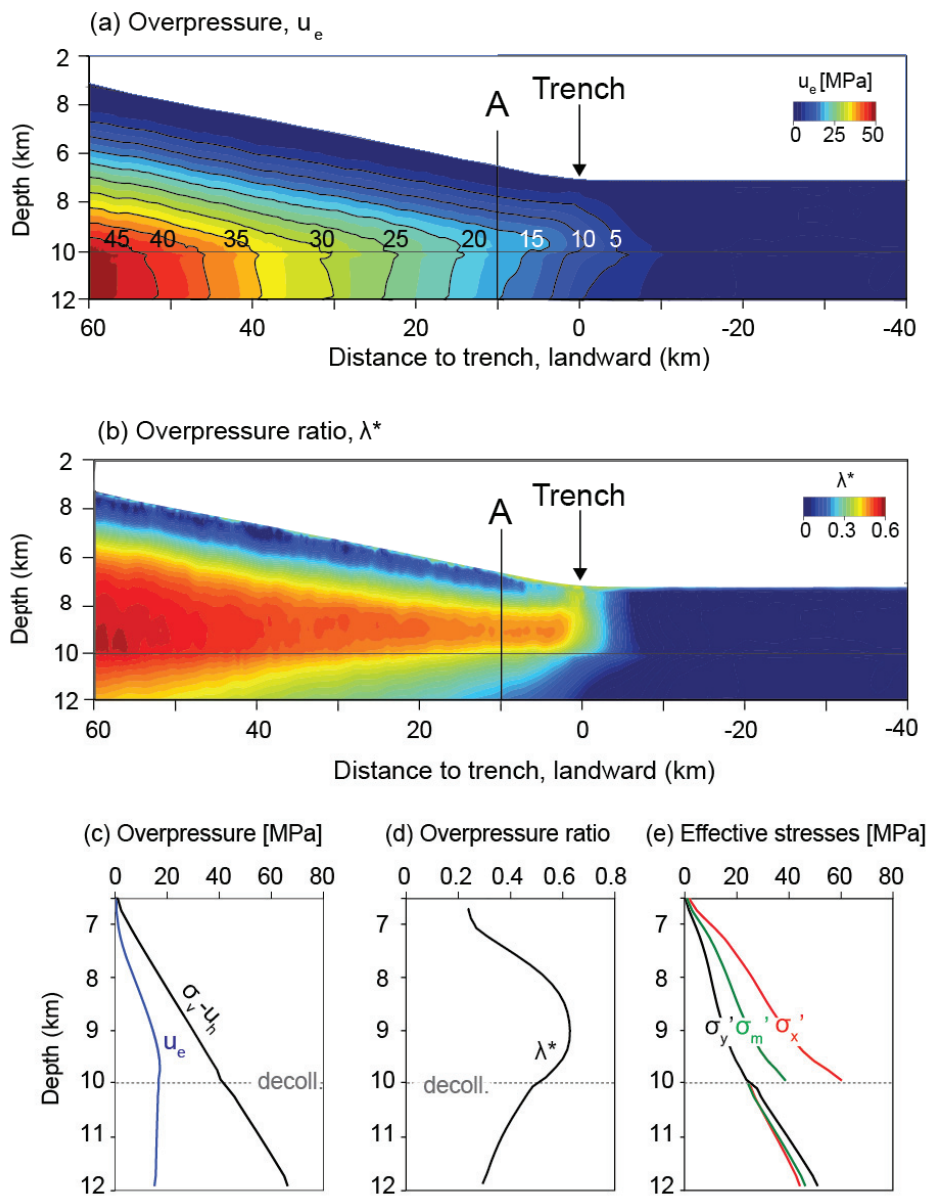


Figure 3.3: (a) Color contours of overpressure at 85 km of tectonic displacement. (b) Color contours of overpressure ratio (λ^*). (c) Overpressure along profile A in (a) together with reduced overburden stress ($\sigma_v - u_h$). (d) Overpressure ratio along profile A. (e) Horizontal (σ'_h , red line), vertical (σ'_y , black), and mean (σ'_m , green line) effective stresses along profile A.

Toward the back of the wedge ($> 40\text{km}$, Figure 3.3a), the overpressure increases continuously all the way to the base of the model. The overpressure contours inside the wedge are sub-parallel to the seafloor showing the fluid in the hanging-wall is drained upward to the seafloor. The footwall overpressure becomes higher than the hanging-wall and the fluid is drained both upward from the footwall to hanging-wall across the décollement and also laterally towards the trench.

3.3.2 Stresses and compression distribution

Due to the lateral tectonic loading, the horizontal effective stress (σ'_x) inside the wedge exceeds the vertical effective stress (σ'_y) (red line vs. black line, Figure 3.3e). The increase of horizontal effective stress also raises the mean effective stresses (σ'_m) (green line, Figure 3.3e) of the wedge sediment. In the footwall, horizontal and mean effective stresses remain lower than the vertical effective stress.

Close to the trench (-5km to $+5\text{km}$, Figure 3.4a, b), there is only a small change in the mean effective stress of the hanging-wall sediment (σ'_m , Figure 3.4a); on the contrary, the deviatoric stress (q) in the hanging-wall notably increases (Figure 3.4b). In the footwall, the mean effective stress decreases toward the trench (dipping contours, e.g. at 30MPa , Figure 3.4a). The footwall mean effective stress then gradually increases but remains low for more than 50km (Figure 3.4a, e.g. 40MPa contour) toward landward direction. The deviatoric stress in the footwall (Figure 3.4b) remains close to its uniaxial value. This low deviatoric stress suggests that there is limited shear stress transferred to the footwall sediment through the décollement.

The shear-stress ratio ($\eta = q/\sigma'_m$) shows the proximity of the stress state of sediment to critical state ($\eta_{cs} = 0.91$, red, Figure 3.4c). Sediment in the far-field remains

at uniaxial-strain state (blue color contours, Figure 3.4c). Starting 10km seaward of the trench and proceeding towards the trench, the stress state of the hanging-wall sediment changes rapidly from uniaxial to critical state (blue to red contours, Figure 3.4c). The hanging-wall sediment is at critical state inside the wedge (red zone Figure 3.4c). Along profile A, the hanging-wall sediment lies on the critical state line in $\sigma'_m - q$ space (red circles, Figure 3.4e). The shear-stress ratio of the footwall sediment is much less than the hanging-wall and it decreases with depth towards the uniaxial value. (Figure 3.4c; triangles vs. black line, Figure 3.4e). The footwall shear stress ratio increases slightly laterally toward the inner wedge (cyan to green, Figure 3.3c) because of a slight increase of shear stress transmitted to the footwall from the décollement as the overburden stress increases (thicker hanging-wall sediment).

Because the mean-effective stress and deviatoric stress above the décollement is much greater than that below, the hanging-wall porosity is much lower than the footwall porosity near the décollement (Figure 3.4d, f). For example, along profile A just above the décollement (white circle, Figure 3.4e), the mean effective stress is 40MPa and the deviatoric stress is 36MPa, and they drop to about 25MPa and 12MPa respectively just below the décollement (white triangle, Figure 3.4e). As a result, the sediment porosity above the décollement is 0.21 and below is 0.24 (Figure 3.4f), leading to a porosity offset of 3 porosity units.

This transient model, which allows for the development of overpressures, predicts lower stresses and less porosity loss compared to drained conditions. I run a drained geomechanical model with the same tectonic rate and material properties. I compare stress and porosity along profile A (color symbols, Figure 3.4e, f) in the transient model with those along a profile in the drained model with the equivalent hanging-wall and footwall

thickness (gray symbols, Figure 3.4e, f). In both drained and transient models, hanging-wall sediments are all at critical state. However, the magnitude of the mean effective stress and deviatoric stress in the transient case is notably less than the drained case due to high overpressure. As a result, the hanging-wall porosity is much higher in the transient case than the drained case (red circles vs. grey line, Figure 3.4f). Similarly, footwall sediment in the transient case also has a lower mean effective and deviatoric stresses than in drained conditions (green triangles vs. grey triangles, Figure 3.4e), thus the footwall porosity in the transient case has a higher porosity (Figure 3.4f) as well. Overall, the porosity offset at the décollement is less pronounced in the transient model than the drained model (Figure 3.4f).

3.3.3 The evolutionary behavior of stress and compression

We track sediment elements in the hanging wall and footwall to study the evolution of stress and porosity. The first tracked elements was initially located in the middle of the upper layer and the second just below the décollement (points A_0 and B_0 , Figure 3.5a). Before the sediments undertake tectonic loading, both tracked elements were at uniaxial strain (K_0) compression condition (A_0 , B_0 , Figure 3.5d, e)

In the hanging-wall, tectonic loading results in a rapid increase of deviatoric stress and a slight decrease of mean effective stress ahead of the trench (A_0 to A_1 , Figure 3.5d). The mean effective stress decreases due to the rapid increase of overpressure. As the sediment reaches the trench (A_1 , Figure 3.5b), its stress state is driven toward critical state (A_0 to A_1 , Figure 3.5d). Because there is limited change in mean effective stress, the slope of the effective stress path is high thus the sediment reaches critical state with little change in mean stress. The stress path curves back toward the critical state line, suggesting that loading conditions are similar to undrained conditions, in which the stress path follows an

iso-porosity curve (green arc, Figure 3.5a). At the same time, the compression curve moves toward the critical state compression line (A_0 to A_1 , Figure 3.5e). The horizontal portion of the compression curve from A_0 to A_1 (Figure 3.5e) indicates no porosity loss along the corresponding portion of the stress path, which follows the iso-porosity line (Figure 3.5a). As the sediment is consumed further into the wedge, mean effective stress increases (Figure 3.5d), and the stresses remain at critical state and compression follows the critical state line (A_1 to A_2 , Figure 3.5d, e). In the footwall, the sediment starts with a quick increase of deviatoric stress and then undergoes a decrease in mean effective stress ahead of the trench (B_0 to B_1 Figure 3.5d; Figure 3.3a). This decrease in mean effective stress results in a slight porosity increase in the footwall (B_1 , Figure 3.5e). Toward the inner wedge, footwall porosity decreases as both mean effective and deviatoric stresses increase (B_1 to B_2 , Figure 3.5d, e).

Comparing the stress and compression paths with the results from the drained model (Chapter 2, Figure 2.7), we find that the fluid-flow coupled model shows less stress increase and less porosity loss. The mean and deviatoric stress increases by 33MPa and 40MPa in the drained model, whereas they only increase by 12MPa and 20MPa in the transient model. As a result, sediment porosity decreases by 0.085 in drained model and decreases by 0.055 (Δn_{total} , Figure 3.5e) in transient model. Thus, the total porosity loss of the tracked overpressured sediment is 35% less than the porosity loss of the tracked drained sediment.

In the transient case, the increase of deviatoric stress contributes to a higher fraction of porosity loss than the drained case as the sediment is incorporated into the wedge. I decompose the total porosity loss (Δn_{total}) along the stress path ($A_0 \rightarrow A_1 \rightarrow A_2$) into mean-induced (Δn_m) and shear-induced porosity loss (Δn_s) (Figures 3.5e). The mean-

induced porosity loss is calculated by assuming that the sediment is compressed along the uniaxial strain stress path and reaches the same mean effective stress at final stage ($A_0 \rightarrow A_k$, Figure 3.5e). Along the K_0 compression line from A_0 to A_k , the porosity decreases by 0.03, thus the mean-induced compression (Δn_m) is 0.03 and it contributes to 55% total porosity loss ($\Delta n_{total}=0.055$, Figure 3.5e). Therefore, the shear-induced porosity loss (Δn_s) is 0.025 and it contributes to 45% of the total porosity loss during tectonic loading. Comparing to the drained case, which has shear-induced compression of 35% (Chapter 2), the higher fraction of shear-induced porosity loss in transient case indicates that the deviatoric stress plays a more important role in sediment compression in overpressured wedge than in the drained wedge.

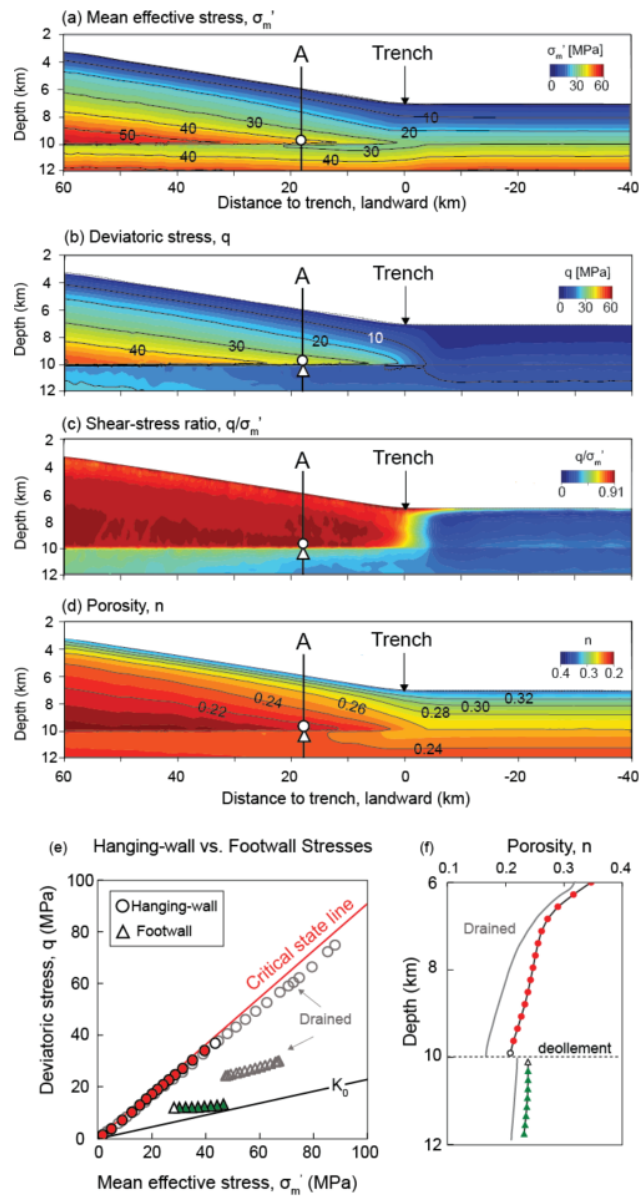


Figure 3.4: (a) Color contour of mean effective stress. (b) Deviatoric stress. (c) Shear-stress ratio (q/σ'_m). (d) Porosity. (e) Mean effective stress and deviatoric stress for hanging-wall (red circles) and footwall (green triangles) along profile A. The white-filled circle and triangle represent the stress state immediately above and below the décollement, respectively. The grey open circle and triangles represent the stress state of the hanging-wall and footwall from the drained model. (f) Porosity along profile A (red: hanging-wall, green: footwall) and porosity results from drained model (grey line).

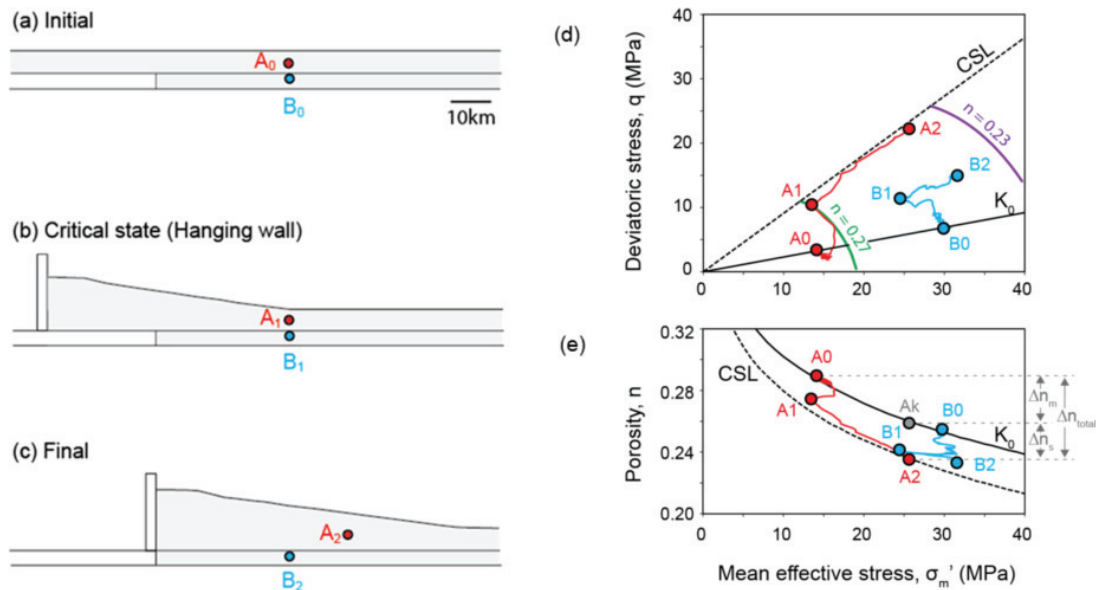


Figure 3.5: Stress and compression paths of hanging-wall (A) and footwall (B) sediment. (a) Initial condition before tectonic loading. A_0 (red dot) is at the middle of upper layer and B_0 (cyan dot) is immediate beneath the décollement. (b) Sediment A arrives the trench sediment and B is below the wedge toe. (c) Final locations of the tracked sediments (A_2 , B_2). (d) Mean stress – deviatoric stress space showing stress paths of hanging wall (red, $A_0 \rightarrow A_1 \rightarrow A_2$) and footwall (cyan, $B_0 \rightarrow B_1 \rightarrow B_2$) sediments. The green and purple arcs represent the iso-porosity curves of 0.27 and 0.23. (e) Corresponding sediment compression paths. Δn_{total} is the total porosity loss from A_0 to A_2 . Δn_m is the mean-induced porosity loss and Δn_s is the shear-induced porosity loss.

3.3.4 Impact of mudrock permeability

We investigate the impact of mudrock permeability on the hydro-mechanical system by comparing four models with high, medium, low permeability conditions (Model 1-3, Table 3.1), and undrained case. The only difference between the first three models is the assigned porosity - permeability relationship (Figure 3.13b, Appendix A). The medium permeability case has the same permeability-porosity relationship as the base model. At a given porosity, the high permeability model has a permeability value that is 10 times higher than the base model. Similarly, the low permeability case is 10 times lower than the base permeability. In the undrained case, there is no flow. We compare stress and pore pressure along the vertical profiles where the thickness of sediment above the décollement is 4km (Figure 3.6a-c). The location of these vertical profiles varies because the different permeability models have slight different wedge geometry. The average surface slope angle between 0 to 40km (Figure 3.6a-c) for the low, medium, and high permeable cases are 4.0° , 3.8° , and 4.1° , respectively.

The hanging-wall overpressure and the associated overpressure ratio significantly increase as the mudrock permeability decreases. The highly overpressured region in the low-permeability case ($\lambda^* > 0.5$, Figure 3.6c) is much larger than that of the high-permeability case (Figure 3.7a). Near the décollement, as the mudrock permeability decreases, the overpressure increases from 12MPa to 26MPa (Figure 3.6e), and the overpressure ratio λ^* increases from 0.23 to 0.54 (Figure 3.6f). The reason for the overpressure increase in the low-permeability case is that the dissipation rate is significantly reduced. With a lower permeability, because the fluid cannot be drained efficiently in time, the pore fluid support a significant amount of the additional load due to tectonic loading. The undrained case (Figure 3.6d) is similar to a model with extremely

low permeability. The overpressure ratio in the wedge is very high ($\lambda^* > 0.8$, Figure 3.6d, f), which results in pore pressure being closer to the overburden stress in the wedge (grey dash line, Figure 3.6e). At the décollement, overpressure and λ^* are elevated in the low permeability and undrained cases. This results into downward flow and increases the overpressure at the top of the footwall. This, together with the low footwall permeability, result in a significant decrease of overpressure and λ^* with depth in the footwall.

As the overpressure increases, the effective stresses of the hanging-wall and footwall sediments decrease. Inside the wedge, the sediments in all three cases are at critical state (red zone, Figure 3.7a-c; circles, Figure 3.7d). The magnitude of the mean effective stress in the high-permeability case is notably higher than the low-permeability case (green dots vs blue dots, Figure 3.8d). In the footwall, with a lower permeability, the stress state is much closer to uniaxial (blue vs. green triangles, Figure 3.7d). The undrained case shows very low effective stress and shear stress. In addition, the footwall sediment is closely aligned to the uniaxial strain (K_0) stress path (Figure 3.7e).

The high overpressure and low effective stress associated with decreasing permeability result in less porosity decrease, especially in the hanging-wall sediments. (blue vs. green, Figure 3.7f). As a result, the porosity offset at the décollement decreases with decreasing mudrock permeability. The undrained case has the greatest porosity in the hanging-wall. This is because under undrained conditions there is no volumetric change, as fluid cannot drain from the pores. In this case, we see a much greater hanging-wall porosity than the footwall (grey-dash line, Figure 3.7f).

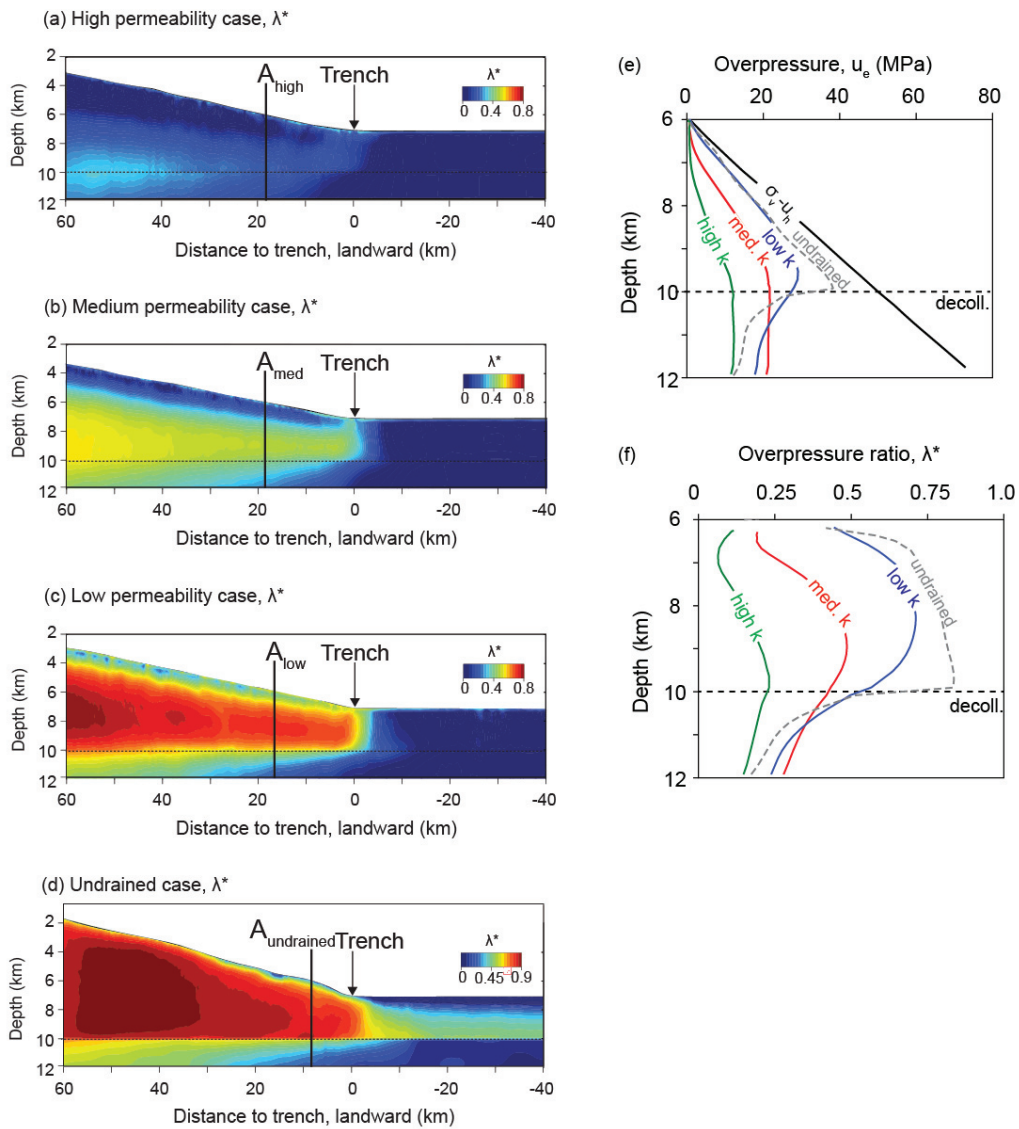


Figure 3.6: Impact of permeability on overpressure (Table 3.1, Model 1-3). (a)–(c): Overpressure ratio (λ^*) from high-, medium-, and low-permeability case. The medium-permeability case is the same as the base model (Model 1, Table 1). (d) λ^* distribution from undrained model. (e), (f): Comparison of overpressure and overpressure ratio along vertical profiles A_{high} , A_{med} , A_{low} , and $A_{undrained}$ in (a)–(d). Locations of these profiles are chosen where the hanging-wall thickness is 4 km. Green, red, blue, and grey-dash lines represent high, medium, low permeability, and undrain cases, respectively.

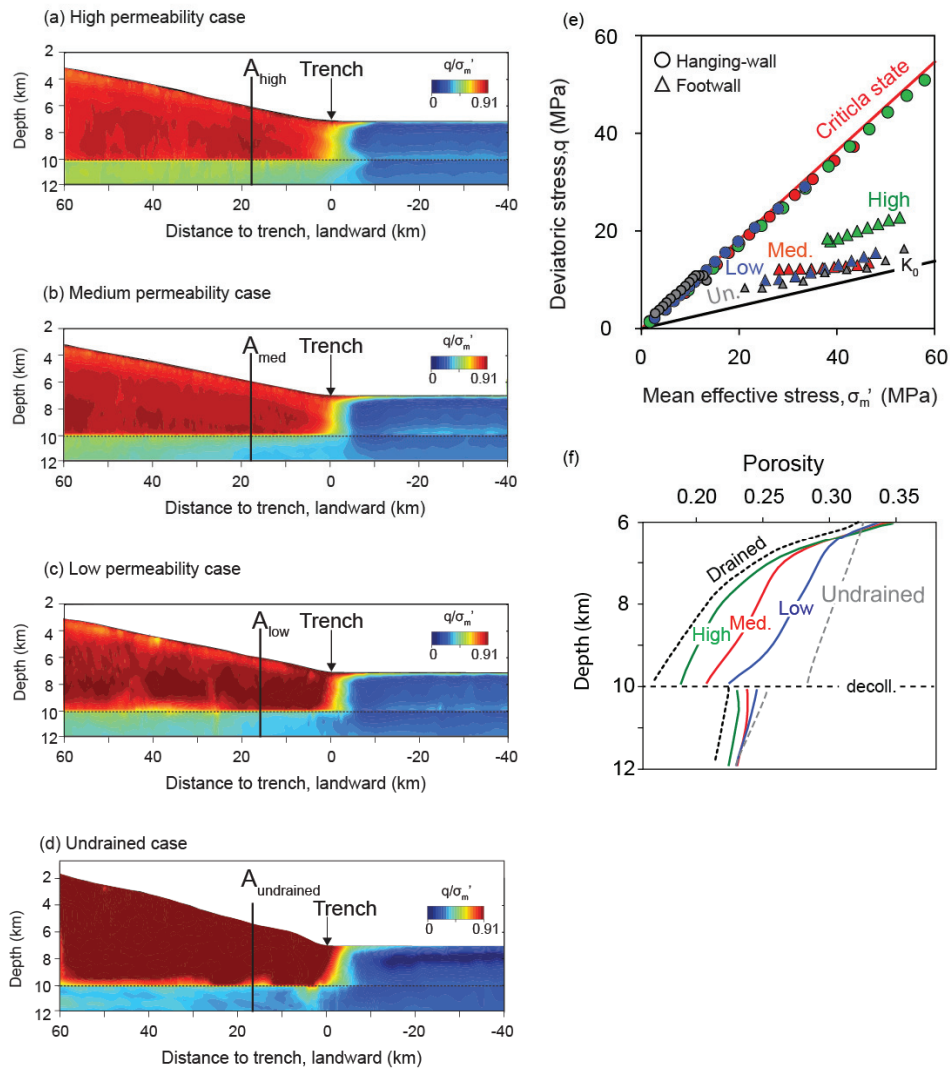


Figure 3.7: Impact of permeability on stress and compression. (a)-(c) Shear-stress ratio for high-, medium-, and low- permeability cases. (d) Overpressure ratio distribution of the undrained case. (e) Mean effective stress and deviatoric stress along vertical profiles A_{high} , A_{med} , A_{low} , and $A_{undrain}$ in (a)-(d). Circles represent stress states in the hanging wall and triangles in footwall. (f) Porosity-depth curves along vertical profiles A_{high} , A_{med} , A_{low} , $A_{undrained}$ and in drained condition. Green, red and blue colors represent high, medium and low permeability case, respectively. The black line in (f) shows the drained porosity-depth curve from Chapter 2. The grey dash line shows the porosity-depth profile from the undrained case.

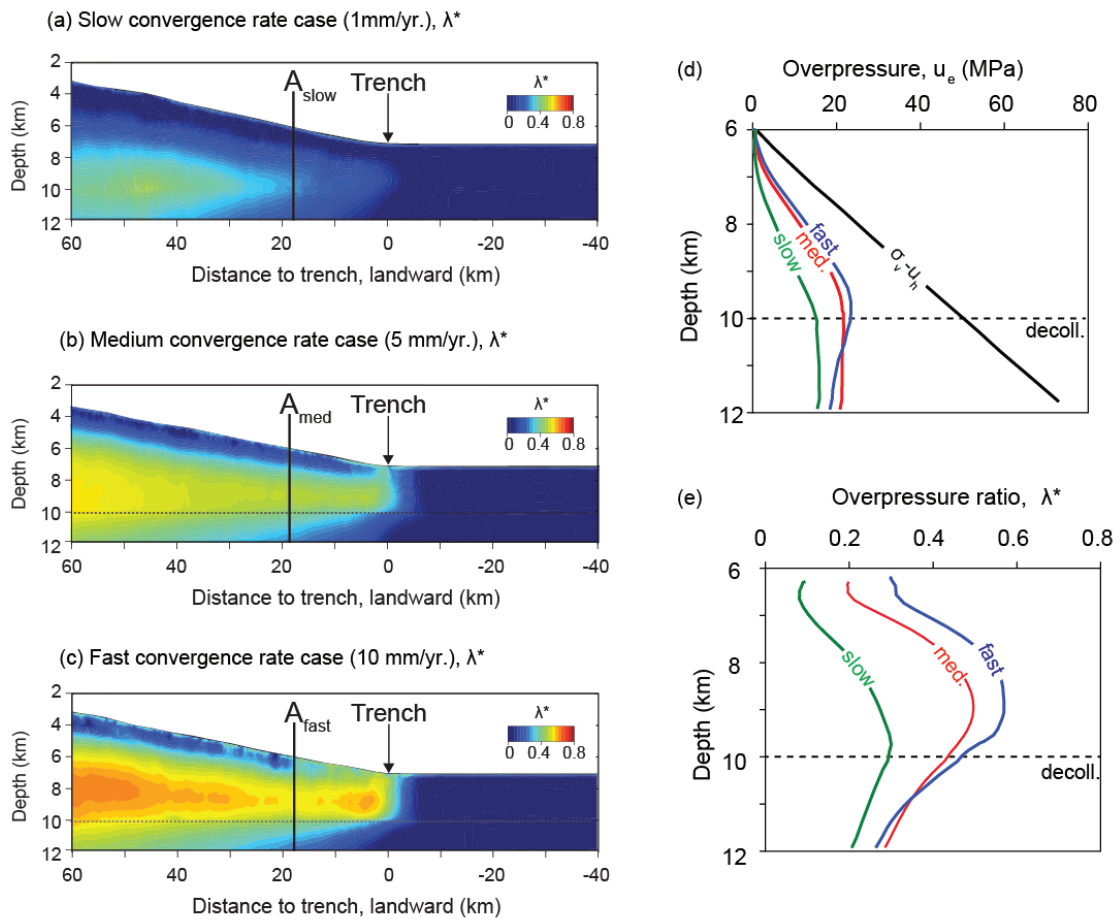


Figure 3.8: Impact of convergence rate on overpressure (Table 2, Model 1, 4, and 5). (a) –(c): Overpressure ratio (λ^*) from slow-, medium-, and fast-convergence case. The medium-convergence case is the same as the base model (Model 1, Table2). (d) Comparison of overpressure along vertical profiles A_{slow} , A_{med} , and A_{fast} in (a)-(c). Locations of these profiles are chosen where the hanging-wall thickness is 4km. (e) Overpressure ratio from vertical profile A_{slow} , A_{med} , and A_{fast} in (a)-(c). Green, red, and blue represent slow-, medium-, and fast- convergence rate cases.

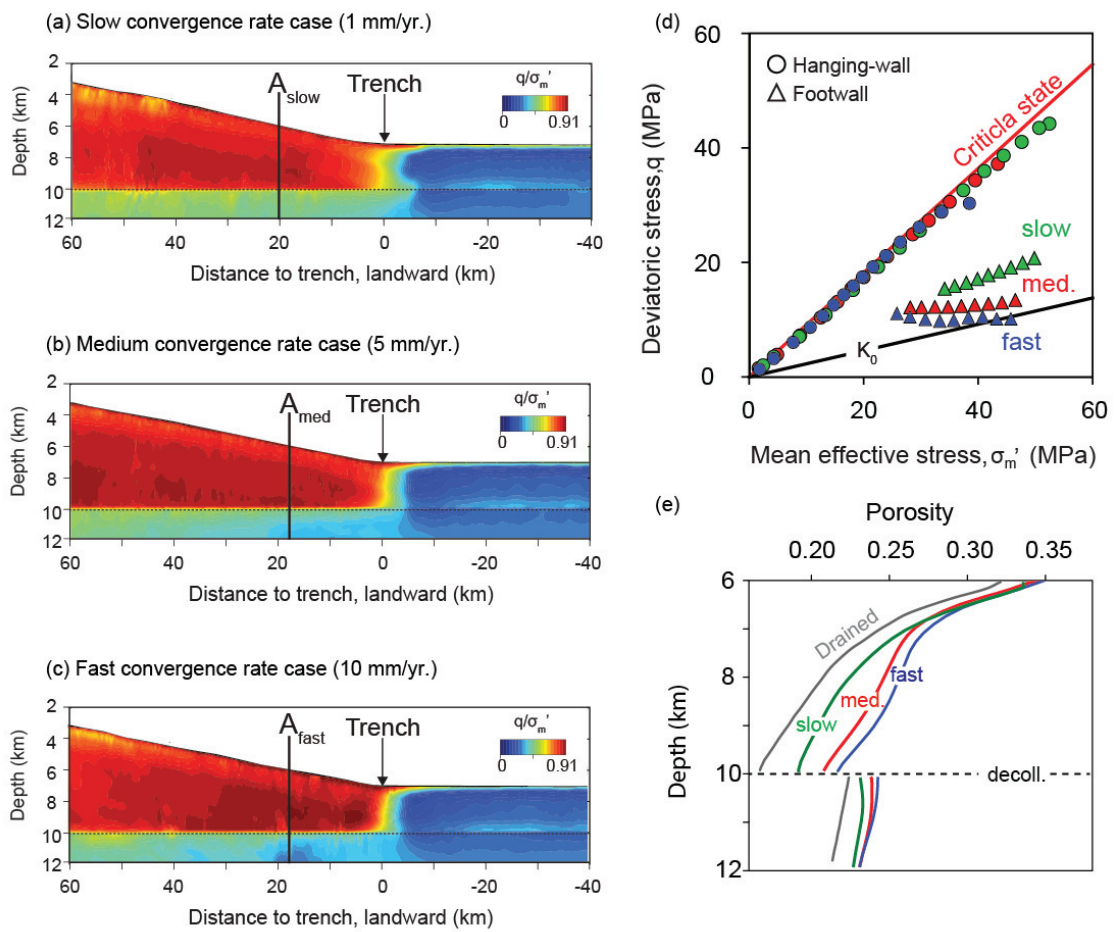


Figure 3.9: Impact of convergence rate on stresses and compaction (a)-(c). Shear-stress ratio for slow-, medium-, and fast- convergence rate case. (d) Mean effective stress and deviatoric stress along vertical profiles A_{slow} , A_{med} , and A_{fast} in (a)-(c). Circles represent stress states in the hanging wall and triangles in footwall. (e) Porosity-depth curves along vertical profiles A_{low} , A_{med} , A_{high} in (a)-(c) and in drained condition. Green, red and blue colors represent high-, medium- and low- permeability case, respectively. The grey line in (e) shows the porosity-depth curve from drained model in Chapter 2.

3.3.5 Impact of convergence rate

I explore the influence of convergence rate on pressure and stress with 3 models having convergence rates of 1 mm/yr. (slow), 5 mm/yr. (medium), and 10 mm/yr. (high) (Figure 3.8). The medium-convergence-rate case is the same as the base model.

Similarly to the low-permeability case, a higher convergence rate results in a higher magnitude of overpressure and a wider range of highly overpressured region (yellow, Figure 3.8c). At the décollement, as the convergence rate increases from 1 mm/yr. to 10 mm/yr., the overpressure increases from 15MPa to 22 MPa (Figure 3.8d), and the overpressure ratio increases from 0.29 to 0.43 (Figure 3.8e). The hanging-wall overpressure increases because a higher convergence rate increases the loading rate (increase of stress per unit time). Although the drainage capability for the sediment in the higher convergence case increases as well (due to high porosity thus high permeability), the increase of loading rate exceeds the dissipation rate so much therefore resulting in an overall increase of pore pressure. Another interesting result is that there is a significant overpressure decrease along the depth in the footwall in high convergence rate case (blue, Figure 3.8d). The reasons for the decrease in footwall overpressure are two fold. First, the high convergence rate increases the hanging-wall overpressure and thus causes a greater overpressure contrast between the hanging-wall and footwall. Second, the high hanging-wall overpressure increases the footwall overpressure near decollement because the pressure propagates downwards. The deeper footwall sediment is less influenced by the downward flow from the hanging-wall and thus shows a lower overpressure than that near the decollement.

As the convergence rate increases, the mean effective stress and the deviatoric stress decrease in the hanging-wall (Figure 3.9d). As a result, porosity loss in the hanging-

wall is less than in the slow convergence rate case (Figure 3.9e). Specifically, porosity offsets resulting from high and low convergence rates are 2 and 4 porosity units, respectively (Table 3.1, Model 4 vs. Model 5).

The hanging-wall sediment remains at critical state for all three cases (Figure 3.9d). In contrast, the shear-stress ratio of the footwall sediment decreases with an increased convergence rate (Figure 3.9d) because the greater overpressure results in less basal shear stress transmitted into the footwall.

3.4 DISCUSSION

I show the evolution of stress, porosity, and pore pressure in an accretionary wedge system using a transient forward geomechanical model. Here, I discuss the new findings, physical insights, applications, and model limitations.

3.4.1 Overpressure generation mechanism and implications

The resultant overpressure variation in an accretionary wedge system depends on three major parameters: the loading rate, the dissipation rate, and the compressibility. In an accretionary wedge, the compressional deformation causes the increase of mean and shear stress and both of them drive overpressure generation. The resultant stresses and pore pressure then affect the subsequent porosity loss, the permeability and the deformation. A high loading rate will positively impact the overpressure generation. The dissipation rate depends on the intrinsic sediment permeability and the drainage path. A lower permeability or a longer drainage path limits the sediment's drainage ability and result in overpressure increase. The compressibility impacts the volumetric strain and the amount of fluid that needs to be drained. A lower compressibility tends to generate a higher overpressure.

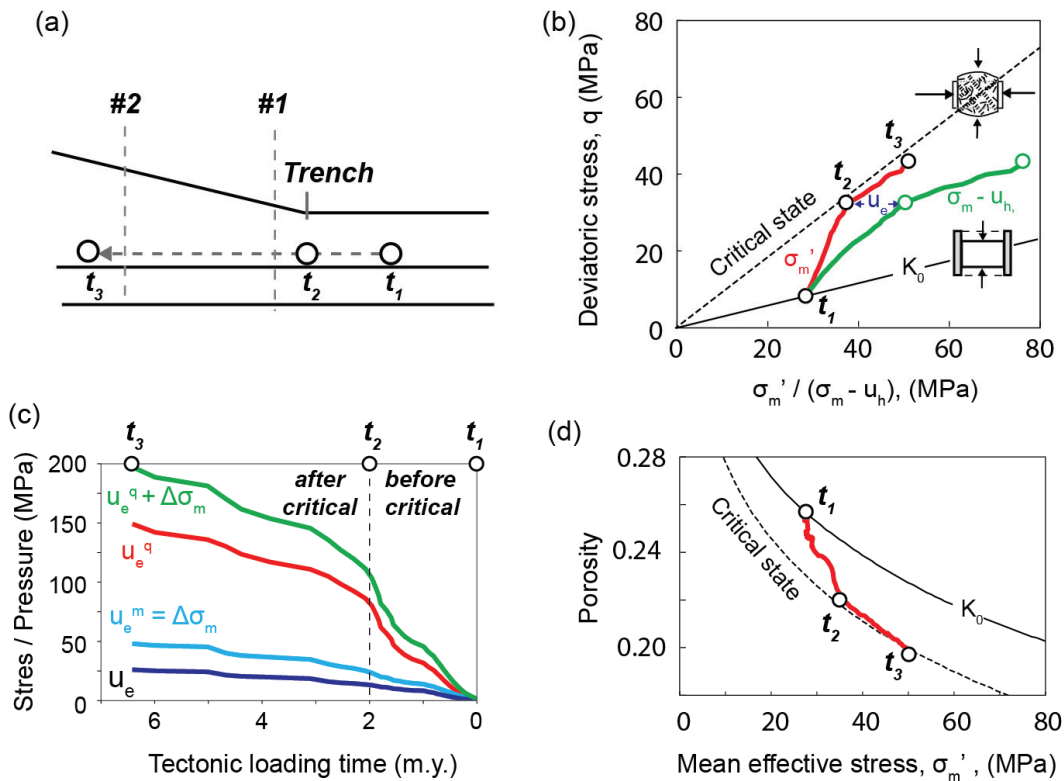


Figure 3.10: (a) Schematic figure of the trajectory of a tracked sediment as it is incorporated into the prism. #1 and #2 are the approximate location of the vertical profiles in Fig.1b. t_1 , t_2 and t_3 illustrate the locations where the tracked sediment starts to feel tectonic loading, reach critical state, and the final location. (b) Stress history. Red: mean effective stress versus deviatoric stress. Green: reduced mean total stress (total stress minus hydrostatic pressure) versus deviatoric stress. The horizontal distance between the red and green line is the overpressure (u_e). (c) Pore pressure generation components versus loading time. Dark blue: the ultimate overpressure from model simulation. Cyan: the increase of total mean stress, which equals the mean-induced overpressure (u_e^m). Red: the overpressure generated by shear stress. Green: the total overpressure generated by total mean stress and shear stress. The vertical distance between the total overpressure (green line) and the resultant overpressure (dark blue) is the amount of drainage. (d) The compression path along t_1 to t_3 in (b).

A few factors cause the hanging-wall overpressure to be higher than the footwall overpressure near the trench and the dominant role is the rapid increase of total mean stress and deviatoric stress in the hanging-wall. I deconvolve (Figure 3.10, Appendix C) the loading components that induce overpressure as a sediment element begins to undertake tectonic loading and finally reaches the inner wedge (t1-t2-t3, Figure 3.10a). The tracked sediment is located immediately above the decollement. The induced overpressure is caused by the sum of the increase of overpressure by total mean stress ($\Delta\sigma_m$) and the increase of overpressure by shear stress (u_e^q) (red line Figure 3.10c). These two components rise rapidly from t1 to t2 and then moderately thereafter from t2 to t3 (Figure 3.10c). Before the sediment reaches critical state, the shear-induced overpressure (u_e^q) is much greater than the mean-induced overpressure (cyan vs. red, Figure 3.10c). From t1 to t2, the average increase rate of shear-induced-overpressure (u_e^q) is 41MPa/m.y. whereas the average increase rate of mean-induced overpressure (u_e^m) is only 12.5MPa/m.y. (Figure 3.10c). It means that the increase of shear stress ratio plays a more significant role in overpressure generation as the stress state transcends from uniaxial strain to critical state. After the sediment reaches critical stress state, from t2 to t3, the increase rate of the shear-induced overpressure (u_e^q) and mean-induced overpressure drops by 64% and 56% and becomes 14.8MPa/m.y. and 5.5MPa/m.y., respectively (Figure 3.10c). As a result, the increase rate of the resultant overpressure (u_e , 3.Figure 10c) after the sediment has reached critical state drops by 61% compared to before, reflecting a much slower overpressure increase as the sediment is incorporated into the inner wedge. The difference between the total induced overpressure (green, Figure 3.10c) and the actual resultant overpressure (dark blue, Figure 3.10c) records the pore pressure dissipation. This dissipation is also reflected by the decrease of porosity from t1 to t3 (Figure 3.10d).

In the hanging-wall, the pore pressure is dissipated to both upward to the seafloor and downward into the footwall. The pore pressure dissipation causes the increase of mean effective stress and shear stress in the hanging-wall and results in porosity loss (Figure 3.10d). As the porosity decreases, the hanging-wall permeability decreases and then it limits the subsequent sediment drainage under continuous tectonic loading. As the effective stress increases and porosity decrease, the compressibility increases in the hanging-wall. In the footwall, the increase of total mean stress is mainly from the increase of overburden stress. Because there is no lateral loading source, the increase of total mean stress and shear stress (q , Figure 3.4b) is significant lower than the hanging-wall. Although the entire footwall has a longer drainage path to the seafloor and a lower overall permeability compared the hanging-wall, the geomechanical modeling results show that these overpressure generation factors are not high enough to outweigh the impact of much less loading source in the hanging-wall than in the footwall. As a result, the hanging-wall overpressure is greater than the footwall near trench.

Toward the inner wedge, the footwall overpressure becomes greater than the hanging-wall overpressure (40~60km, Figure 3.3a) due to a great increase of overburden load, a longer drainage path (toward seafloor), low-permeable overlying hanging-wall sediment, and a higher footwall compressibility (than the inner wedge). As the footwall sediment moves to deeper depths underneath the wedge with thicker overlying sediment, the overburden load and the drainage path increase steadily. On the contrary, the increase rate of total mean stress and shear stress in the hanging-wall actually decreases ($t_2 - t_3$, green line, Figure 3.10b; cyan line, Figure 3.10c). Thus the contrast of the loading source between the hanging-wall and footwall-wall decrease. In addition, the sediment immediately above decollement at inner wedge have a much lower porosity than the

hanging-wall (dark red region, Figure 3.4d), which suggests that the inner wedge sediment has a much lower permeability than the footwall. This low-permeable overlying sediment significantly impedes the footwall to drain upward. Thus, the footwall sediment is mainly drained laterally to the trench through long drainage path. The relative high footwall porosity also indicates a higher footwall compressibility than the hanging-wall, which is another factor that assists to generate high overpressure in the footwall.

The region in front of the trench in the hanging-wall is a transition zone (blue to red, Figure 3.4c) where the stress states vary rapidly from uniaxial to critical state. In the overpressured accretionary wedge, this transition zone is much narrower than that of the drained condition. The transition zone is about 20km wide (Gao et al., 2018) in drained case whereas only 10km in the transient case. Decreasing the permeability and increasing the convergence rate reduces the width of transition zone (Figure 3.7, 3.9). Under drained condition, both mean effective stress and the deviatoric stress increase significantly and reach critical state at high effective stress levels. However, in the overpressured accretionary wedge, the sediment reaches critical state at lower stresses with rapid increase of deviatoric stress (high slope from A_0 to A_1 , Figure 3.6e). This means the sediment compresses less and fails easier at a given depth.

My model results suggest that the dewatering rate near trench is strongly impacted by the deviatoric stress. By analyzing the field porosity distribution and sediment movement trajectories, previous studies (Bekins & Dreiss, 1992; Karig, 1990) suggest that the dewatering process (or termed “fluid production”) is most pronounced near the deformation front. This understanding is confirmed by our transient geomechanical model. In addition, I find that the shear-induced dewatering may play an even greater role in dewatering than the mean effective stress. The physical foundation for shear-induced

dewatering (porosity loss) is that high shear stress help to rotate the platy minerals into preferred orientation thus accelerate the dewatering (Bray & Karig, 1985). As the sediment moves toward trench (t1-t2, Figure 3.10a), the stresses transcends from uniaxial strain (K_0) to critical state (red line, 3.10b). This occurs as the sediment passing through the transition zone and reaching the wedge toe. The rapid increase of mean effective stress and deviatoric stress leads to sediment compression and fluid expulsion. Comparing before and after the sediment reaches the critical state, the averages porosity loss rate in the transition zone (K_0 to critical state) is three times greater than inside the wedge. As the sediment moves through the transition zone from t1 to t2 (Figure 3.10a, d), the shear-induced dewatering accounts for 66% of the total dewatering in transition zone.

The inability for fluid to escape during tectonic loading results in overpressure, which limits the sediment compression, and reduces the porosity offset at the décollement. At equivalent depth below seafloor, sediment with higher overpressure has less effective stress and thus higher porosity (e.g. Figure 3.7d, 3.8e). With high overpressure, the effective stress and deviator stress difference between the hanging wall and footwall sediments is less pronounced. Thus, there is less porosity offset at the décollement in high overpressured accretionary wedges. The porosity variation predicted by the geomechanical model (e.g. Figure 3.4d) can be used to better understand the permeability and velocity structures in fields. Using empirical or experimental relationships of porosity vs. permeability and porosity vs. V_p velocity, the spatial distribution of permeability and velocity can be obtained (e.g. (Gao et al., 2018)). The wedge sediment has a lower porosity than that of the footwall sediment near décollement. Thus, the hanging wall sediment is expected to have a lower matrix permeability and higher seismic velocity than that of the footwall sediment.

3.4.2 Comparison with critical taper theory

In the transient cases, the surface angles predicted by the geomechanical models do not show good agreement with that predicted by the critical taper theory. The pressure ratio is defined as follows (Davis et al., 1983):

$$\lambda = \frac{u - \rho_1 g D}{\sigma_v - \rho_1 g D} \quad (7)$$

where u is pore pressure, ρ_1 is water density, and D is the water depth between the seafloor and the sea level.

I calculate the average surface slope angle and the pore pressure ratio (λ) of the hanging-wall sediment in the area between the trench (0km) and 40km landward of trench. Figure 3.11 shows the distribution of pore pressure ratio of the base model. The grey box (Figure 3.11a) shows the region where I calculate the average pore pressure ratio in the hanging-wall. For the low-, medium- and high- permeability cases, the average pore pressure ratios (λ) are 0.79, 0.66, and 0.53. The surface slope angles of low-, medium, and high- permeability cases predicted by the geomechanical models are 4.0° , 3.8° and 4.1° , respectively. Substituting the pore pressure ratios, sediment internal strength ($\mu_s = 0.44$), basal friction coefficient ($\mu_b = 0.2$), and the average bulk density (based on porosity distributions, e.g Figure 4d) into the force balance equation in critical taper theory (Davis et al., 1983), I obtain that the surface slope angles predicted by the critical taper theory equal 2.9° , 3.9° , and 4.6° for low-, medium-, and high- permeability cases, respectively. The discrepancy between the geomechanical model and critical taper theory predictions is most likely due to the assumption of constant pore pressure ratio in the critical taper theory. I show the pore pressure ratio along the vertical profiles located at the distance of 0km, 10km, 20km, and 30km landward distance to the trench (Figure 3.11a,

b). Geomechanical models show that the pore pressure ratio near the seafloor is lower than in deeper sections. The pore pressure ratio also varies significantly along the decollement (Figure 3.11b). Along the decollement (10km depth, Figure 3.11b), from 0km to 30km landward distance to trench, the pore pressure ratio increases from 0.58 to 0.7. This large variation of pore pressure ratios shows that the assumption of constant pore pressure ratio in critical taper theory is not valid in overpressured accretionary wedge system. Thus it is not recommended to use critical taper theory to quantitatively predict the stress and pressure distribution in overpressured wedges. This finding indicates that using the surface slope parameter to inverse calculate overpressure may yield erroneous results. Under drained conditions, the geomechanical models show more consistent results with the critical taper theory models (Gao et al., 2018).

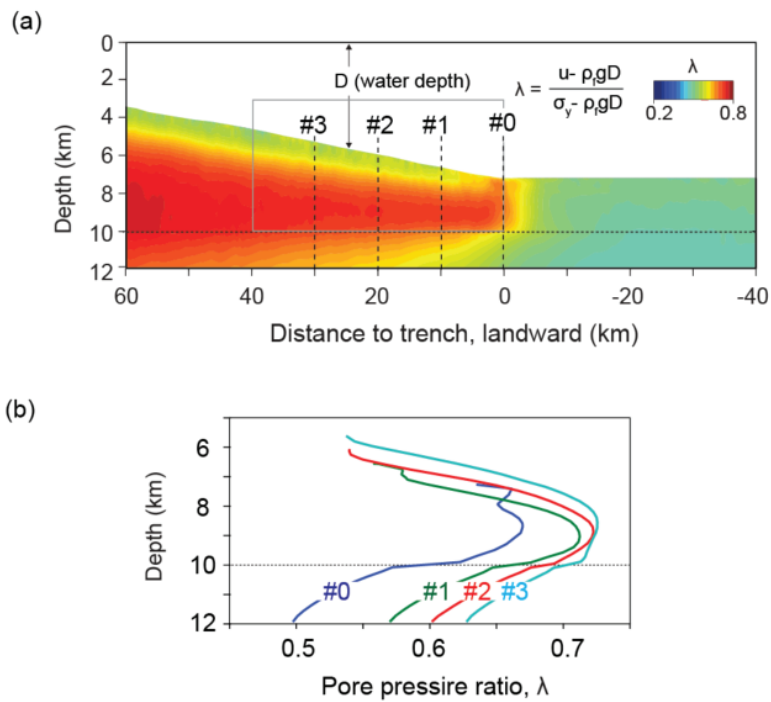


Figure 3.11: (a) Color contour of pore pressure ratio. #0, #1, #2, and #3 are the locations of the vertical profiles shown in (b). They are at 0km, 10km, 20km, and 30km landward distance to trench, respectively. The grey box shows the region in which I extract the pore pressure ratio to calculate the average value: from 0km to 40km landward distance to the trench. (b) Pore pressure ratio along the vertical profiles in (a).

3.4.3 Strain evolution

Shortening and elongation occur concurrently as the sediment is incorporated into an accretionary wedge (Figure 3.12). I illustrate the sediment deformation by plotting the associated strain ellipses of a tracked sediment element (Figures 3.12). The sediment element was initially located in the middle of the top layer and started to experience tectonic loading at about 7km in front the trench (Figure 3.12a). At the beginning, the sediment is deformed under vertical uniaxial strain by burial and the minimum principal strain axis is horizontal (red, Figures 3.12a). As the sediment moves past the trench, the minimum principal strain rotates toward vertical (gray line, Figure 3.12b). At distances greater than 7 km landward from the trench, the sediment experiences vertical elongation (Figure 3.12 a, b). Although there is both vertical elongation and horizontal shortening at inner wedge, the magnitude of the shortening strain is higher than that of the elongation strain. The net effect is that the volumetric strain continues to increase. These results are qualitatively very similar to those derived by Morgan et al. (1994) based on kinematic modeling. The results on strain rotation also show agreement with the strain analysis indicated from fabric orientations (Henry et al., 2003; Housen, 1997; Housen et al., 1996; Owens, 1993) and *P* wave anisotropy (Brückmann et al., 1997) of Nankai and Barbados accretionary wedges.

The magnitude of strain change under transient conditions is much lower than under drained conditions (Chapter 2, Figure 2.12). This is because volumetric deformation in the transient wedge depends on the dissipation of overpressures. In addition, the strain rotation

from horizontal to sub-vertical (ϵ_3 , Figure 3.12b) occurs within a much shorter distance in transient conditions than in drained conditions.

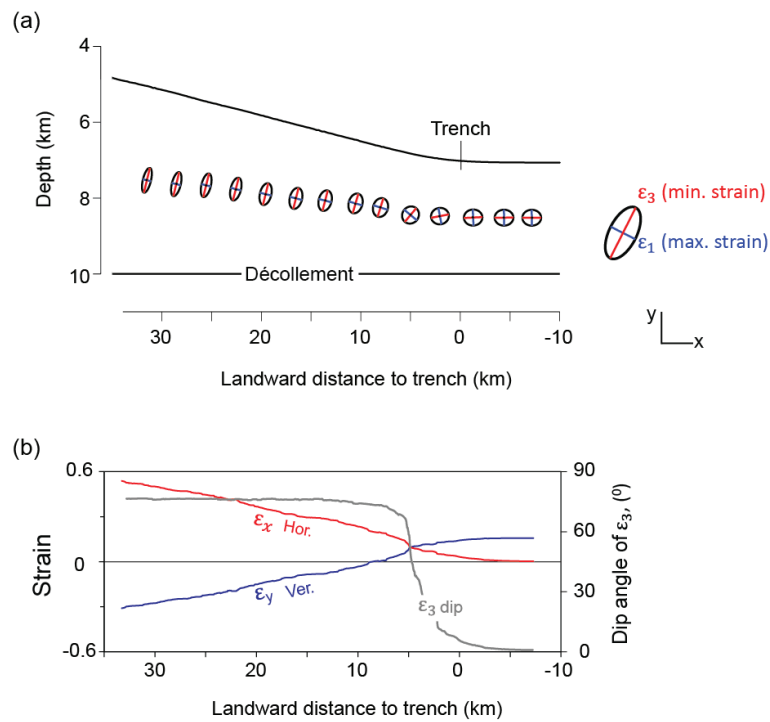


Figure 3.12: Evolution of strain of a sediment element that passes into the accretionary wedge (transient model, base case). (a) Evolution of strain ellipse. The dark blue and red axes show the maximum (ϵ_1) and minimum (ϵ_3) strain orientations, respectively. Sediment starts to experience tectonic loading at about 7km seaward of the trench. (b) The evolution of the horizontal (ϵ_x) and vertical strain (ϵ_y) with distance to the trench. I denote shortening as positive and elongation as negative. The rotation of the minimum principal strain (ϵ_3) orientation is shown with the grey line.

3.4.4 Model limitations and future directions

This study provides great physical insights of accretionary wedge system, but I am also aware of the limitations and the future directions for improvements.

First, the current models have considered the deformation due to sediment compression but they do not consider the development of individual faults. Adding mechanisms for fault generation in future studies will improve the understanding of stress, fluid flow, and internal structures in accretionary wedges. Second, the current study does not investigate the effect of a permeable decollement. A permeable decollement may induce significant lateral flow and limit the overpressure development. Thirdly, more tectonic loading scenarios need to be included for future field studies. For a particular field case, local geologic events such as deposition, erosion, compression or extension events should be included to more accurately predict the stress and pressure through geologic history.

3.5 CONCLUSIONS

I studied the stress, porosity, and pore pressure evolution in a critically stressed wedge from the onset of tectonic loading to a steady wedge. The lateral tectonic loading results in overpressure in both hanging-wall and footwall. Near the trench, the hanging-wall overpressure is greater than the footwall overpressure whereas it is lower than the footwall overpressure toward the inner wedge. The great hanging-wall overpressure near the trench is driven by the rapid increase of both total mean stress and deviatoric stress. This highly overpressured frontal wedge drive the fluid to flow upward to the seafloor and downward into the footwall. The footwall sediment near trench experiences decrease of mean effective stress due to the downward flow from the hanging-wall. The footwall

overpressure is higher than the hanging-wall toward the inner wedge because of the steady increase of loading source (overburden stress) and drainage length, low-permeability overlying sediment, and higher compressibility (than the inner wedge). The deviatoric stress plays a more important role in sediment compression in overpressured wedge than in the drained wedge. The shear-induced compression accounts for 45% of total porosity loss during tectonic loading (base transient model). The overpressure causes the sediment to reach critical state at low stresses thus there is much less porosity loss in an overpressured accretionary wedge than in a drained wedge. By tracking the sediment porosity loss in the hanging-wall (in base case), I find that porosity loss in the overpressured accretionary wedge is about 35% less than in a drained wedge. This further results in less pronounced porosity offset across the decollement. Decrease the rock permeability and increase the convergence rate increase the overpressure generation, decrease the sediment compression, and decrease the porosity offset at the decollement.

Table 3.2: Nomenclature

Symbol	Description	Dimensions
K_0	Geostatic stress ratio	Dimensionless
k	Intrinsic permeability	L^2
n	Porosity	Dimensionless
q	Deviatoric stress	M/LT^2
μ_w	Friction coefficient at wall contact	Dimensionless
μ_s	Sediment internal friction coefficient	Dimensionless
μ_b	Basal friction coefficient	Dimensionless
ϕ'_s	Sediment internal friction angle	Dimensionless
ϕ_b	Basal friction angle	Dimensionless
σ'_x	Horizontal effective stress	M/LT^2
σ'_y, σ'_v	Vertical effective stress	M/LT^2
σ'_1	Maximum principal effective stress	M/LT^2
σ'_2	Intermediate principal effective stress	M/LT^2
σ'_3	Minimum principal effective stress	M/LT^2
σ'_m	Mean effective stress	M/LT^2
λ	Pore pressure ratio	M/LT^2
λ^*	Excess pressure ratio	M/LT^2
τ_{slip}	Décollement strength	M/LT^2
ε_1	Maximum principal strain	Dimensionless
ε_2	Minimum principal strain	Dimensionless
ε_x	Horizontal strain	Dimensionless
ε_z	Vertical strain	Dimensionless
η	Shear stress ratio	Dimensionless
η_{K_0}	Slope of K_0 state line	Dimensionless
η_{cs}	Slope of critical state line	Dimensionless
ε_v	Volumetric strain	Dimensionless
ρ_f	Fluid density	M/L^3
μ_f	Fluid viscosity	M/LT
K_f	Fluid bulk modulus	M/LT^2
K_s	Solid bulk modulus	M/LT^2

3.6 Appendix A: material properties

Figure 3.13 shows compression, permeability and coefficient of consolidation behaviors of the applied materials.

Figure 3.14 shows the hardening relationship of the applied material. Table 3.3 is the applied SR3 model parameters. More detailed material equations and descriptions can be found in Gao et al. (2018) and Crook et al. (2006).

Table 3.3: SR3 material model parameters

Symbol	Parameter Name	Value
A	Material constant	-0.28
B	Material constant	-0.28
c	Material constant	-2
E_{ref}	Reference Young's modulus	40 MPa
$\sigma_m^{t_0}$	Initial tensile intercept	-0.085 MPa
$\sigma_m^{c_0}$	Initial compressive intercept	1 MPa
n_{sr3}	Material constant	1.3
n_e	Material constant	0.3
β	Friction parameter	60°
ν	Poisson's ratio	0.25

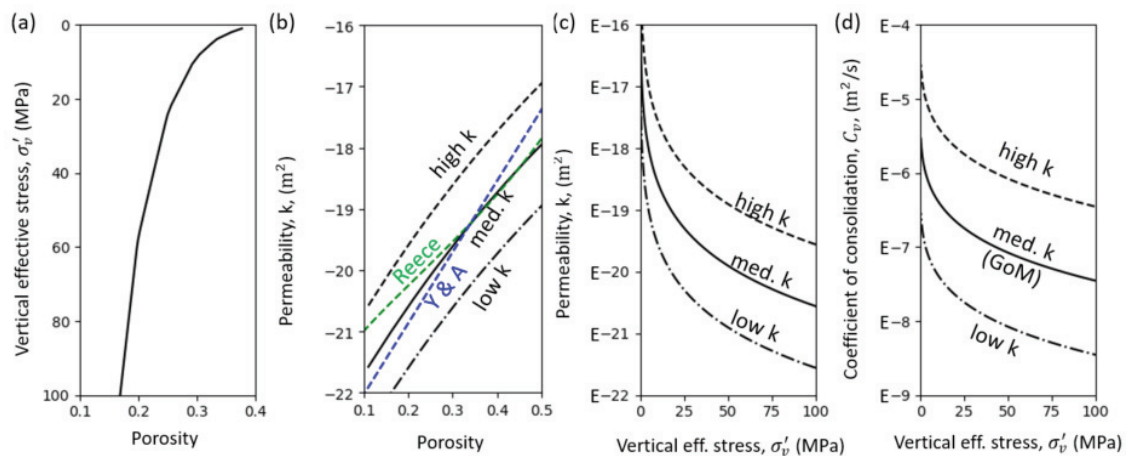


Figure 3.13: (a) The porosity and vertical effective stress relationship at uniaxial strain condition. (b) The porosity and permeability relationships for high-permeability (black dash, Model 3), medium permeability (black solid, Model 1), and low-permeability (black dashed-dot) cases (Table 1). The green and blue dash lines represent the permeability relationship of the mudrocks in Nankai (Reece et al., 2013) and Gulf of Mexico (Yang and Aplin, 2010) with 65% clay fraction. (c) The permeability and vertical effective stress relationship. (d) The coefficient of consolidation and vertical effective stress relationship. The relationship of the medium case matches the experimental results of the Gulf of Mexico mudrocks.

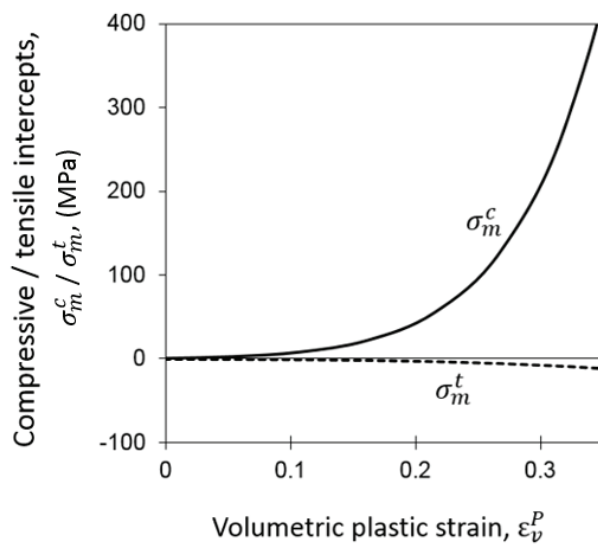


Figure 3.14: Input hardening: relationship among volumetric strain (ϵ_v^p), compressive intercept σ_m^c (solid line), and tensile intercept σ_m^t (dashed line).

3.7 Appendix B: Governing equation and numerical discretization

Elfen is a finite-element code that simulates the evolution of geologic system by solving coupled hydro-mechanical equations, including Darcy's law, stress equilibrium equations, and constitutive laws for rock behavior. A Lagrangian reference frame is used for the rock phase, and an Eulerian reference frame is used for the fluid phase. The mechanical equations are solved explicitly and the hydraulic equations are solved implicitly.

Simulation of the evolution of geologic systems often involves large deformation and strain. Elfen uses two strategies to take into account these deformations and strains. First, Elfen uses a large-strain formulation for the constitutive equations of rocks in the model to correctly express their stress-strain behavior at large strain and rotation. Second, Elfen uses optimized automated remeshing techniques to remesh elements in the model that have been excessively distorted due to large strains, thereby preventing the failure of the numerical implementation.

1) Mechanical equations

The momentum balance equation describes the equilibrium of stresses and momentums (Lewis & Schrefler, 1998):

$$\mathbf{L}^T \boldsymbol{\sigma} + \rho_b \mathbf{g} = \rho_b \ddot{\mathbf{u}} \quad (\text{B1}),$$

$$\mathbf{L}^T = \begin{pmatrix} \frac{\partial}{\partial x} & 0 & 0 & \frac{\partial}{\partial y} & 0 & \frac{\partial}{\partial z} \\ 0 & \frac{\partial}{\partial y} & 0 & \frac{\partial}{\partial x} & \frac{\partial}{\partial z} & 0 \\ 0 & 0 & \frac{\partial}{\partial z} & 0 & \frac{\partial}{\partial y} & \frac{\partial}{\partial x} \end{pmatrix} \quad (\text{B2}),$$

$$\boldsymbol{\sigma} = [\sigma_x, \sigma_x, \sigma_x, \tau_{xy}, \tau_{yz}, \tau_{zx}]^T \quad (\text{B3}),$$

where \mathbf{L} is the differential operator on stress tensor, $\boldsymbol{\sigma}$ is the stress tensor in the vector form, ρ_b is the bulk density, \mathbf{g} is the gravity acceleration vector, and $\dot{\mathbf{u}}$ is the acceleration vector.

The bulk density (ρ_b) is calculated based on the sediment grain density (ρ_s), the pore fluid density (ρ_f), and the porosity (n):

$$\rho_b = (1 - n)\rho_s + n\rho_f \quad (\text{B4}).$$

2) Fluid flow equations

The sediment is assumed to be fully saturated with a single fluid. The equation governing the flow of the pore fluid is (Rockfield, 2017):

$$\text{div} \left(\frac{k(n)}{\mu_f} (\nabla p_f - \rho_f \mathbf{g}) \right) = \left(\frac{n}{K_f} + \frac{\alpha(n)-n}{K_s} \right) \left(\frac{\partial p_f}{\partial t} \right) - \frac{\alpha}{1-n} \frac{\partial n}{\partial t} \quad (\text{B5}),$$

$$\alpha = 1 - \frac{K_A}{K_s} \quad (\text{B6}).$$

where div is the divergence operator, k is the intrinsic permeability and assumed to be a function of porosity, K_f is the bulk modulus of the pore fluid, K_s is the bulk modulus of the solid matrix, μ_f is the viscosity of the pore fluid, α is the Biot coefficient and is assumed to depend on the ratio of the bulk moduli of the rock matrix (K_A) and of rock grains (Eq. 6). In this paper, $\mu_f = 0.001 \text{ pa} \cdot \text{s}$, $K_f = 2.013 \times 10^9 \text{ Pa}$, and $K_s = 2 \times 10^{10} \text{ Pa}$.

The relationship between the effective stress, total stress, and the pore fluid pressure is:

$$\boldsymbol{\sigma} = \boldsymbol{\sigma}' - \alpha \mathbf{m} p_f \quad (\text{B7}),$$

$$\mathbf{m}^T = [1, 1, 1, 0, 0, 0] \quad (\text{B8}).$$

3) Numerical discretization

In our finite element model, the displacement (\mathbf{u}) and pore water pressure (p_f) are unknowns. The value of these variables within each element is interpolated from their values at the element nodes (Lewis & Schrefler, 1998):

$$\mathbf{u} = \mathbf{N}_u \bar{\mathbf{u}} \quad (\text{B9}),$$

$$p_f = \mathbf{N}_f \bar{p}_l \quad (\text{B10}).$$

where $\bar{\mathbf{u}}$ is the vector of nodal displacement, and \bar{p}_l is the vector of nodal pore pressures. \mathbf{N}_u is the matrix of interpolation (shape) functions for displacement, and \mathbf{N}_f is the matrix of interpolation (shape) functions for the pore pressure.

Similarly, the strain rate vector (\mathbf{D}) within an element may be calculated from the nodal values of the velocity vector ($\bar{\mathbf{v}}$) through the strain operator (\mathbf{B}) (Lewis & Schrefler, 1998):

$$\mathbf{D} = \mathbf{B} \bar{\mathbf{v}} \quad (\text{B11}),$$

$$\mathbf{B} = \mathbf{L} \mathbf{N}_u \quad (\text{B12}),$$

$$B_i^T = \begin{pmatrix} \frac{\partial N_{ui}}{\partial x_1} & 0 & 0 & 0 & \frac{\partial N_{ui}}{\partial x_3} & \frac{\partial N_{ui}}{\partial x_2} \\ 0 & \frac{\partial N_{ui}}{\partial x_2} & 0 & \frac{\partial N_{ui}}{\partial x_3} & 0 & \frac{\partial N_{ui}}{\partial x_1} \\ 0 & 0 & \frac{\partial N_{ui}}{\partial x_3} & \frac{\partial N_{ui}}{\partial x_2} & \frac{\partial N_{ui}}{\partial x_1} & 0 \end{pmatrix} \quad (\text{B13}).$$

We use the Galerkin method (Zienkiewicz *et al.*, 1990) to derive the discretized form of the governing equations (Lewis & Schrefler, 1998; Rockfield, 2017):

$$\int_{\Omega} \mathbf{B}^T \boldsymbol{\sigma}' d\Omega - \mathbf{Q} p_f + \mathbf{M} \ddot{\mathbf{u}} = \mathbf{f}^u \quad (\text{B14}),$$

$$\mathbf{H} p_f + \mathbf{Q}^T \frac{\partial \mathbf{u}}{\partial t} + \mathbf{S} \frac{\partial p_f}{\partial t} = \mathbf{f}^p \quad (\text{B15}),$$

where Ω represents the domain of interest, \mathbf{Q} is the coupling matrix, \mathbf{H} is the permeability matrix, \mathbf{M} is the mass matrix, and \mathbf{S} is the compressibility matrix:

$$\mathbf{Q} = \int_{\Omega} \mathbf{B}^T \alpha m N_f \sigma d\Omega \quad (\text{B16}),$$

$$\mathbf{H} = \int_{\Omega} \mathbf{B}_f^T \frac{k}{\mu_f} \mathbf{B}_f d\Omega \quad (\text{B17}),$$

$$\mathbf{S} = \int_{\Omega} \left(\frac{n}{K_f} + \frac{\alpha-n}{K_s} \right) N_f d\Omega \quad (\text{B18}),$$

$$\mathbf{M} = \int_{\Omega} N_u^T [\rho_s(1-n) + n\rho_f] N_u d\Omega \quad (21).$$

$\int_{\Omega} \mathbf{B}^T \boldsymbol{\sigma}' d\Omega$ represents the internal force.

\mathbf{f}^u is the external load factor:

$$\mathbf{f}^u = \int_{\Omega} N_u^T [\rho_s(1-n) + n\rho_f] N_u d\Omega + \int_{\Gamma} N_u^T \bar{t} d\Gamma \quad (\text{B19}).$$

\mathbf{f}^p is the flow vector:

$$\mathbf{f}^p = \int_{\Omega} (\nabla N_f)^T \frac{k}{\mu_f} \rho_f g d\Omega + \int_{\Omega} N_f^T \alpha m^T \dot{\epsilon} d\Omega - \int_{\Gamma} N_f^T w^{*T} n d\Gamma \quad (\text{B20}).$$

where w^* is a weighting function, and Γ represents the the boundary of the studied domain.

3.8 Appendix C: Deconvolution of overpressure components

The overpressure components are calculated incrementally using the effective stress path and total stress path from geomechanical model. I illustrate a big increment of stress (from a0 to a1) in the example below (Figure 3.15) to visualize the different components clearly. The actual calculation in is based on a much smaller incremental of stress ($\Delta q < 1 \text{MPa}$) to ensure accuracy. Despite the difference in the increment of stress, the fundamental calculation concept is the same.

The increase of overpressure is the combined result of mean-induced overpressure, shear-induced overpressure, and fluid drainage:

$$\Delta\sigma_m + \Delta u_e^q - \Delta u_e^{diss.} = \Delta u_e \quad (C1)$$

where $\Delta\sigma_m$ is the increase of total mean stress, Δu_e^q is overpressure generation due to the increase deviatoric stress, $\Delta u_e^{diss.}$ is the decrease of overpressure due to fluid drainage, and Δu_e is the ultimate resultant overpressure.

As the particle is loaded from a0 to a1, the reduced total stress path ($\sigma_m - u_h$; green line, Figure 3.15a) deviates away from the effective stress path (blue line, Figure 3.15a). The horizontal distance between the effective stress path and the reduced total stress path is the increase of overpressure (Δu_e) (Figure 3.15a). The mean-stress-induced overpressure (Δu_e^m) equals the increase of total mean stress ($\Delta\sigma_m$), which is the increase of reduced total stress from a0 to a1 along total stress path (Figure 3.15a). The shear induced overpressure is estimated by calculating the difference of mean effective stress along the iso-porosity curve (grey arc in Figure 3.15a) with respect to the change of deviatoric stress from initial a_{q0} to $a_1(\sigma'_m)$ (u_e^q , Figure 3.15a). Substituting the Δu_e , $\Delta\sigma_m$, and Δu_e^q in equation C1, $\Delta u_e^{diss.}$ can be obtained as well. The resultant porosity loss due to drainage from a0 to a1 is illustrated in Figure 3.15b.

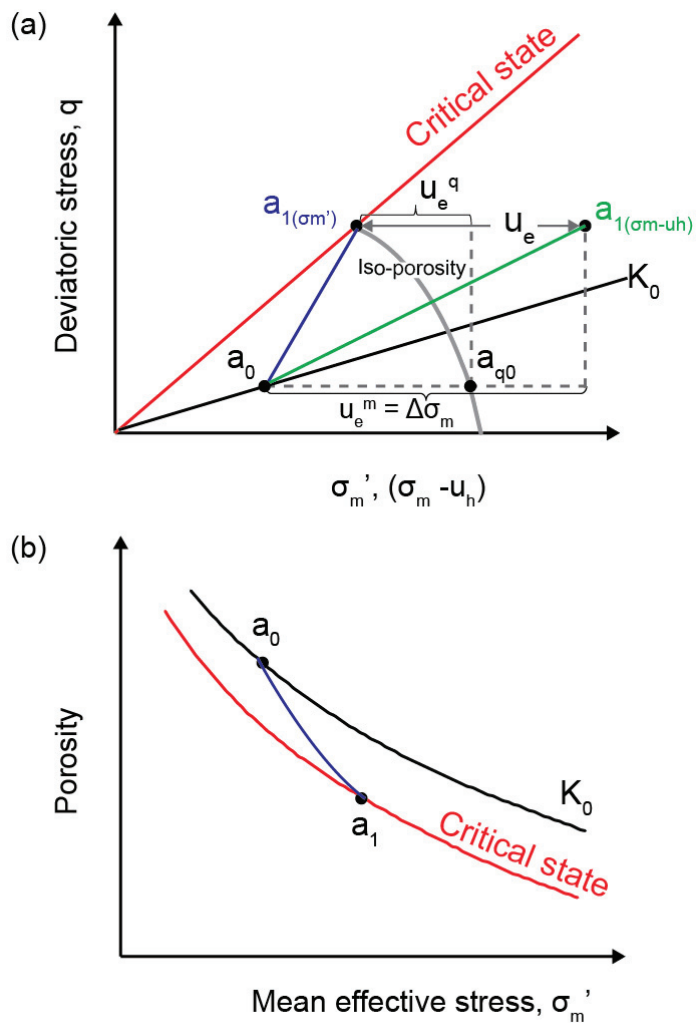


Figure 3.15: (a) Stress path from a_0 to a_1 . Blue line: effective stress path. Green line: reduced total stress path (total stress minus hydrostatic pressure). Grey arc: iso-porosity curve. Blue line: uniaxial strain stress path. Red line: critical state stress path. (b) The corresponding compression path due to drainage from a_0 to a_1 . Red line: critical state compression path. Black: K_0 compression path.

REFERENCES

- Bangs, N.L.B., Moore, G.F., Gulick, S.P.S., Pangborn, E.M., Tobin, H.J., Kuramoto, S., and Taira, A., 2009, Broad, weak regions of the Nankai Megathrust and implications for shallow coseismic slip: *Earth and Planetary Science Letters*, v. 284, 1-2, p. 44–49, doi: 10.1016/j.epsl.2009.04.026.
- Becker, K., Fisher, A.T., and Davis, E.E., editors, 1997, The CORK experiment in Hole 949C: long-term observations of pressure and temperature in the Barbados accretionary prism, *Ocean Drilling Program, Volume 156*, 247-252.
- Beeler, N.M., Simpson, R.W., Hickman, S.H., and Lockner, D.A., 2000, Pore fluid pressure, apparent friction, and Coulomb failure: *Journal of Geophysical Research: Solid Earth*, v. 105, B11, p. 533–542.
- Casey, B., Germaine, J.T., Flemings, P.B., and Fahy, B.P., 2015, Estimating horizontal stresses for mudrocks under one-dimensional compression: *Marine and Petroleum Geology*, v. 65, p. 178–186, doi: 10.1016/j.marpetgeo.2015.02.001.
- Couzens-Schultz, B.A., and Azbel, K., 2014, Predicting pore pressure in active fold–thrust systems: An empirical model for the deepwater Sabah foldbelt: *Journal of Structural Geology*, v. 69, p. 465–480, doi: 10.1016/j.jsg.2014.07.013.
- Crook, A.J.L., Owen, D.R.J., Willson, S.M., and Yu, J.G., 2006, Benchmarks for the evolution of shear localisation with large relative sliding in frictional materials: *Computer methods in applied mechanics and engineering*, v. 195, 37-40, p. 4991–5010, doi: 10.1016/j.cma.2005.11.016.
- Crook, A.J.L., Willson, S.M., Yu, J.G., and Owen, D.R.J., 2006, Predictive modelling of structure evolution in sandbox experiments: *Journal of Structural Geology*, v. 28, no. 5, p. 729–744, doi: 10.1016/j.jsg.2006.02.002.
- Dahlen, F.A., 1990, Critical Taper Model Of Fold-And-Thrust Belts And Accretionary Wedges: *Annual Review of Earth and Planetary Sciences*, v. 18, no. 1, p. 55–99, doi: 10.1146/annurev.earth.18.1.55.
- Dahlen, F.A., Suppe, J., and Davis, D., 1984, Mechanics of fold-and-thrust belts and accretionary wedges: Cohesive Coulomb Theory: *Journal of Geophysical Research: Solid Earth*, v. 89, B12, p. 10087–10101, doi: 10.1029/JB089iB12p10087.

- Davis, D., Suppe, J., and Dahlen, F.A., 1983, Mechanics of fold-and-thrust belts and accretionary wedges: *Journal of Geophysical Research*, v. 88, B2, p. 1153, doi: 10.1029/JB088iB02p01153.
- Dimitrov, L.I., 2002, Mud volcanoes—the most important pathway for degassing deeply buried sediments: *Earth-Science Reviews*, v. 59, 1-4, p. 49–76, doi: 10.1016/S0012-8252(02)00069-7.
- Dixon, T.H., and Moore, C., editors, 2007, *The Seismogenic Zone of Subduction Thrust Faults*: New York Chichester, West Sussex, Columbia University Press.
- Flemings, P.B., and Saffer, D.M., 2018, Pressure and Stress Prediction in the Nankai Accretionary Prism: A Critical State Soil Mechanics Porosity-Based Approach: *Journal of Geophysical Research: Solid Earth*, v. 123, no. 2, p. 1089–1115, doi: 10.1002/2017JB015025.
- Gao, B., Flemings, P.B., Nikolinakou, M.A., Saffer, D.M., and Heidari, M., 2018, Mechanics of Fold - and - Thrust Belts Based on Geomechanical Modeling: *Journal of Geophysical Research: Solid Earth*.
- Hardebeck, J.L., and Loveless, J.P., 2018, Creeping subduction zones are weaker than locked subduction zones: *Nature Geoscience*, v. 11, no. 1, p. 60.
- Hauser, M.R., Couzens-Schultz, B.A., and Chan, A.W., 2014, Estimating the influence of stress state on compaction behavior: *Geophysics*, v. 79, no. 6, D389-D398, doi: 10.1190/geo2014-0089.1.
- Hirono, T., Tsuda, K., Tanikawa, W., Ampuero, J.-P., Shibasaki, B., Kinoshita, M., and Mori, J.J., 2016, Near-trench slip potential of megaquakes evaluated from fault properties and conditions: *Scientific reports*, v. 6, p. 28184, doi: 10.1038/srep28184.
- Hubbert, M.K., and Rubey, W.W., 1959, Mechanics of fluid-filled porous solids and its application to overthrust faulting: *Geological Society of America Bulletin*, v. 70, p. 115–166.
- Kim, S., and Hosseini, S.A., 2014, Geological CO₂ storage: Incorporation of pore-pressure/stress coupling and thermal effects to determine maximum sustainable pressure limit: *Energy Procedia*, v. 63, p. 3339–3346, doi: 10.1016/j.egypro.2014.11.362.
- Kimura, G., Hina, S., Hamada, Y., Kameda, J., Tsuji, T., Kinoshita, M., and Yamaguchi, A., 2012, Runaway slip to the trench due to rupture of highly pressurized

- megathrust beneath the middle trench slope: The tsunamigenesis of the 2011 Tohoku earthquake off the east coast of northern Japan: *Earth and Planetary Science Letters*, 339-340, p. 32–45, doi: 10.1016/j.epsl.2012.04.002.
- Kitajima, H., Saffer, D., Sone, H., Tobin, H., and Hirose, T., 2017, In Situ Stress and Pore Pressure in the Deep Interior of the Nankai Accretionary Prism, Integrated Ocean Drilling Program Site C0002: *Geophysical Research Letters*, v. 44, no. 19, p. 9644–9652, doi: 10.1002/2017GL075127.
- Kitajima, H., and Saffer, D.M., 2012, Elevated pore pressure and anomalously low stress in regions of low frequency earthquakes along the Nankai Trough subduction megathrust: *Geophysical Research Letters*, v. 39, no. 23, n/a-n/a, doi: 10.1029/2012GL053793.
- Lallemand, S.E., Schnürle, P., and Malavieille, J., 1994, Coulomb theory applied to accretionary and nonaccretionary wedges: Possible causes for tectonic erosion and/or frontal accretion: *Journal of Geophysical Research: Solid Earth* (1978–2012), v. 99, p. 12033–12055.
- Lewis, R.W., and Schrefler, B.A., 1998, *The finite element method in the static and dynamic deformation and consolidation of porous media*, Wiley Chichester, Volume 2.
- Moore, J.C., and Vrolijk, P., 1992, Fluids in accretionary prisms: *Reviews of Geophysics*, v. 30, no. 2, p. 113–135.
- Nemcok, M., Schamel, S., and Gayer, R., 2009, *Thrustbelts: Structural architecture, thermal regimes and petroleum systems*, Cambridge University Press.
- Neuzil, C.E., 1995, Abnormal pressures as hydrodynamic phenomena: *American Journal of Science*, v. 295, no. 6, p. 742–786.
- Obara, K., and Kato, A., 2016, Connecting slow earthquakes to huge earthquakes: *Science* (New York, N.Y.), v. 353, no. 6296, p. 253–257, doi: 10.1126/science.aaf1512.
- Obradors-Prats, J., Rouainia, M., Aplin, A.C., and Crook, A.J.L., 2017, Hydromechanical Modeling of Stress, Pore Pressure, and Porosity Evolution in Fold-and-Thrust Belt Systems: *Journal of Geophysical Research: Solid Earth*, v. 122, no. 11, p. 9383–9403, doi: 10.1002/2017JB014074.

- Peng, Z., and Gomberg, J., 2010, An integrated perspective of the continuum between earthquakes and slow-slip phenomena: *Nature Geoscience*, v. 3, no. 9, p. 599–607, doi: 10.1038/ngeo940.
- Reece, J.S., Flemings, P.B., and Germaine, J.T., editors, 2013, Data report: Permeability, compressibility, and microstructure of resedimented mudstone from IODP Expedition 322, Site C0011, Volume 322, 1-26.
- Rockfield, 2017, *Elfen Explicit Manual, Version 4.10*: Swansea, UK, Rockfield Software.
- Romano, F., Trasatti, E., Lorito, S., Piromallo, C., Piatanesi, A., Ito, Y., Zhao, D., Hirata, K., Lanucara, P., and Cocco, M., 2014, Structural control on the Tohoku earthquake rupture process investigated by 3D FEM, tsunami and geodetic data: *Scientific reports*, v. 4, p. 5631, doi: 10.1038/srep05631.
- Roscoe, K.H., Schofield, A., and Wroth, C.P., 1958, On the yielding of soils: *Geotechnique*, v. 8, p. 22–53.
- Rowe, K.T., Screaton, E.J., and Ge, S., 2012, Coupled fluid flow and deformation modeling of the frontal thrust region of the Kumano Basin transect, Japan: Implications for fluid pressures and decollement downstepping: *Geochemistry, Geophysics, Geosystems*, v. 13, no. 3, n/a-n/a, doi: 10.1029/2011GC003861.
- Saffer, D.M., and Bekins, B.A., 2002, Hydrologic controls on the morphology and mechanics of accretionary wedges: *Geology*, v. 30, no. 3, p. 271, doi: 10.1130/0091-7613(2002)030<0271:HCOTMA>2.0.CO;2.
- Saffer, D.M., and Bekins, B.A., 2006, An evaluation of factors influencing pore pressure in accretionary complexes: Implications for taper angle and wedge mechanics: *Journal of Geophysical Research*, v. 111, B4, p. 104, doi: 10.1029/2005JB003990.
- Saffer, D.M., and Tobin, H.J., 2011, Hydrogeology and Mechanics of Subduction Zone Forearcs: Fluid Flow and Pore Pressure: *Annual Review of Earth and Planetary Sciences*, v. 39, no. 1, p. 157–186, doi: 10.1146/annurev-earth-040610-133408.
- Saffer, D.M., and Wallace, L.M., 2015, The frictional, hydrologic, metamorphic and thermal habitat of shallow slow earthquakes: *Nature Geoscience*, v. 8, no. 8, p. 594–600, doi: 10.1038/ngeo2490.
- Sawai, M., Niemeijer, A.R., Plümper, O., Hirose, T., and Spiers, C.J., 2016, Nucleation of frictional instability caused by fluid pressurization in subducted blueschist:

- Geophysical Research Letters, v. 43, no. 6, p. 2543–2551, doi: 10.1002/2015GL067569.
- Schofield, A., and Wroth, P., 1968, Critical state soil mechanics.
- Scholz, C.H., 2002, The Mechanics of Earthquakes and Faulting.
- Screaton, E., Saffer, D., Henry, P., and Hunze, S., 2002, Porosity loss within the underthrust sediments of the Nankai accretionary complex: Implications for overpressures: *Geology*, v. 30, no. 1, p. 19, doi: 10.1130/0091-7613(2002)030<0019:PLWTUS>2.0.CO;2.
- Tonegawa, T., Araki, E., Kimura, T., Nakamura, T., Nakano, M., and Suzuki, K., 2017, Sporadic low-velocity volumes spatially correlate with shallow very low frequency earthquake clusters: *Nature communications*, v. 8, no. 1, p. 2048, doi: 10.1038/s41467-017-02276-8.
- Tsuji, T., Kamei, R., and Pratt, R.G., 2014, Pore pressure distribution of a mega-splay fault system in the Nankai Trough subduction zone: Insight into up-dip extent of the seismogenic zone: *Earth and Planetary Science Letters*, v. 396, p. 165–178, doi: 10.1016/j.epsl.2014.04.011.
- Tsuji, T., Tokuyama, H., Costa Pisani, P., and Moore, G., 2008, Effective stress and pore pressure in the Nankai accretionary prism off the Muroto Peninsula, southwestern Japan: *Journal of Geophysical Research: Solid Earth (1978–2012)*, v. 113, p. 1–19, doi: 10.1029/2007JB005002.
- Wood, D.M., 1990, Soil behaviour and critical state soil mechanics, Cambridge University Press.
- Yang, Y., and Aplin, A.C., 2010, A permeability–porosity relationship for mudstones: *Marine and Petroleum Geology*, v. 27, no. 8, p. 1692–1697, doi: 10.1016/j.marpetgeo.2009.07.001.
- Zienkiewicz, O.C., Chan, A.H.C., Pastor, M., Paul, D.K., and Shiomi, T., 1990, Static and dynamic behaviour of soils: a rational approach to quantitative solutions. I. Fully saturated problems: *Proc. R. Soc. Lond. A*, v. 429, no. 1877, p. 285–309.
- Zoback, M.D., 2010, Reservoir geomechanics, Cambridge University Press., p. 340-369

Chapter 4: The role of overpressure on décollement friction resistance in frontal subduction zone

ABSTRACT

Shallow slip events are closely linked to the mechanical and fluid flow behaviors in subduction zones; however, the fundamental mechanism of the development of stress and pore pressure conditions are not well understood. I use a forward geomechanical model to simulate the stress and pore pressure evolution as the incoming sediment is incorporated into the accretionary wedge. I find that the lateral tectonic loading causes rapid change of stress and generates great overpressure near trench. The sediment near the trench plays a key role in generating high overpressure toward the inner wedge and it weakens the décollement all the way to the trench. The rapid increase of overpressure reduces the normal effective stress at the frontal wedge and thus decreases the frictional resistance at the décollement. The frictional resistance at the décollement is decreased to the lowest at about 5km landward distance to the trench. Both the increase of mean stress and shear stress contribute to overpressure generation. Low sediment permeability and high plate convergence rate promote the generation of overpressure, lower the vertical effective stress, and expand the low frictional resistance area.

4.1 INTRODUCTION

The outer accretionary wedge (<10km depth) is generally observed to be aseismic; frictional sliding occurs with limited seismicity activity, which is commonly referred to as creep (Dixon & Moore, 2007). In fact, modern high-resolution geodetic networks and seismological observations record various modes of slip in the outer accretionary wedge accompanied by a wide spectrum of seismic events, including low frequency earthquake (LFE), very low frequency event (VLF), and tremors (Obara & Kato, 2016; Araki *et al.*, 2017; Wallace *et al.*, 2017). These slip and seismic events suggest that the stress states and frictional behaviors in the outer accretionary wedge are heterogeneous (Saffer & Wallace, 2015). It is important to investigate the variation of stress and frictional resistance at the plate boundary of the frontal accretionary wedge because it greatly impact the sliding stability (stable versus unstable), slip distance, and the amount of seismic energy. The variation of the frictional resistance along the décollement can be impacted by diagenesis (Hacker, 1997; Moore & Saffer, 2001), slip rate (Dieterich, 1978), geometry variation (e.g. seamount), and overpressure (Saffer & Wallace, 2015).

There is very limited understanding of the stress and pressure in the hanging-wall sediment. Rapid tectonic loading and low permeable unconsolidated sediment could generate significant overpressure and alter fault stability along the décollement (Saffer & Tobin, 2011; Han *et al.*, 2017). Here, I apply geomechanical model to reveal the physical insights about the mechanical and fluid flow behaviors in accretionary wedge system under lateral tectonic loading. I investigate the following fundamental questions: (1) what is the spatial variation of the pore pressure and stress states of the hanging wall and how does it evolve? (2) how does pore pressure and stress couple between the hanging wall and footwall? and (3) what is the variation of frictional resistance at the décollement (plate

boundary).

4.2 APPROACH AND RESULTS

4.2.1 Model set-up and material properties

I use a large-strain geomechanical model (Figure 4.1a) to study the evolution of stress and pore pressure in accretionary wedges. The accreted hanging-wall sediment and the subducted footwall sediment are represented by two initially horizontal layers that are 3km and 2km thick, respectively. The décollement between them is simulated with a frictional contact that has a friction coefficient (μ_b) equal to 0.2 ($\phi'_s = 11^\circ$). The sediment is modeled as poro-elastoplastic using the critical state formulation SR3 (Crook *et al.*, 2006). The applied material in this study has equivalent internal friction coefficient (μ_s) of 0.44 ($\phi'_s = 24^\circ$). Sediment porosity is a function of both mean effective stress (σ'_m) and deviatoric stress (q), where:

$$\sigma'_m = \frac{\sigma'_1 + \sigma'_2 + \sigma'_3}{3} \quad (1),$$

$$q = \sqrt{\frac{(\sigma'_1 - \sigma'_2)^2 + (\sigma'_2 - \sigma'_3)^2 + (\sigma'_3 - \sigma'_1)^2}{2}} \quad (2).$$

Sediment permeability is a function of porosity and is updated continuously as porosity changes. The porosity versus permeability relationship is shown in Figure 3.13b (“med. k”). The sediment has a coefficient of consolidation equal to that observed experimentally in Gulf of Mexico mudrock (Casey *et al.*, 2013; Nikolinakou *et al.*, 2018) (Figure 3.13d). To simulate the lateral deformation in an accretionary wedge, a wall is displaced at a constant rate (5mm./yr. in base case) on the left edge of the model above the décollement (Figure 4.1a).

More detailed information about the material parameters and modeling techniques

are described in the Chapter 3.

4.2.2 Base model results

After 85 km of displacement, the upper surface develops a constant slope of 3.8° ; the break in slope marks the ‘trench’, which is located at 0 km (Figure 4.1b, e, f). The displacement load deforms the sediment and generates overpressure throughout the wedge (Figure 4.1b, c, d). On the far right (-10 to -20 km, Figure 4.1b), pore pressure is hydrostatic because the sediment has not undertaken the loading from the wedge yet. In the frontal part of the wedge (between 20 and -10 km), the overpressure is greater within the hanging wall than in the footwall (Figure 4.1b, d). This is strikingly illustrated with the parameter λ^* (section 3.3.1), which records how close the pore pressure is to overburden stress (green, Figure 4.1d). Along profile #1 (Figure 4.1b) near trench, the maximum overpressure ratio in hanging-wall is 0.45 ($\lambda^* = 0.45$), which means the pore pressure is 45% of the distance between the hydrostatic pressure and the overburden stress (Figure 4.1d). In contrast, beneath the décollement, pressure drops and (λ^*) decreases from 0.35 to 0.2 with depth (Figure 4.1d). In the interior of the wedge, along profile #2, the overpressure increases with depth and becomes almost constant in the footwall (Figure 4.1b, c). Inside the wedge, the overpressure contours are parallel to the seafloor; because the permeability is assumed isotropic, this drives flow upward to the seafloor. In contrast, in the footwall, overpressure contours are sub-vertical and flow is driven laterally away from the wedge. At the décollement, there is downward flow in the frontal part of the wedge where the hanging wall has a higher pressure than the footwall; in contrast in the interior there is upward drainage at the décollement as flow occurs from the more pressured footwall upward into the hanging wall.

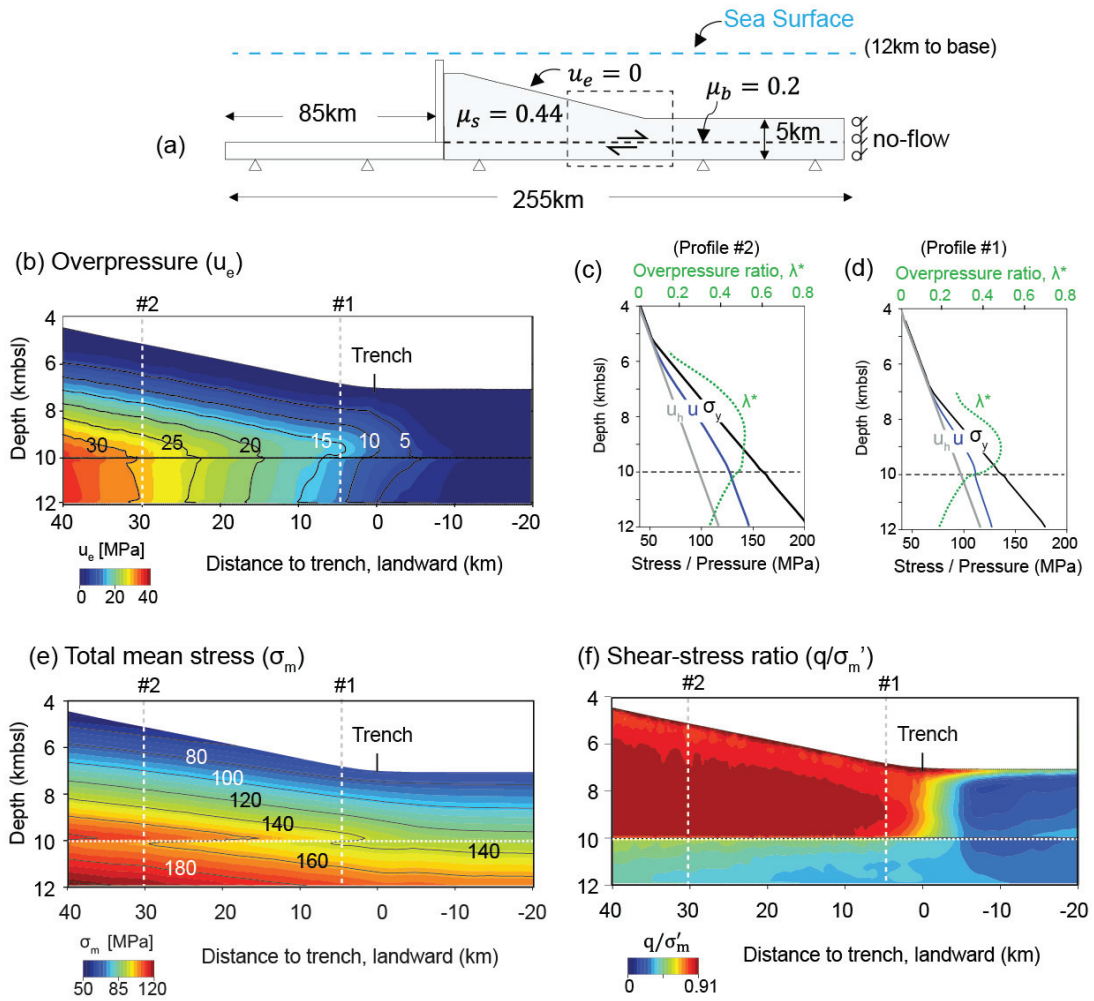


Figure 4.1: (a) Model set-up and boundary conditions. The sediments were initially horizontally deposited and then displaced 85 km to the right. Sea level is 12 km above the model base. The region inside the dashed box is expanded in b, e, and f. (b) Overpressure (u_e) is equal to the total pore pressure (u) less the hydrostatic pressure ($u_e = u - u_h$). (c) and (d): Pressure & stress profiles for location #2 and #1 shown in (b). The hydrostatic pressure (u_h), the pore pressure (u), the overburden stress (σ_y), and the overpressure ratio ($\lambda^* = \frac{u_e}{\sigma_v - u_h}$) are displayed. (e) Total mean stress (σ_m) distribution. (f) Shear-stress ratio (q/σ'_m).

Shortening in the wedge increases the total mean stress (Figure 4.1e) and the ratio of deviatoric stress to mean effective stress (Figure 4.1f). In the footwall, the total mean stress (σ_m) increases approximately linearly from near the trench to the interior of the wedge. This is largely caused by the linear increase in overburden that occurs toward the interior. The mean stress increases abruptly upwards across the décollement. This is because within the wedge, the horizontal and intermediate stress are greater than the overburden in contrast to below the décollement where the horizontal and intermediate stress are less than the overburden. In normal uniaxial strain compression condition (e.g. far away from the wedge), for geostatic ratio ($K_0 = \frac{\sigma'_x}{\sigma'_y}$) equals 0.8, the ratio of deviatoric stress (q) to mean effective stress (σ'_m) is 0.23. Within the wedge, the shear stress ratio (q/σ'_m) is approximately 0.9. The material applied in this study has critical state value (η_{cs}) of 0.91, representing an equivalent sediment internal friction angle of $\phi'_s = 24^\circ$ ($\eta_{cs} = \frac{6\sin\phi'_s}{3-\sin\phi'_s}$). This is the stress ratio at shear failure and indicates that all of the hanging wall is failing. In contrast, beneath the wedge, the shear stress ratio is ~ 0.35 . In this zone, the shear stress ratio is slightly greater than that in the far-field because some shear stress is transmitted into the footwall through the frictional décollement. Near the trench, the shear stress ratio varied rapidly within short distance (-5km to 5km) from uniaxial strain condition to critical state (blue to yellow to red, Figure 4.1f).

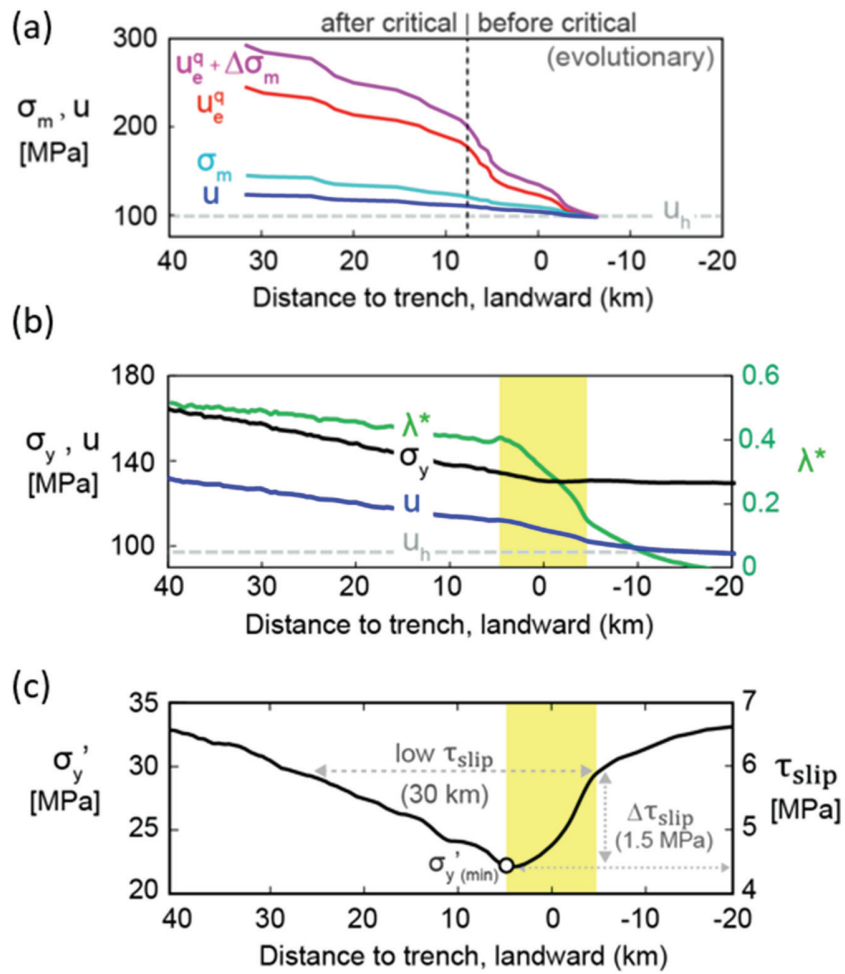


Figure 4.2: (a) The evolution of stress and pressure in a sediment element immediately above the decollement. Dark blue, cyan, red, and pink lines represent the pore pressure (u), total mean stress (σ_m), shear-induced overpressure (u_e^q), and total induced-overpressure ($u_e^q + \Delta\sigma_m$), respectively. (b) The variation of stress and pressure immediately above the décollement at the end of the simulation. Dashed grey: hydrostatic pressure (u_h). Blue: pore pressure (u). Black: overburden stress (σ_y). Green: overpressure ratio (λ^*). (c) The distribution of vertical effective stress (σ'_y) and the frictional resistance (τ_{slip}) immediately above the decollement at the end of the simulation.

The high overpressure in the wedge near trench is driven by the rapid increase in total mean and shear stress as the sediment is consumed into the wedge. I track the stress and pore pressure of a sediment volume as it passes into the wedge (Figure 4.2a). The tracked sediment was initially located at 7km seaward of trench immediately above the décollement and finally reaches 33km landward of trench. The total induced overpressure (pink, Figure 4.2a) is caused by the sum of the increase of overpressure by mean stress (σ_m) (cyan line, Figure 4.2a) and the increase of overpressure by shear stress (u_e^q) (red line Figure 2a). These two components rise rapidly as the stress condition changes from uniaxial strain to critical state (-7km to 8km, Figure 4.2a) and then moderately thereafter (> 8km, Figure 4.2a). Before sediment reaches critical state, the average increase rate of shear-induced-overpressure (u_e^q) is 41MPa/m.y. and the average increase rate of mean-induced overpressure (u_e^m) is 12.5MPa/m.y. (t1 to t2, Figure 3.10c). After the sediment reach critical stress state, the increase rate of the shear-induced overpressure (u_e^q) and mean-induced overpressure drops by 64% and 56% respectively (t2-t3, Figure 3.10c). As a result, the increase rate of the resultant overpressure (u_e , Figure 4.2a) after the sediment reach critical state drops by 61% compared to before, reflecting a much slower overpressure increase as the sediment incorporated into the inner wedge. The difference between the total induced overpressure (pink, Figure 4.2a) and the actual resultant overpressure (dark blue, Figure 2a) records the pore pressure dissipation.

High overpressure in the hanging-wall significantly decreases the vertical effective stress, which decreases the basal frictional resistance. I show the variation of stress and pore pressure immediately above the décollement. From 5km seaward of trench to 5km landward of trench (Figure 4.2b, yellow region), the overpressure ($u - u_h$) increase from 2MPa to 15MPa and the overpressure ratio increases from 0.15 to 0.41 (Figure 4.2b).

Because the pore pressure increases much faster than the overburden stress near trench, the vertical effective stress decreases. At 5km landward of the trench, the vertical effective stress at the décollement decreases from 28MPa to 22MPa (Figure 4.2c). Further into the wedge, the vertical effective stress along the décollement gradually increases. The frictional resistance (τ_{slip}) for the sediment to slip along the décollement is proportional to the vertical effective stress (μ_b is assumed constant: 0.2):

$$\tau_{\text{slip}} = \mu_b(\sigma_y - u) = \mu_b\sigma'_y \quad (3).$$

τ_{slip} decreases 1.5 MPa ($\Delta\tau_{\text{slip}}$) from ~ 6 MPa at 5km seaward of trench to 4.5MPa at 5km distance landward of the trench (yellow zone, Figure 4.2c). Further into the wedge, τ_{slip} increases back to ~ 6 MPa at 25 km landward of trench. The low τ_{slip} area caused by the high overpressure is 30 km wide (Figure 4.2c).

4.3 THE IMPACT OF PERMEABILITY AND CONVERGENCE RATE ON STRESS

Low permeable mudrock and high convergence rate expand the region of weak décollement zone and further decrease the frictional resistance at the décollement (Figure 4.3). I test the sensitivity of the mudrock permeability by comparing the base case (“med.k”) with another two cases: one is 10 times higher permeability (“high k”) than that of the base case and another is 10 times lower permeability (“low k”) than the base case (Figure 3.13b). I choose 5km in front of the wedge as a reference location to measure the range of the overpressure-weakened décollement (Figure 4.3). As the mudrock permeability decreases, the vertical effective stress decreases and the range of the low-frictional-resistance zone increase from 14km to 37km (Figure 4.3a). The frictional resistance at the décollement (τ_{slip}) is reduced to as low as 3MPa in the low permeability case with the maximum frictional resistant drop $\Delta\tau_{\text{slip}}$ of 2.5MPa. On the contrary, the high permeable rock case shows a much lower effective stress reduction near trench and

quicker vertical effective stress increase at inner wedge (blue, Figure 4.3a). In the high permeability case, the reduction of vertical effective stress region is only 14km wide and the maximum frictional resistance drop $\Delta\tau_{\text{slip}}$ is only 0.5MPa. High plate convergence rate has similar impact as the low permeability case. As the convergence rate increases from 1mm./year (“slow”, Figure 4.3b) to 10mm./yr. (“fast”, Figure 4.3b), the range of overpressure-weakened décollement increase from 16km to 41km. The minimal basal friction resistance τ_{slip} decreases from 6MPa to 3.5MPa as the convergence rate increases (“slow” vs. “fast”, Figure 4.3b).

4.4 DISCUSSION

The sediment properties and the loading condition near the trench play a key role in initiating and preserving high overpressure in accretionary wedge system. Under the quick increase of total lateral stresses, the overpressure increases rapidly from 5km seaward of trench to 5km landward of the trench. This rapid-pressure-increases zone (Figure 4.2b) near the trench largely controls the variation of basal frictional resistance toward the inner wedge. High overpressure also causes the decrease of vertical effective stress and decrease the basal friction resistance. When the convergence rate is increased or the permeability is decreased, the vertical effective stress is furthered reduced and results in even lower basal frictional resistance.

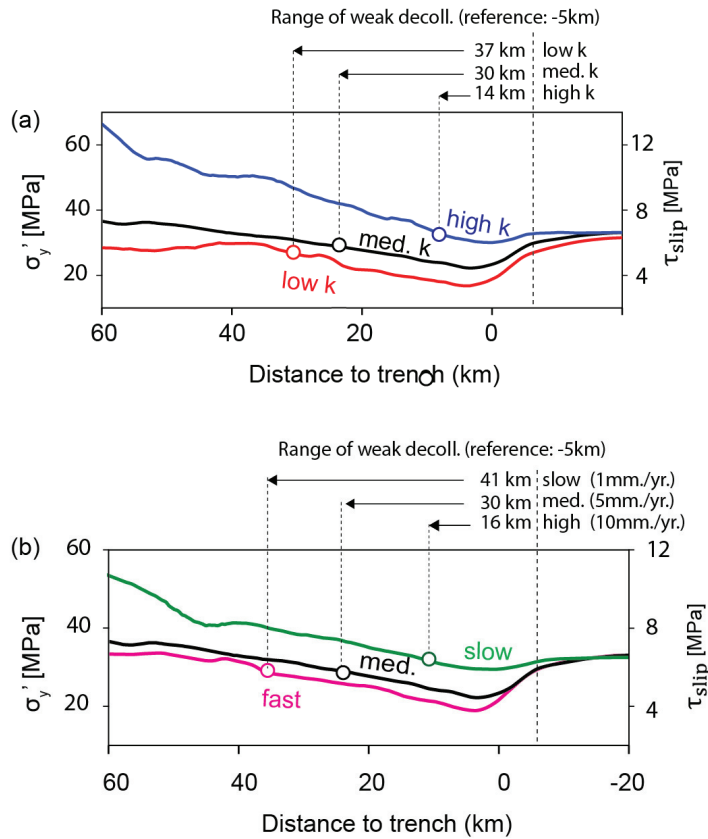


Figure 4.3: (a) Impact of mudrock permeability on the vertical effective stress and basal frictional resistance along décollement. The high permeability case (“high k”) and low permeability case (“low k”) has 10 times higher and 10 times lower permeability than that of the medium permeability case (“med.k”) with respect to the same porosity (Figure 3.13b). The circles mark the location where the vertical effective stress increases back to the initial value at 5km seaward of the trench. (b) Impact of convergence rate on the vertical effective stress and basal frictional resistance. The “slow”, “med.”, and “fast” represent displacement rate of 1mm./yr., 5mm./yr., and 10mm./yr., respectively.

The lateral tectonic displacement increases both total mean stress and deviatoric stress, which drive the increase of overpressure. The mean-stress-induced overpressure (u_e^m) and the shear-induced overpressure (u_e^q) increase much faster before the sediment reach critical state than after (Figure 4.2a). In addition, before the sediment reach critical state, the deviatoric stress plays a dominant role in overpressure generation (pink vs. cyan, Figure 4.2a). After the critical state, the increase rates of mean-induced overpressure and shear-induced overpressure are more close to each other.

High overpressure near the trench reduces the possibility of initiating big earthquakes at shallow depths. The occurrence of high-magnitude earthquake requires sudden release of significant amount of elastic energy. Because sediment with high pore pressure has very low frictional resistance ($<10\text{MPa}$, Figure 4.3) and low elastic properties, it is not likely to host big earthquakes and radiate large amount of energy within short time. As a result, the highly overpressured accretionary wedges are more prone to have aseismic slip. The overpressure may also deepen the up-dip limit depth of the seismic zone because the effective stress may remain low for long distance along the décollement in highly overpressured prisms (Figure 4.3).

4.5 CONCLUSIONS

In summary, I find pore pressure increases significantly as the sediment is incorporated into accretionary wedge. Both shear stress and mean stress contribution to the overpressure generation. The overpressure reduces the normal effective stress and decrease the frictional resistance along the décollement. Low rock permeability and high convergence rate lower the frictional resistance and broaden the area of weak décollement.

REFERENCE

- Araki, E., Saffer, D.M., Kopf, A.J., Wallace, L.M., Kimura, T., Machida, Y., Ide, S., and Davis, E., 2017, Recurring and triggered slow-slip events near the trench at the Nankai Trough subduction megathrust: *Science* (New York, N.Y.), v. 356, no. 6343, p. 1157–1160, doi: 10.1126/science.aan3120.
- Casey, B., Germaine, J.T., Flemings, P.B., Reece, J.S., Gao, B., and Betts, W., 2013, Liquid limit as a predictor of mudrock permeability: *Marine and Petroleum Geology*, v. 44, p. 256–263, doi: 10.1016/j.marpetgeo.2013.04.008.
- Crook, A.J.L., Owen, D.R.J., Willson, S.M., and Yu, J.G., 2006, Benchmarks for the evolution of shear localisation with large relative sliding in frictional materials: *Computer methods in applied mechanics and engineering*, v. 195, 37-40, p. 4991–5010, doi: 10.1016/j.cma.2005.11.016.
- Dieterich, J.H., 1978, Time-dependent friction and the mechanics of stick-slip: *Pure and Applied Geophysics PAGEOPH*, v. 116, 4-5, p. 790–806, doi: 10.1007/BF00876539.
- Dixon, T.H., Jiang, Y., Malservisi, R., McCaffrey, R., Voss, N., Protti, M., and Gonzalez, V., 2014, Earthquake and tsunami forecasts: relation of slow slip events to subsequent earthquake rupture: *Proceedings of the National Academy of Sciences of the United States of America*, v. 111, no. 48, p. 17039–17044, doi: 10.1073/pnas.1412299111.
- Dixon, T.H., and Moore, C., editors, 2007, *The Seismogenic Zone of Subduction Thrust Faults*: New York Chichester, West Sussex, Columbia University Press.
- Hacker, B.R., 1997, Diagenesis and fault valve seismicity of crustal faults: *Journal of Geophysical Research: Solid Earth*, v. 102, B11, p. 24459–24467.
- Han, S., Bangs, N.L., Carbotte, S.M., Saffer, D.M., and Gibson, J.C., 2017, Links between sediment consolidation and Cascadia megathrust slip behaviour: *Nature Geoscience*, v. 10, no. 12, p. 954–959, doi: 10.1038/s41561-017-0007-2.
- Ingebritsen, S.E., and Sanford, W.E., 1999, *Groundwater in geologic processes*, Cambridge University Press.
- Kozdon, J.E., and Dunham, E.M., 2013, Rupture to the Trench: Dynamic Rupture Simulations of the 11 March 2011 Tohoku Earthquake: *Bulletin of the Seismological Society of America*, v. 103, 2B, p. 1275–1289, doi: 10.1785/0120120136.

- Maksymowicz, A., Chadwell, C.D., Ruiz, J., Tréhu, A.M., Contreras-Reyes, E., Weinrebe, W., Díaz-Naveas, J., Gibson, J.C., Lonsdale, P., and Tryon, M.D., 2017, Coseismic seafloor deformation in the trench region during the Mw8.8 Maule megathrust earthquake: Scientific reports, v. 7, p. 45918, doi: 10.1038/srep45918.
- Moore, J.C., and Saffer, D., 2001, Updip limit of the seismogenic zone beneath the accretionary wedge of southwest Japan: An effect of diagenetic to low-grade metamorphic processes and increasing effective stress: *Geology*, v. 29, no. 2, p. 183–186.
- Neuzil, C.E., 1995, Abnormal pressures as hydrodynamic phenomena: *American Journal of Science*, v. 295, no. 6, p. 742–786.
- Nikolinakou, M.A., Heidari, M., Flemings, P.B., and Hudec, M.R., 2018, Geomechanical modeling of pore pressure in evolving salt systems: *Marine and Petroleum Geology*, v. 93, p. 272–286, doi: 10.1016/j.marpetgeo.2018.03.013.
- Obara, K., and Kato, A., 2016, Connecting slow earthquakes to huge earthquakes: *Science (New York, N.Y.)*, v. 353, no. 6296, p. 253–257, doi: 10.1126/science.aaf1512.
- Polet, J., and Kanamori, H., 2000, Shallow subduction zone earthquakes and their tsunamigenic potential: *Geophysical Journal International*, v. 142, no. 3, p. 684–702, doi: 10.1046/j.1365-246x.2000.00205.x.
- Saffer, D.M., and Tobin, H.J., 2011, Hydrogeology and Mechanics of Subduction Zone Forearcs: Fluid Flow and Pore Pressure: *Annual Review of Earth and Planetary Sciences*, v. 39, no. 1, p. 157–186, doi: 10.1146/annurev-earth-040610-133408.
- Saffer, D.M., and Wallace, L.M., 2015, The frictional, hydrologic, metamorphic and thermal habitat of shallow slow earthquakes: *Nature Geoscience*, v. 8, no. 8, p. 594–600, doi: 10.1038/ngeo2490.
- Wallace, L.M., Kaneko, Y., Hreinsdóttir, S., Hamling, I., Peng, Z., Bartlow, N., D’Anastasio, E., and Fry, B., 2017, Large-scale dynamic triggering of shallow slow slip enhanced by overlying sedimentary wedge: *Nature Geoscience*, v. 10, no. 10, p. 765–770, doi: 10.1038/ngeo3021.

Bibliography

- Allaby, M., 2013, *A Dictionary of Geology and Earth Sciences*.
- Araki, E., Saffer, D.M., Kopf, A.J., Wallace, L.M., Kimura, T., Machida, Y., Ide, S., and Davis, E., 2017, Recurring and triggered slow-slip events near the trench at the Nankai Trough subduction megathrust: *Science* (New York, N.Y.), v. 356, no. 6343, p. 1157–1160, doi: 10.1126/science.aan3120.
- Bangs, N.L.B., Moore, G.F., Gulick, S.P.S., Pangborn, E.M., Tobin, H.J., Kuramoto, S., and Taira, A., 2009, Broad, weak regions of the Nankai Megathrust and implications for shallow coseismic slip: *Earth and Planetary Science Letters*, v. 284, 1-2, p. 44–49, doi: 10.1016/j.epsl.2009.04.026.
- Becker, K., Fisher, A.T., and Davis, E.E., editors, 1997, The CORK experiment in Hole 949C: long-term observations of pressure and temperature in the Barbados accretionary prism, *Ocean Drilling Program, Volume 156*, 247-252.
- Beeler, N.M., Simpson, R.W., Hickman, S.H., and Lockner, D.A., 2000, Pore fluid pressure, apparent friction, and Coulomb failure: *Journal of Geophysical Research: Solid Earth*, v. 105, B11, p. 533–542.
- Bekins, B. A., & Dreiss, S. J. (1992). A simplified analysis of parameters controlling dewatering in accretionary prisms. *Earth and Planetary Science Letters*, 109(3-4), 275–287. [https://doi.org/10.1016/0012-821X\(92\)90092-A](https://doi.org/10.1016/0012-821X(92)90092-A)
- Bray, C. J., & Karig, D. E. (1985). Porosity of sediments in accretionary prisms and some implications for dewatering processes. *Journal of Geophysical Research: Solid Earth* (1978–2012), 90, 768–778.
- Casey, B., Germaine, J.T., Flemings, P.B., and Fahy, B.P., 2015, Estimating horizontal stresses for mudrocks under one-dimensional compression: *Marine and Petroleum Geology*, v. 65, p. 178–186, doi: 10.1016/j.marpetgeo.2015.02.001.
- Casey, B., Germaine, J.T., Flemings, P.B., Reece, J.S., Gao, B., and Betts, W., 2013, Liquid limit as a predictor of mudrock permeability: *Marine and Petroleum Geology*, v. 44, p. 256–263, doi: 10.1016/j.marpetgeo.2013.04.008.
- Chapple, W.M., 1978, Mechanics of thin-skinned fold-and-thrust belts: *Geological Society of America Bulletin*, v. 89, no. 8, p. 1189, doi: 10.1130/0016-7606(1978)89<1189:MOTFB>2.0.CO;2.

- Couzens-Schultz, B.A., and Azbel, K., 2014, Predicting pore pressure in active fold–thrust systems: An empirical model for the deepwater Sabah foldbelt: *Journal of Structural Geology*, v. 69, p. 465–480, doi: 10.1016/j.jsg.2014.07.013.
- Crook, A.J.L., Owen, D.R.J., Willson, S.M., and Yu, J.G., 2006, Benchmarks for the evolution of shear localisation with large relative sliding in frictional materials: *Computer methods in applied mechanics and engineering*, v. 195, 37–40, p. 4991–5010, doi: 10.1016/j.cma.2005.11.016.
- Crook, A.J.L., Willson, S.M., Yu, J.G., and Owen, D.R.J., 2006, Predictive modelling of structure evolution in sandbox experiments: *Journal of Structural Geology*, v. 28, no. 5, p. 729–744, doi: 10.1016/j.jsg.2006.02.002.
- Dahlen, F.A., 1990, Critical Taper Model Of Fold-And-Thrust Belts And Accretionary Wedges: *Annual Review of Earth and Planetary Sciences*, v. 18, no. 1, p. 55–99, doi: 10.1146/annurev.earth.18.1.55.
- Dahlen, F.A., Suppe, J., and Davis, D., 1984, Mechanics of fold-and-thrust belts and accretionary wedges: Cohesive Coulomb Theory: *Journal of Geophysical Research: Solid Earth*, v. 89, B12, p. 10087–10101, doi: 10.1029/JB089iB12p10087.
- Davis, D., Suppe, J., and Dahlen, F.A., 1983, Mechanics of fold-and-thrust belts and accretionary wedges: *Journal of Geophysical Research*, v. 88, B2, p. 1153, doi: 10.1029/JB088iB02p01153.
- Dieterich, J.H., 1978, Time-dependent friction and the mechanics of stick-slip: *Pure and Applied Geophysics PAGEOPH*, v. 116, 4–5, p. 790–806, doi: 10.1007/BF00876539.
- Dimitrov, L.I., 2002, Mud volcanoes—the most important pathway for degassing deeply buried sediments: *Earth-Science Reviews*, v. 59, 1–4, p. 49–76, doi: 10.1016/S0012-8252(02)00069-7.
- Dixon, T.H., and Moore, C., editors, 2007, *The Seismogenic Zone of Subduction Thrust Faults*: New York Chichester, West Sussex, Columbia University Press.
- Flemings, P.B., and Saffer, D.M., 2018, Pressure and Stress Prediction in the Nankai Accretionary Prism: A Critical State Soil Mechanics Porosity-Based Approach: *Journal of Geophysical Research: Solid Earth*, v. 123, no. 2, p. 1089–1115, doi: 10.1002/2017JB015025.

- Gao, B., Flemings, P.B., Nikolinakou, M.A., Saffer, D.M., and Heidari, M., 2018, Mechanics of Fold - and - Thrust Belts Based on Geomechanical Modeling: *Journal of Geophysical Research: Solid Earth*.
- Gordon, D.S., and Flemings, P.B., 2002, Generation of overpressure and compaction-driven fluid flow in a Plio-Pleistocene growth-faulted basin, Eugene Island 330, offshore Louisiana: *Basin Research*, v. 10, no. 2, p. 177–196, doi: 10.1046/j.1365-2117.1998.00052.x.
- Hacker, B.R., 1997, Diagenesis and fault valve seismicity of crustal faults: *Journal of Geophysical Research: Solid Earth*, v. 102, B11, p. 24459–24467.
- Han, S., Bangs, N.L., Carbotte, S.M., Saffer, D.M., and Gibson, J.C., 2017, Links between sediment consolidation and Cascadia megathrust slip behaviour: *Nature Geoscience*, v. 10, no. 12, p. 954–959, doi: 10.1038/s41561-017-0007-2.
- Hardebeck, J.L., and Loveless, J.P., 2018, Creeping subduction zones are weaker than locked subduction zones: *Nature Geoscience*, v. 11, no. 1, p. 60.
- Hart, B.S., Flemings, P.B., and Deshpande, A., 1995, Porosity and pressure: Role of compaction disequilibrium in the development of geopressures in a Gulf Coast Pleistocene basin: *Geology*, v. 23, no. 1, p. 45, doi: 10.1130/0091-7613(1995)023<0045:PAPROC>2.3.CO;2.
- Hauser, M.R., Couzens-Schultz, B.A., and Chan, A.W., 2014, Estimating the influence of stress state on compaction behavior: *Geophysics*, v. 79, no. 6, D389-D398, doi: 10.1190/geo2014-0089.1.
- Heidari, M., Nikolinakou, M.A., and Flemings, P.B., 2018, Coupling geomechanical modeling with seismic pressure prediction: *Geophysics*, v. 83, no. 5, p. 1–54.
- Heidari, M., Nikolinakou, M.A., Hudec, M.R., and Flemings, P.B., 2016, Geomechanical analysis of a welding salt layer and its effects on adjacent sediments: *Tectonophysics*, v. 683, p. 172–181, doi: 10.1016/j.tecto.2016.06.027.
- Hirono, T., Tsuda, K., Tanikawa, W., Ampuero, J.-P., Shibazaki, B., Kinoshita, M., and Mori, J.J., 2016, Near-trench slip potential of megaquakes evaluated from fault properties and conditions: *Scientific reports*, v. 6, p. 28184, doi: 10.1038/srep28184.
- Hubbert, M.K., and Rubey, W.W., 1959, Mechanics of fluid-filled porous solids and its application to overthrust faulting: *Geological Society of America Bulletin*, v. 70, p. 115–166.

- Jordan, T.H., and Grotzinger, J., 2008, *The Essential Earth*, W. H. Freeman.
- Karig, D.E., 1986, Physical properties and mechanical state of accreted sediments in the Nankai Trough, Southwest Japan Arc, in Moore, J.C., ed., *Structural Fabrics in Deep Sea Drilling Project Cores From Forearcs*, Geological Society of America, p. 117–133.
- Karig, D. (1990). Experimental and observational constraints on the mechanical behaviour in the toes of accretionary prisms. Geological Society, London, *Special Publications*, 54, 383–398.
- Kim, S., and Hosseini, S.A., 2014, Geological CO₂ storage: Incorporation of pore-pressure/stress coupling and thermal effects to determine maximum sustainable pressure limit: *Energy Procedia*, v. 63, p. 3339–3346, doi: 10.1016/j.egypro.2014.11.362.
- Kimura, G., Hina, S., Hamada, Y., Kameda, J., Tsuji, T., Kinoshita, M., and Yamaguchi, A., 2012, Runaway slip to the trench due to rupture of highly pressurized megathrust beneath the middle trench slope: The tsunamigenesis of the 2011 Tohoku earthquake off the east coast of northern Japan: *Earth and Planetary Science Letters*, 339-340, p. 32–45, doi: 10.1016/j.epsl.2012.04.002.
- Kitajima, H., Saffer, D., Sone, H., Tobin, H., and Hirose, T., 2017, In Situ Stress and Pore Pressure in the Deep Interior of the Nankai Accretionary Prism, Integrated Ocean Drilling Program Site C0002: *Geophysical Research Letters*, v. 44, no. 19, p. 9644–9652, doi: 10.1002/2017GL075127.
- Kitajima, H., and Saffer, D.M., 2012, Elevated pore pressure and anomalously low stress in regions of low frequency earthquakes along the Nankai Trough subduction megathrust: *Geophysical Research Letters*, v. 39, no. 23, n/a-n/a, doi: 10.1029/2012GL053793.
- Lallemand, S.E., Schnürle, P., and Malavieille, J., 1994, Coulomb theory applied to accretionary and nonaccretionary wedges: Possible causes for tectonic erosion and/or frontal accretion: *Journal of Geophysical Research: Solid Earth* (1978–2012), v. 99, p. 12033–12055.
- Lewis, R.W., and Schrefler, B.A., 1998, *The finite element method in the static and dynamic deformation and consolidation of porous media*, Wiley Chichester, Volume 2.
- Moore, J.C., and Saffer, D., 2001, Updip limit of the seismogenic zone beneath the accretionary prism of southwest Japan: An effect of diagenetic to low-grade

- metamorphic processes and increasing effective stress: *Geology*, v. 29, no. 2, p. 183–186.
- Moore, J.C., and Vrolijk, P., 1992, Fluids in accretionary prisms: *Reviews of Geophysics*, v. 30, no. 2, p. 113–135.
- Morgan, J.K., and Karig, D.E., 1995, Kinematics and a balanced and restored cross-section across the toe of the eastern Nankai accretionary prism: *Journal of Structural Geology*, v. 17, p. 31–45.
- Morgan, J.K., Karig, D.E., and Maniatty, A., 1994, The estimation of diffuse strains in the toe of the western Nankai accretionary prism: A kinematic solution: *Journal of Geophysical Research: Solid Earth (1978–2012)*, v. 99, p. 7019–7032.
- Nemcok, M., Schamel, S., and Gayer, R., 2009, *Thrustbelts: Structural architecture, thermal regimes and petroleum systems*, Cambridge University Press.
- Neuzil, C.E., 1995, Abnormal pressures as hydrodynamic phenomena: *American Journal of Science*, v. 295, no. 6, p. 742–786.
- Nikolinakou, M.A., Heidari, M., Flemings, P.B., and Hudec, M.R., 2018, Geomechanical modeling of pore pressure in evolving salt systems: *Marine and Petroleum Geology*, v. 93, p. 272–286, doi: 10.1016/j.marpetgeo.2018.03.013.
- Obara, K., and Kato, A., 2016, Connecting slow earthquakes to huge earthquakes: *Science (New York, N.Y.)*, v. 353, no. 6296, p. 253–257, doi: 10.1126/science.aaf1512.
- Obradors-Prats, J., Rouainia, M., Aplin, A.C., and Crook, A.J.L., 2017, Hydromechanical Modeling of Stress, Pore Pressure, and Porosity Evolution in Fold-and-Thrust Belt Systems: *Journal of Geophysical Research: Solid Earth*, v. 122, no. 11, p. 9383–9403, doi: 10.1002/2017JB014074.
- Obradors-Prats, J., Rouainia, M., Aplin, A.C., and Crook, A.J.L., 2017, Hydromechanical Modeling of Stress, Pore Pressure, and Porosity Evolution in Fold-and-Thrust Belt Systems: *Journal of Geophysical Research: Solid Earth*, v. 122, no. 11, p. 9383–9403, doi: 10.1002/2017JB014074.
- Peng, Z., and Gomberg, J., 2010, An integrated perspective of the continuum between earthquakes and slow-slip phenomena: *Nature Geoscience*, v. 3, no. 9, p. 599–607, doi: 10.1038/ngeo940.

- Reece, J.S., Flemings, P.B., and Germaine, J.T., editors, 2013, Data report: Permeability, compressibility, and microstructure of resedimented mudstone from IODP Expedition 322, Site C0011, Volume 322, 1-26.
- Rockfield, 2017, Elfen Explicit Manual, Version 4.10: Swansea, UK, Rockfield Software.
- Romano, F., Trasatti, E., Lorito, S., Piromallo, C., Piatanesi, A., Ito, Y., Zhao, D., Hirata, K., Lanucara, P., and Cocco, M., 2014, Structural control on the Tohoku earthquake rupture process investigated by 3D FEM, tsunami and geodetic data: Scientific reports, v. 4, p. 5631, doi: 10.1038/srep05631.
- Roscoe, K. H., and Burland, J.B., 1968, On the generalized stress-strain behaviour of wet clay, Cambridge.
- Roscoe, K.H. , Schofield, A., and Wroth, C.P., 1958, On the yielding of soils: Geotechnique, v. 8, p. 22–53.
- Rowe, K.T., Screaton, E.J., and Ge, S., 2012, Coupled fluid flow and deformation modeling of the frontal thrust region of the Kumano Basin transect, Japan: Implications for fluid pressures and decollement downstepping: Geochemistry, Geophysics, Geosystems, v. 13, no. 3, n/a-n/a, doi: 10.1029/2011GC003861.
- Saffer, D.M., and Bekins, B.A., 2002, Hydrologic controls on the morphology and mechanics of accretionary wedges: Geology, v. 30, no. 3, p. 271, doi: 10.1130/0091-7613(2002)030<0271:HCOTMA>2.0.CO;2.
- Saffer, D.M., and Bekins, B.A., 2006, An evaluation of factors influencing pore pressure in accretionary complexes: Implications for taper angle and wedge mechanics: Journal of Geophysical Research, v. 111, B4, p. 104, doi: 10.1029/2005JB003990.
- Saffer, D.M., and Tobin, H.J., 2011, Hydrogeology and Mechanics of Subduction Zone Forearcs: Fluid Flow and Pore Pressure: Annual Review of Earth and Planetary Sciences, v. 39, no. 1, p. 157–186, doi: 10.1146/annurev-earth-040610-133408.
- Saffer, D.M., and Tobin, H.J., 2011, Hydrogeology and Mechanics of Subduction Zone Forearcs: Fluid Flow and Pore Pressure: Annual Review of Earth and Planetary Sciences, v. 39, no. 1, p. 157–186, doi: 10.1146/annurev-earth-040610-133408.
- Saffer, D.M., and Wallace, L.M., 2015, The frictional, hydrologic, metamorphic and thermal habitat of shallow slow earthquakes: Nature Geoscience, v. 8, no. 8, p. 594–600, doi: 10.1038/ngeo2490.

- Sawai, M., Niemeijer, A.R., Plümpner, O., Hirose, T., and Spiers, C.J., 2016, Nucleation of frictional instability caused by fluid pressurization in subducted blueschist: *Geophysical Research Letters*, v. 43, no. 6, p. 2543–2551, doi: 10.1002/2015GL067569.
- Schofield, A., and Wroth, P., 1968, *Critical state soil mechanics*.
- Scholz, C.H., 2002, *The Mechanics of Earthquakes and Faulting*.
- Screaton, E., Saffer, D., Henry, P., and Hunze, S., 2002, Porosity loss within the underthrust sediments of the Nankai accretionary complex: Implications for overpressures: *Geology*, v. 30, no. 1, p. 19, doi: 10.1130/0091-7613(2002)030<0019:PLWTUS>2.0.CO;2.
- Steele, J.H., Thorpe, S.A., and Turekian, K.K., 2009, *Encyclopedia of Ocean Sciences*, Elsevier, *Encyclopedia of Ocean Sciences*.
- Stigall, J., and Dugan, B., 2010, Overpressure and earthquake initiated slope failure in the Ursa region, northern Gulf of Mexico: *Journal of Geophysical Research: Solid Earth* (1978–2012), v. 115, B4.
- Tonegawa, T., Araki, E., Kimura, T., Nakamura, T., Nakano, M., and Suzuki, K., 2017, Sporadic low-velocity volumes spatially correlate with shallow very low frequency earthquake clusters: *Nature communications*, v. 8, no. 1, p. 2048, doi: 10.1038/s41467-017-02276-8.
- Tsuji, T., Kamei, R., and Pratt, R.G., 2014, Pore pressure distribution of a mega-splay fault system in the Nankai Trough subduction zone: Insight into up-dip extent of the seismogenic zone: *Earth and Planetary Science Letters*, v. 396, p. 165–178, doi: 10.1016/j.epsl.2014.04.011.
- Tsuji, T., Tokuyama, H., Costa Pisani, P., and Moore, G., 2008, Effective stress and pore pressure in the Nankai accretionary prism off the Muroto Peninsula, southwestern Japan: *Journal of Geophysical Research: Solid Earth* (1978–2012), v. 113, p. 1–19, doi: 10.1029/2007JB005002.
- Wallace, L.M., Kaneko, Y., Hreinsdóttir, S., Hamling, I., Peng, Z., Bartlow, N., D’Anastasio, E., and Fry, B., 2017, Large-scale dynamic triggering of shallow slow slip enhanced by overlying sedimentary wedge: *Nature Geoscience*, v. 10, no. 10, p. 765–770, doi: 10.1038/ngeo3021.
- Wood, D.M., 1990, *Soil behaviour and critical state soil mechanics*, Cambridge University Press.

Yang, Y., and Aplin, A.C., 2010, A permeability–porosity relationship for mudstones: *Marine and Petroleum Geology*, v. 27, no. 8, p. 1692–1697, doi: 10.1016/j.marpetgeo.2009.07.001.

Zienkiewicz, O.C., Chan, A.H.C., Pastor, M., Paul, D.K., and Shiomi, T., 1990, Static and dynamic behaviour of soils: a rational approach to quantitative solutions. I. Fully saturated problems: *Proc. R. Soc. Lond. A*, v. 429, no. 1877, p. 285–309.

Zoback, M.D., 2010, *Reservoir geomechanics*, Cambridge University Press., p. 340-369.